INFORMATION TO USERS

This manuscript has been reproduced from the microfilm master. UMI films the text directly from the original or copy submitted. Thus, some thesis and dissertation copies are in typewriter face, while others may be from any type of computer printer.

The quality of this reproduction is dependent upon the quality of the copy submitted. Broken or indistinct print, colored or poor quality illustrations and photographs, print bleedthrough, substandard margins, and improper alignment can adversely affect reproduction.

In the unlikely event that the author did not send UMI a complete manuscript and there are missing pages, these will be noted. Also, if unauthorized copyright material had to be removed, a note will indicate the deletion.

Oversize materials (e.g., maps, drawings, charts) are reproduced by sectioning the original, beginning at the upper left-hand corner and continuing from left to right in equal sections with small overlaps. Each original is also photographed in one exposure and is included in reduced form at the back of the book.

Photographs included in the original manuscript have been reproduced xerographically in this copy. Higher quality 6" x 9" black and white photographic prints are available for any photographs or illustrations appearing in this copy for an additional charge. Contact UMI directly to order.

UMI

A Bell & Howell Information Company
300 North Zeeb Road, Ann Arbor MI 48106-1346 USA
313/761-4700 800/521-0600

MULTIFRAGMENTATION OF HIGHLY EXCITED NUCLEI

Todd Matthew Hamilton

Submitted to the faculty of the Graduate School
in partial fulfillment of the requirements
for the degree
Doctor of Philosophy
in the Department of Chemistry,
Indiana University
July 1996

UMI Number: 9637560

UMI Microform 9637560
Copyright 1996, by UMI Company. All rights reserved.

This microform edition is protected against unauthorized
copying under Title 17, United States Code.

UMI
300 North Zeeb Road
Ann Arbor, MI 48103

Accepted by the Graduate Faculty, Indiana University, in partial fulfillment of the requirements for the degree of Doctor of Philosophy.

Romualdo de Souza

Romualdo de Souza, Ph.D., Chairman

Andrew Bacher

Andy Bacher

P. Ortoleva

Peter Ortoleva

Vic Viola

Vic Viola

June 25, 1996

To my wife, Lisa

ACKNOWLEDGEMENTS

I am extremely grateful to my advisor, Romualdo de Souza, for his direction and encouragement over the past several years. His remarkable enthusiasm for science has helped me accomplish more than I thought possible. I also wish to thank Vic Viola, Kris Kwiatkowski, Andy Bacher, and Peter Ortoleva for serving on my research committee. My fellow group members - Earl Cornell, Yunian Lou, Brian Davin, and Shaolin Chen have each taught me a lot and I have enjoyed working alongside of them. I have also enjoyed collaborating with Corn Williams, Ray Huang, and my other colleagues at Michigan State University. I have been fortunate to receive support from the Department of Energy (Grant No.s DE-FG02-88ER40404 and DE-FG02-92ER40714) during my years at Indiana University.

I will never forget the instruction I received early in my graduate career from Darleane Hoffman, Ken Gregorich, Diana Lee, and other members of the Hoffman group at the University of California, Berkeley. I also appreciate the dedication of Ann Hoffelder, Jim Hicks, Tom Dzugan, Jim Manning, and other faculty at Cumberland College in helping me build a strong foundation for graduate work. My desire to pursue a career in science began in high school where the excellent teaching of the late John Hensley introduced me to the exciting world of chemistry.

This thesis would have been impossible without the limitless love and patience of my wife, Lisa. My parents, parents-in-law, and other members of our close-knit family have also been extremely supportive during my graduate years. I have received much spiritual support from my fellow Christians in the Church of Christ congregations here in Bloomington, in Burning Springs (KY), and in Franklin (OH). You have all helped make the journey more enjoyable.

Todd Matthew Hamilton

Multifragmentation of Highly Excited Nuclei

The decay of highly excited nuclear systems into several intermediate mass fragments (IMF: $3 \leq Z \leq 20$) is important in understanding the behavior of nuclear matter under extreme conditions of temperature and pressure. Using exclusive studies, fragment emission in the reaction ^{84}Kr + ^{197}Au at E/A = 35, 55, and 70 MeV is examined. Kinetic energy, angular, and atomic number distributions of emitted fragments are used to characterize the sources of fragment emission. Slope parameters extracted from the transverse kinetic energy distributions reach values of 32 MeV at E/A = 70 MeV; QMD simulations using a "soft" equation-of-state predict a value that is 20% lower. Evidence is presented for the reducibility of multifragmentation to an elementary binary process. For central collisions, fragment-fragment velocity correlations are used to determine the fragment emission time scale. A strong relationship is observed between the fragment velocities and the mean emission times suggesting that there are changes in the source characteristics (e.g., size, density, excitation) on a time scale concurrent with fragment emission. The data appear inconsistent with a single freeze-out condition; a statistical model which assumes fragment emission from an evolving system qualitatively reproduces the general trend of the observed data. From these results it is deduced that time is an important variable in the multifragment breakup and that multifragmentation is an evolutionary process.

TABLE OF CONTENTS

List of Tables ix

List of Figures x

I. Introduction 1

- A. Background 2
- B. Overview of Thesis Work 6
- References 8

II. Multifragmentation Theory 10

- A. Dynamical Theories 10
  - 1. Quantum Molecular Dynamics Model 10
  - 2. Boltzmann-Uehling-Uhlenbeck Model 14
- B. Statistical Theories 16
  - 1. Expanding-Emitting Source Model 16
  - 2. Microcanonical Fragmentation Code 17
- C. Summary 19
- References 21

III. Experimental Details 22

- A. Minball/Miniwall 4π Detector Array 23
  - 1. Particle Identification 24
  - 2. Energy Calibration 26

B. Ion Chamber Telescopes 27
  1. Particle Identification 28
  2. Energy Calibration 29
References 32

IV. Fragment Emission in the Reaction ^{84}Kr + ^{197}Au at E/A = 35-70 MeV 46
A. General Reaction Characteristics 46
  1. Multiplicity Distributions 46
  2. Z_{sum} Distributions 48
  3. Atomic Number Distributions 49
B. Fragment Energy Spectra 52
  1. Ion Chamber Telescope Energy Spectra 52
  2. Comparisons with Independent Calibrations 54
C. Moving-source Fits 56
  1. Backward-Angle Spectra 56
  2. Two-source Fits 59
D. Multifragmentation Systematics 62
  1. Non-thermal Behavior in Multifragment Decay 62
  2. Comparisons to the Predictions of the QMD Model 65
  3. Evidence for the Reducibility of Multifragment Emission 68
References 74

V. Assessing the Evolutionary Nature of Multifragment Decay 118
A. Velocity Correlation Functions 118
B. Model Comparisons 121
References 125

VI. Changing Source Characteristics During Multifragment Decay ... 130

A. Impact Parameter Selection ... 130

B. Inclusive Correlation Functions ... 133

C. Exclusive Correlation Functions ... 137

D. Finite Detector Resolution Effects ... 141

E. Sensitivity to Source Assumptions ... 143

F. Angular Momentum Distortions ... 145

References ... 149

VII. Conclusions ... 176

Appendix A Data Tape Format ... 180

1. Raw Data Tape Format ... 180
2. Physics Tape Format ... 182
3. Data Summary Tape Format ... 184

Appendix B Coulomb Trajectory Model ... 185

Appendix C Data Analysis Techniques ... 187

1. Velocity Correlation Functions ... 187
2. Azimuthal Correlation Functions ... 188
3. List of Analysis Programs ... 189

LIST OF TABLES

Table 3.1 Coverage in solid, polar, and azimuthal angles for individual detectors in the Miniball/Miniwall array. The Miniball rings are labeled 3′-11; the Miniwall rings are labeled 12-17. Ring 17 was not used in this experiment 31

Table 4.1 Table of parameters for two-source fits to the energy spectra of fragments emitted in the reaction ^{84}Kr + ^{197}Au at E/A = 35, 55, and 70 MeV. The Normalization constants, N_i are given in units of ($sr^{-1}MeV^{-2}$). The slope parameters, T_i, and Coulomb parameters, V_{C_i}, are in units of MeV. The source velocities are expressed as a fraction of the speed of light, c = 30.0 cm/ns 73

Table 6.1 Table of parameters for fits to the azimuthal correlation functions for ^{84}Kr + ^{197}Au at E/A = 35 MeV with the form $A[1+\lambda_1\cos(\Delta\phi)+\lambda_2\cos(2\Delta\phi)]$. The errors are estimated to be ±0.10 for λ_1 and ±0.05 for λ_2 148

Table A.1 Event structure for each particle 181

Table A.2 Hit detectors in the 91014 Experiment 181

Table A.3 Isotope identification words for the Miniball/Miniwall detectors 182

Table A.4 Isotope identification words for the ion chamber telescopes 183

Table C.1 List of Analysis Programs 189

LIST OF FIGURES

Figure 3.1 Half-plane section of the Miniball/Miniwall detector array. Each ring is labeled (rings 3′-11 for the Miniball and rings 12-17 for the Miniwall) and the number of detectors in each ring is given in parentheses 33

Figure 3.2 Artist's perspective of the original Miniball detector array 34

Figure 3.3 Schematic diagram of an individual phoswich detector 35

Figure 3.4 Schematic anode signal from the photomultiplier tube of a phoswich detector along with the timing and widths of the "fast", "slow", and "tail" gates .. 35

Figure 3.5 "Fast" versus "slow" spectrum measured in ring 3′ (θ_{lab} = 28 °) in the reaction ^{84}Kr + ^{197}Au at E/A = 55 MeV 36

Figure 3.6 "Tail" versus "slow" spectrum measured in ring 3′ (θ_{lab} = 28 °) in the reaction ^{84}Kr + ^{197}Au at E/A = 55 MeV 37

Figure 3.7 Expanded view of the lower left region in Figure 3.6 showing the Z=1 isotopes 38

Figure 3.8 Schematic tail versus slow plot which describes variables used in constructing the PDT function 39

Figure 3.9 "Slow" versus PDT spectrum measured in ring 3′ (θ_{lab} = 28 °) in the reaction ^{84}Kr + ^{197}Au at E/A = 55 MeV. See text for a discussion of the PDT function 40

Figure 3.10 Calibration data for ^{4}He (solid circles), ^{6}Li (open fancy crosses), ^{10}B (crosses), ^{12}C (open circles), ^{14}N (solid squares), ^{16}O (open diamonds), and ^{20}Ne (open squares) [4] The lines are fits with the form given by Eq. 6 (solid lines for odd charge elements and dashed lines for even charge elements). 41

Figure 3.11 Cross-sectional view of an ion chamber telescope (from Ref. [3]) 42

Figure 3.12 Two-dimensional plot of energy deposited in ion-chamber versus energy deposited in Si(IP) detector (from Ref. [3]) 43

Figure 3.13 Two-dimensional plot of energy deposited in Si(IP) detector versus energy deposited in CsI(Tl) crystal (from Ref. [3]) 44

Figure 3.14 Dependence of light output on deposited energy for various particles (from Ref. [3]): p,d, and t isotopes (closed circles) and ^{3,4}He nuclei (closed squares) which punchthrough the CsI(Tl) crystal, deuteron (open circles) and α (open squares) beams of 22 MeV/u, 16 MeV/u, and 12 MeV/u which pass through the Si(IP) detector, and ^{12}C (open diamonds) and ^{16}O (closed diamonds) beams of 22 MeV/u and 17 MeV/u (top panel) and 22, 17, and 12 MeV/u (bottom panel) 45

Figure 4.1 Charged particle multiplicity distributions measured in the reactions ^{84}Kr + ^{197}Au at E/A = 35-70 MeV, ^{36}Ar + ^{197}Au at E/A = 50-110 MeV, and ^{14}N + ^{197}Au at E/A = 100-156 MeV 77

Figure 4.2 Dependence of the mean IMF multiplicity on the charged particle multiplicity for the reactions ^{84}Kr + ^{197}Au at E/A = 35-70 MeV, ^{36}Ar + ^{197}Au at E/A =

50-110 MeV, and ^{14}N + ^{197}Au at E/A = 100-156 MeV 78

Figure 4.3 Dependence of the total detected charge, Z_{sum}, on the charged particle multiplicity for the reaction ^{84}Kr + ^{197}Au at E/A = 35 MeV (top panel) and E/A = 70 MeV (bottom panel) 79

Figure 4.4 Total detected charge distributions for different cuts in charged particle multiplicity in the reaction ^{84}Kr + ^{197}Au at E/A = 55 MeV 80

Figure 4.5 Dependence of the mean (top panel) and the variance (bottom panel) of the total detected charge distribution on the charged particle multiplicity in the reaction ^{84}Kr + ^{197}Au at E/A = 35 (open circles), 55 (closed circles), and 70 MeV/A (open squares) 81

Figure 4.6 Inclusive Z distributions measured in the ion chamber telescopes at θ_{lab} = 45° (top panel), 72.5° (middle panel), and 130° (bottom panel) in the reaction ^{84}Kr + ^{197}Au at E/A = 55 MeV. The solid and dashed lines correspond to software thresholds equal to the Miniball thresholds and twice the Miniball thresholds, respectively . 82

Figure 4.7 (a) Inclusive Z distributions measured in the ion chamber telescopes (solid points) and the Miniball detectors (open points) at θ_{lab} = 35.5° in the reaction ^{84}Kr + ^{197}Au at E/A = 35 MeV. The line corresponds to a power law fit with the form $P(Z) \approx Z^{-\tau}$. (b) The same as in panel (a) expect at θ_{lab} = 110°. Solid and dashed lines correspond to power law fits to the data measured in the ion chamber telescope and Miniball detectors, respectively 83

Figure 4.8 (a) Dependence of the τ parameter on θ_{lab} from power law fits to the Z distributions measured in the ion chamber telescopes (solid points) and the Miniball detectors (open points) in the reaction ^{84}Kr + ^{197}Au at E/A = 35 MeV. (b) The same as in panel (a) except at E/A = 70 MeV 84

Figure 4.9 (a) The charged particle multiplicity distribution measured in the reaction ^{84}Kr + ^{197}Au at E/A = 55 MeV with the requirement of detecting two or more particles in the Miniball/Miniwall detector array. (b) The same as in panel (a) with the additional requirement of detecting a particle in an ion chamber telescope. (c) The same as in panel (a) with the additional requirement of detecting an IMF in an ion chamber telescope 85

Figure 4.10 Kinetic energy spectra of lithium fragments measured in the ion chamber telescopes for central and midcentral collisions ($b/b_{max} \leq 0.4$) in the reaction ^{84}Kr + ^{197}Au at E/A = 35 MeV 86

Figure 4.11 The same as in Figure 4.10 except for carbon fragments 87

Figure 4.12 The same as in Figure 4.10 except at E/A = 55 MeV 88

Figure 4.13 The same as in Figure 4.10 except for carbon fragments at E/A = 55 MeV 89

Figure 4.14 The same as in Figure 4.10 except at E/A = 70 MeV 90

Figure 4.15 The same as in Figure 4.10 except for carbon fragments at E/A = 70 MeV 91

Figure 4.16 Comparison between kinetic energy spectra for lithium fragments measured in the ion chamber telescopes ($b/b_{max} \leq 0.4$, solid points) and the Miniball detectors ($b/b_{max} \leq 0.2$, open points) in the reaction ^{84}Kr + ^{197}Au at E/A = 55 MeV 92

Figure 4.17 The same as in Figure 4.16 except for carbon fragments 93

Figure 4.18 Comparison between inclusive kinetic energy spectra for lithium fragments measured in the ion chamber telescopes (solid points and solid line) and spectra measured by Milkau *et. al.* (open points, Ref. [7]) in the reaction ^{84}Kr + ^{197}Au at E/A = 35 MeV. See text for a description of the arrows 94

Figure 4.19 The same as in Figure 4.18 except for carbon fragments 95

Figure 4.20 Backward angle kinetic energy spectra of fragments (Z = 3 to 6) measured in the ion chamber telescopes for central and midcentral collisions ($b/b_{max} \leq 0.4$) in the reaction ^{84}Kr + ^{197}Au at E/A = 35, 55, and 70 MeV 96

Figure 4.21 Single source fits of backward angle kinetic energy spectra of lithium (left panels) and carbon (right panels) fragments measured in the ion chamber telescopes for central and midcentral collisions ($b/b_{max} \leq 0.4$) in the reaction ^{84}Kr + ^{197}Au at E/A = 55 MeV. The lines in the top panels correspond to source fits with all parameters varying freely. In the bottom panels, the lines correspond to source fits with the temperature parameter fixed to the indicated values 97

Figure 4.22 Dependence of the temperature parameter on Z from single source fits to the backward angle kinetic energy spectra. The fragments were measured in the ion chamber telescopes for central and midcentral collisions ($b/b_{max} \leq 0.4$) in the reaction ^{84}Kr + ^{197}Au at E/A = 35 (open diamonds), 55 (closed circles), and 70 MeV (open squares) 98

Figure 4.23 Two-source fits of kinetic energy spectra of beryllium fragments measured in the ion chamber telescopes for central and midcentral collisions ($b/b_{max} \leq 0.4$) in the reaction ^{84}Kr + ^{197}Au at E/A = 55 MeV. The dashed line represents emission from target-like fragment (TLF); the dotdashed line represent emission from the intermediate rapidity source (IRS). The solid line is the sum of the TLF and IRS components 99

Figure 4.24 (a) Kinetic energy spectra of boron fragments emitted in central collisions of the reaction ^{84}Kr + ^{197}Au at E/A = 55 MeV. (b) Transverse kinetic energy spectra constructed from the spectra shown in (a) 100

Figure 4.25 Extracted slopes from the transverse kinetic energy distributions for boron fragments emitted in central collisions. The beam energies represented for each system are described in the text 101

Figure 4.26 Slope parameters of the target-like source from moving-source fits of boron kinetic energy spectra. The beam energies represented for each system and the QMD calculations are described in the text 102

Figure 4.27 Simulation of a central collision (impact parameter = 0.5 fm) in the reaction ^{84}Kr + ^{197}Au at E/A = 70 MeV using the Quantum molecular Dynamics (QMD) model for the different timesteps indicated in the figure. The ^{84}Kr projectile nucleons are represented as solid circles; the ^{197}Au target nucleons are represented as open circles 103

Figure 4.28 Intermediate mass fragment and charged particle multiplicities from QMD simulations of central collisions in the reactions ^{14}N + ^{197}Au at E/A = 156 MeV (top panels) and ^{84}Kr + ^{197}Au at E/A = 70 MeV (bottom panels) 104

Figure 4.29 Effective charge distributions from QMD simulations of central collisions in the reactions ^{14}N + ^{197}Au at E/A = 156 MeV (top panel) and ^{84}Kr + ^{197}Au at E/A = 70 MeV (bottom panel) 105

Figure 4.30 Kinetic energy spectra of Z_{eff}=3 fragments from QMD simulations of central collisions in the reaction ^{84}Kr + ^{197}Au at E/A = 70 MeV. The spectra are shown before (panel (a)) and after (panel (b)) the n-body Coulomb trajectory calculation (see text) 106

Figure 4.31 Transverse kinetic energy spectra of Z_{eff}=4 fragments from QMD simulations of central collisions in the reactions ^{14}N + ^{197}Au at E/A = 156 MeV (open squares), ^{36}Ar + ^{197}Au at E/A = 80 MeV (closed circles), and ^{84}Kr + ^{197}Au at E/A = 70 MeV (open diamonds). The spectra are shown before (panel (a)) and after (panel (b)) the n-body Coulomb trajectory calculation (see text) 107

Figure 4.32 The reciprocal of the binary decay probability 1/p (calculated from the mean and variance of the IMF distributions) as a function of $E_t^{-1/2}$ for the reaction ^{84}Kr + ^{197}Au at E/A = 35 (open diamonds), 55 (closed squares) and 70 MeV (open circles) 108

Figure 4.33 Dependence of the mean and variance of the IMF distribution, and the number of "tries" on the total transverse energy for the reaction ^{84}Kr + ^{197}Au at E/A = 35 (open diamonds), 55 (closed squares) and 70 MeV (open circles) 109

Figure 4.34 The reciprocal of the binary decay probability 1/p as a function of $E_t^{-1/2}$ for the reaction ^{84}Kr + ^{197}Au at E/A = 70 MeV 110

Figure 4.35 Longitudinal velocity distributions for alpha particles (top panel) and boron fragments (bottom panel) emitted in peripheral collisions ($b/b_{max} \geq 0.8$) of the reaction ^{84}Kr + ^{197}Au at E/A = 70 MeV. The arrows are described in the text 111

Figure 4.36 The same as in Figure 4.28 after eliminating punchthrough and high v_z particles (see text) 112

Figure 4.37 The reciprocal of the binary decay probability 1/p as a function of $E_t^{-1/2}$ for the reaction ^{36}Ar + ^{197}Au at E/A = 110 MeV. The different restrictions are described in the text 113

Figure 4.38 Dependence of the mean and variance of the IMF distribution, and the number of "tries" on the total transverse energy for the reaction ^{36}Ar + ^{197}Au at E/A = 50 (open diamonds), 80 (closed squares) and 110 MeV (open circles). Punchthrough and high v_z particles have been eliminated (see text) 114

Figure 4.39 The reciprocal of the binary decay probability 1/p as a function of $E_t^{-1/2}$ for the reactions ^{84}Kr + ^{197}Au at E/A = 35, 55, and 70 MeV and reactions ^{36}Ar + ^{197}Au at E/A = 50, 80, and 110 MeV. Punchthrough and high v_z particles have been eliminated 115

Figure 4.40 The reciprocal of the binary decay probability 1/p (calculated from the mean and variance of the IMF distributions) as a function of $E_t^{-1/2}$ for the reaction ^{14}N + ^{197}Au at E/A = 100 (open diamonds), 130 (closed squares) and 156 MeV (open circles) 116

Figure 4.41 Dependence of the mean and variance of the IMF distribution, and the number of "tries" on the total transverse energy for the reaction ^{14}N + ^{197}Au at E/A

= 100 (open diamonds), 130 (closed squares) and 156 MeV (open circles) 117

Figure 5.1 Inclusive kinetic energy spectra for Be and O fragments (closed and open symbols) emitted in central collisions 127

Figure 5.2 (a-c) Experimental correlation functions at E/A = 35, 55, 70 MeV with different restrictions on v_{min}. (d) Correlation functions constructed from the predictions of a microcanonical ensemble model for different restrictions on v_{min} 128

Figure 5.3 (a) Dependence of the Coulomb interaction (HWHM) between fragments on the minimum fragment velocity. Diamonds, circles and squares represent the experimental data at E/A = 35, 55, and 70 MeV. Solid lines indicate the results of 3-body Coulomb trajectory calculations for τ = 25, 100, and 200 fm/c. (b) Dependence of the extracted emission time on the minimum velocity of the fragment pair. The solid circles and open squares correspond to the experimental data at E/A = 55 MeV 129

Figure 6.1 Dependence of the fit parameter τ on N_c extracted from power law fits to the Z distributions measured in the angular range $25° \leq \theta_{lab} \leq 50°$ for the reaction ^{84}Kr + ^{197}Au at E/A = 35 (open circles), 55 (closed circles), and 70 MeV (open squares). Inset: Z distributions measured for particles emitted in collisions of different impact parameters at E/A = 55 MeV. The solid lines represent power law fits for 3≤ Z ≤ 14 with the functional form P(Z) $\propto Z^{-\tau}$ 151

Figure 6.2 (a) fragment energy spectra for beryllium fragments emitted for central collisions in the reaction ^{84}Kr + ^{197}Au at E/A = 55 MeV. The solid line is the energy spectrum calculated by the 3-body Coulomb trajectory model for Z_s=40, A_s=96 and R_s=7 fm. (b) The same as in panel (a) for carbon fragments 152

Figure 6.3 (a) Velocity plots, $d^2N/v^2dvd\Omega$, for beryllium fragments emitted in peripheral collsions for the reaction ^{84}Kr + ^{197}Au at E/A = 70 MeV. The detector thresholds are depicted as a dashed line. (b) The same as in panel (a) except for central collisions. The two solid lines indicate the angular region $25° \leq \theta_{lab} \leq 50°$ 153

Figure 6.4 (a) Dependence of the reduced velocity on the longitudinal component of the center-of-mass velocity of the IMF pair for peripheral collisions in the reaction ^{84}Kr + ^{197}Au at E/A = 70 MeV. (b) The same as in panel (a) except for central collisions. (c) The same as in panel (b) for the angular range $25° \leq \theta_{lab} \leq 50°$ ..154

Figure 6.5 Fragment-fragment velocity correlation functions for central collisions in the reaction ^{84}Kr + ^{197}Au at E/A = 35 (open circles), 55 (closed circles), and 70 MeV (open squares) 155

Figure 6.6 (a) Comparisons of 3-body trajectory calculations with the best χ^2/ν values to the experimental correlation functions for central collisions in the reaction ^{84}Kr + ^{197}Au at E/A = 35 MeV. (b) The same as in panel (a) except for E/A = 70 MeV 156

Figure 6.7 Dependence of the mean emission time, τ, on the source radius, R_s from comparisons with the best χ^2/ν between the 3-body trajectory calculations and the experimental data. The closed and open circles represent central collisons in the reaction ^{84}Kr + ^{197}Au at E/A = 35 and 70 MeV, respectively. The solid and dashed lines represent central collisions in the reaction ^{36}Ar + ^{197}Au at E/A = 50 and 110 MeV, respectively 157

Figure 6.8 (a) Experimental correlation functions selected on the minimum velocity of the fragment pair for central collisions in the reaction ^{84}Kr + ^{197}Au at E/A = 55 MeV. (b) Exclusive experimental correlation functions for central collisions in the reaction

^{36}Ar + ^{197}Au at E/A = 80 MeV. (b) Exclusive experimental correlation functions for central collisions in the reaction ^{14}N + ^{197}Au at E/A = 156 MeV 158

Figure 6.9 (a) Correlation functions selected on the minimum velocity of the fragment pair, v_{min} = 3.25 cm/ns (open circles) and on the average velocity of the fragment pair, v_{avg} = 3.25 cm/ns (solid line) for central collisions in the reaction ^{84}Kr + ^{197}Au at E/A = 55 MeV. (b) The same as in panel (a) except v_{min}, v_{avg} = 4.25 cm/ns. (c) The same as in panel (a) except v_{min}, v_{avg} = 5.25 cm/ns 159

Figure 6.10 (a) Correlation functions selected on the miniumum velocity of the fragment pair for boron fragments emitted for central collisions in the reaction ^{84}Kr + ^{197}Au at E/A = 55 MeV. (b) Comparison between the data selected on v_{min} = 5 cm/ns and 3-body Coulomb trajectory calculations with R_s = 7 fm and τ = 0 (dotted line), 50 (dashed line) and 100 (solid line). (b) The same as in panel (a) except v_{min} = 7 cm/ns 160

Figure 6.11 (a) Dependence of the Coulomb interaction (HWHM) between fragments on the minimum fragment velocity in the laboratory frame. Central collisions in the reaction ^{84}Kr + ^{197}Au at E/A = 35, 55, and 70 MeV are represented by closed diamonds, circles, and squares. Central collisions in the reaction ^{36}Ar + ^{197}Au at E/A = 50, 80, and 110 MeV are represented by open diamonds, circles, and squares. Central collisions in the reaction ^{14}N + ^{197}Au at E/A = 100, 130, and 156 MeV are represented by vertical crosses, diagonal crosses, and fancy diamonds. (b) The same as in panel (a) except for the center-of-mass frame 161

Figure 6.12 (a) Correlation functions selected on the minimum velocity of the fragment pair for fragments emitted in the angular range 25° $\leq \theta_{lab} \leq$ 50° for central collisions in the reaction ^{84}Kr + ^{197}Au at E/A =55 MeV. (b) The same as in panel (a) except for fragments emitted in the angular range $45° \leq \theta_{cm} \leq 90°$ 162

Figure 6.13 Correlation functions selected on the minimum fragment velocity for fragments emitted in the angular range $\theta_{cm} \leq 45°$ (panel (a)), $45° \leq \theta_{cm} \leq 90°$ (panel (b)), and $90° \leq \theta_{cm} \leq 135°$ (panel (c)) 163

Figure 6.14 Distribution of the longitudinal velocity of the IMF pair, $(v_{12})_z/v_{beam}$, for fragments emitted in the angular range $25° \leq \theta_{lab} \leq 50°$ for central collisions in the reaction ^{84}Kr + ^{197}Au at E/A = 70 MeV. The arrows correspond to values of $(v_{12})_z/v_{beam} = 0.3$, 0.4, and 0.5 164

Figure 6.15 Correlation functions selected on the minimum fragment velocity for fragment pairs with $(v_{12})_z/v_{beam} \leq 0.5$ (panel (a)), $(v_{12})_z/v_{beam} \leq 0.4$ (panel (b)), and $(v_{12})_z/v_{beam} \leq 0.3$ (panel (c)) 165

Figure 6.16 (a) Dependence of the Coulomb interaction (HWHM) between fragments on the minimum fragment velocity for fragment pairs with $(v_{12})_z/v_{beam}$ integrated (open circles), $(v_{12})_z/v_{beam} \leq 0.5$ (closed circles), $(v_{12})_z/v_{beam} \leq 0.4$ (open squares), and $(v_{12})_z/v_{beam} \leq 0.3$ (closed squares) 166

Figure 6.17 Transverse correlation functions selected on the minimum velocity of the fragment pair 167

Figure 6.18 Trajectory calculations for pairs of ^{11}B fragments, unfiltered (open circles) and filtered with the detector granularity (solid line) 168

Figure 6.19 (a) The correlation function for central collisions in the reaction ^{84}Kr + ^{197}Au at E/A = 55 MeV. The solid and dashed lines represent the results of smearing the experimentally measured energy distributions on a Gaussian distribution with a FWHM of 10% and 20%. (b) Trajectory calculations for pairs of ^{10}B (closed circles) and ^{12}B (open circles) fragments 169

Figure 6.20 Dependence of the width of the correlation function (HWHM) on the mean emission time for 3-body Coulomb trajectory calculations for pairs of ^{10}B (open circles), ^{11}B (closed diamonds), and ^{12}B (open squares) fragments. The calculations were performed for $Z_s = 79$ ($A_s = 197$), $R_s = 7$ fm, and $\tau = 100$ fm/c 170

Figure 6.21 Dependence of the mean emission time, τ, on the source radius, R_s from comparisons for the best χ^2/ν between the 3-body trajectory calculations and the experimental data. The open circles, closed circles, and open squares represent minimum velocity cutoffs of 4, 5 and 6 cm/ns 171

Figure 6.22 (a) Trajectory calculations for ^{11}B fragments with $v_s = 2.5$ cm/ns and $\tau = 100$ fm/c (open circles). The solid, dashed, and dotdashed lines represent reference calculations with $v_s = 3$ cm/ns and $\tau = 25$, 50, and 100 fm/c, respectively. (b) The same as in panel (a) except the open circles were calculated assuming $v_s = 3.5$ cm/ns 172

Figure 6.23 Azimuthal distributions with respect to the reconstructed reaction plane for peripheral ($b/b_{max} = 0.6$-0.8), midcentral ($b/b_{max} = 0.3$-0.5), and central ($b/b_{max} \leq 0.2$) collisions in the reaction ^{84}Kr + ^{197}Au at E/A = 35, 55, and 70 MeV. The solid and open circles represent alpha particles and beryllium fragments, respectively 173

Figure 6.24 Azimuthal correlation functions for peripheral ($b/b_{max} = 0.6$-0.8), midcentral ($b/b_{max} = 0.3$-0.5), and central ($b/b_{max} \leq 0.2$) collisions in the reaction ^{84}Kr

+ ^{197}Au at E/A = 35, 55, and 70 MeV. The solid and open circles represent alpha particles and beryllium fragments, respectively. Fits to the alpha particle correlation functions with the form $A[1+\lambda_1\cos(\Delta\phi)+\lambda_2\cos(2\Delta\phi)]$ are displayed as solid lines 174

Figure 6.25 (a) Correlation function selected on the minimum velocity of the pair (v_{min} = 2.75 cm/ns) for fragments emitted for central collisions in the reaction ^{84}Kr + ^{197}Au at E/A = 55 MeV with (solid line) and without (open circles) the anisotropy correction (see text). (b) The same as in panel (a) except v_{min} = 3.75 cm/ns .. 175

CHAPTER 1

INTRODUCTION

One of the primary goals of intermediate-energy (35-1000 MeV/nucleon) heavy-ion reaction studies is to understand the nuclear equation-of-state. As a fundamental description of nuclear matter, this equation is important in its own right. Characterizing the nuclear equation-of-state is also necessary to understand astrophysical phenomena, such as neutron stars and supernova explosions. The study of highly excited nuclear systems produced in heavy-ion reactions lends insight into the behavior of nuclear matter under extreme conditions of temperature and pressure, information pertinent to the nuclear equation-of-state.

Highly excited nuclear systems can decay into several intermediate mass fragments (IMF: $3 \leq Z \leq 20$), a process known as multifragmentation. This decay mode is important when the excitation energy approaches the total binding energy of the system. A complete understanding of the multifragmentation process requires the detection of all particles emitted in the heavy-ion collision and subsequent reconstruction of the disassembly in order to unravel the underlying reaction dynamics. To accomplish this objective, several exclusive experiments have been performed with high resolution 4π detector arrays [1–3]. In this thesis, exclusive data measured with low threshold detectors are examined to characterize the multifragmenting system.

A. Background

Intermediate mass fragments emitted in nuclear reactions were first identified in the 1950's in radiochemical studies of high energy proton bombardments [4,5]. These studies showed that the IMF production cross-section increases with bombarding energy from 100 MeV to about 2 GeV and then remains relatively constant [6]. Evidence for the existence of multifragmentation was first observed using emulsion techniques. Events with multiple fragments were observed in photographic emulsions exposed to cosmic rays and high energy protons [7]. However, this technique is limited in statistical accuracy and has significant limitations in unambiguous identification of the mass and charge of the emitted fragments. The introduction of semiconductor counter telescopes to fragmentation studies resulted in an abundance of high statistics inclusive fragment cross-section data [8].

An early investigation of the fragment formation mechanism focused on mass distributions produced in proton bombardments of krypton and xenon targets in the energy range 80 - 350 GeV [9]. These distributions could be described using a power law, $P(A) \propto A^{-\tau}$, with a value of tau similar to that predicted by statistical clustering models. The power-law dependence of the mass distribution was interpreted as the signature of a liquid-gas phase transition near the critical point. In this analogy, the fragments are droplets formed statistically in the highly excited nuclear remnant near its critical temperature [10]. A recent study of the fragment charge distributions produced in the reaction Au + C at 1.0 GeV/A further addressed the question of whether or not a phase transition occurs in highly excited nuclear matter [11]. Critical exponents determined using the moments of the charge distributions were found to be similar to those predicted for a finite liquid-gas system at the critical point. These types of studies, while lending insight into multifragment decay, ignore the underlying dynamics of the process.

The different scenarios which have been proposed to describe multifragmentation range from a series of sequential binary decays [12,13] to an instantaneous disassembly of the compound system [14–16]. Dynamical models, such as the Boltzmann-Uehling-Uhlenbeck (BUU) and Quantum Molecular Dynamics (QMD) codes, can successfully describe certain aspects of heavy-ion collisions in the initial stages of the reaction. Because the BUU model is a mean-field theory with no correlations between the nucleons, fragment formation cannot be described using this approach. The QMD model is an n-body approach that treats the formation of clusters, but the predicted number of fragments is typically smaller than the experimentally observed IMF multiplicities (number of IMF's emitted in a given interaction). Statistical models, which include sequential binary and statistical equilibrium approaches, roughly reproduce the fragment multiplicities. However, in the statistical treatments the properties of the emitting source are required as input parameters. One solution to the problems associated with the two different approaches is to combine them to form a hybrid model [17]. A dynamical model is used to simulate the formation of the highly excited nuclear system; the subsequent decay into fragments is treated by a statistical model. The time step at which the two models are coupled is chosen such that the particle density distribution attained in the initial dynamic stages closely matches the density assumed in the final break-up stages. Although reasonable agreement with experimental fragment distributions has been demonstrated using this prescription [17–19], the uncertainties inherent in matching the two different models remain.

Comparisons to the results from exclusive heavy-ion reaction studies at intermediate energies have provided valuable tests to distinguish between the various models of multifragmentation. For example, 4π measurements of the systems ^{36}Ar + ^{197}Au at E/A = 35-110 MeV and ^{129}Xe + ^{197}Au at E/A = 50 MeV suggest that the large number of IMFs observed in these reactions are emitted from a system that has attained low density [1,2]. This reduced density may be the result of an expansion of the system due to increased thermal pressure and/or a rapid compression-decompression cycle [10]. Investigations of multifragmenting systems have revealed experimental signatures of such an expansion. Collective expansion effects have been observed in the transverse kinetic energy spectra of fragments emitted in the reaction ^{36}Ar + ^{197}Au at E/A = 50-110 MeV [20]. Although the expansion contribution to the average kinetic energy of the fragments was small at these excitation energies, the importance of collective expansion in fragment emission was predicted to increase as the excitation energy of the system becomes larger. Evidence of a large radial collective expansion ($> 30\%$ of the initial kinetic energy) has been observed in the reaction ^{197}Au + ^{197}Au at several hundred MeV/nucleon [21]. A complete model of multifragmentation must incorporate the effects of compression and collective expansion and establish the role of these collective effects in fragment emission.

Another important criterion in differentiating between various multifragmentation models is the fragment emission time scale. Two diametrically opposed scenarios have emerged: (1) instantaneous multifragmentation, where the fragments are emitted simultaneously once the system has reached the "freeze-out" density and (2) evolutionary multifragmentation, where the fragments are emitted sequentially as the system evolves. Determining the emission time scale would aid in isolating the class of models that best describe the decay of highly excited nuclear matter. Because the time scales involved are of the order 1000 fm/c (10^{-21} s) or less, no direct methods of measuring emission times currently exist. Rather, relative emission times are extracted from the modifications to the velocities of coincident fragments. A sensitive tool to accomplish these modifications is the construction of fragment-fragment velocity correlation functions.

The technique of correlation functions originated in the field of astrophysics in the 1950's where intensity interferometry was developed to determine the dimension of distant astronomical objects [22]. The original application by Hanbury-Brown and Twiss (the technique is commonly referred to as the Hanbury-Brown/Twiss or "HBT" effect) used pairs of photons to reveal spatial information about the source from which they originate. Within a decade, the HBT effect was generalized to describe momentum correlations between identical and nonidentical nuclear fragments. Nuclear interferometry has been used extensively to investigate the space-time evolution of elementary-particle and nuclear collisions. Correlation functions have been constructed using pions, light nuclei, and more recently, IMFs [23–25]. In the case of the IMF velocity correlations, the final-state interactions are dominated by the long range Coulomb interaction and the results are generally interpreted using three- or many-body Coulomb trajectory calculations [26]. Comparisons of the IMF results to model calculations yield estimates of the fragment emission lifetime that range from $\tau \approx$ 25-400 fm/c for systems produced in heavy-ion reactions (see [25–28] and references contained therein).

B. Overview of Thesis Work

The reaction ^{84}Kr + ^{197}Au has been measured over the incident energy range 35-400 MeV/A using a 4π detector array to study the dependence of fragment multiplicity on incident energy [29]. As the incident energy is increased, the IMF multiplicity increases to a maximum value of $N_{IMF} \approx 6$ at E/A = 100 MeV. Further increasing the incident energy leads to a decrease in the fragment multiplicity, N_{IMF}. A rise in IMF multiplicity had been observed in central collisions in the reaction ^{36}Ar + ^{197}Au over the bombarding energy range 35-110 MeV [1]. For central collisions of Au+Au over the higher energy range E/A = 100-400 MeV, the IMF multiplicity decreased with increasing incident energy [30]. In the ^{84}Kr + ^{197}Au system, we have studied the initial rise and subsequent decline of IMF multiplicity with increasing bombarding energy for a single projectile-target combination.

In this thesis, characteristics of fragment distributions from the reaction ^{84}Kr + ^{197}Au at E/A = 35, 55, and 70 MeV are examined to gain insight into fragment production on the "rising" side of the excitation function. In particular, the energy spectra are used to deduce properties of the multifragmenting source. The results from the ^{84}Kr + ^{197}Au system are compared to data from the systems ^{14}N + ^{197}Au, ^{36}Ar + ^{197}Au, and ^{129}Xe + ^{197}Au to explore the systematics of fragment emission with increasing excitation of the emitting system. Transverse kinetic energy distributions are examined over the range of bombarding energies (E/A = 35-156 MeV) to determine the extent to which the available energy is equilibrated in these reactions. Evidence for the reducibility of multifragmentation to an elementary binary process is presented.

The time scale for fragment emission is extracted using the technique of correlation functions and the results are compared to predictions of the McFrag statistical multifragmentation model [16] and the Expanding, Emitting Source (EES) model

[12]. Fragment-fragment velocity correlation functions are constructed for central ("head-on") collisions to select preferentially the systems of the highest excitation. Correlation functions selected on the minimum velocity of the fragment pair provide further insight into the source of the emitted fragments. The sensitivity of the correlation function technique to measurement uncertainties and model assumptions is assessed in order to determine the relative errors associated with the deduced time scales.

The remainder of the thesis is organized as follows: Chapter 2 contains a discussion of various theoretical models. Chapter 3 describes the experimental setup used to measure the charged reaction products. General features of the reaction ^{84}Kr + ^{197}Au at E/A = 35, 55, and 70 MeV and the systematics of fragment emission for several systems over a large range in bombarding energy are presented in Chapter 4. An association between fragment velocity and the strength of the fragment-fragment Coulomb interaction is presented in Chapter 5. This association is interpreted in the context of classical Coulomb trajectory calculations and statistical multifragmentation models in the same chapter. In Chapter 6, the universality of the association and the effect of different selection criteria are explored. Conclusions from this work are stated in Chapter 7.

REFERENCES

[1] R.T. de Souza *et al.*, Phys. Lett. **B268**, 6 (1991).

[2] D.R. Bowman *et al.*, Phys. Rev. Lett. **67**, 1527 (1991).

[3] K. Kwiatkowski *et al.*, Phys. Rev. Lett. **74**, 3756 (1995).

[4] G. Friedlander *et al.*, Phys. Rev. **94**, 727 (1954).

[5] R. Wolfgang *et al.*, Phys. Rev. **103**, 394 (1956).

[6] E.K. Hyde *et al.*, Phys. Rev. C **71**, 1759 (1971).

[7] C.F. Powell and G.P.S. Occhialini, Nature **159**, 93 (1947).

[8] W.G. Lynch *et al.*, Ann. Rev. Nucl. Part. Sci. **37**, 493 (1987).

[9] J.E. Finn *et al.*, Phys. Rev. Lett. **49**, 1321 (1982).

[10] G. Bertsch and P.J. Siemens, Phys. Lett. **B126**, 9 (1983).

[11] M.L. Gilkes *et al.*, Phys. Rev. Lett. **73**, 1590 (1994).

[12] W.A. Friedman, Phys. Rev. C **42**, 667 (1990).

[13] L. Phair *et al.*, Phys. Rev. Lett. **75**, 213 (1995).

[14] W. Bauer *eta al.*, Phys. Rev. C **34**, 2127 (1986).Z

[15] J. Aichelin *et al.*, Phys. Rev. C **37**, 2451 (1988).

[16] D.H.E. Gross *et al.*, Phys. Rev. Lett. **56**, 1544 (1986).

[17] D.R. Bowman *et al.*, Phys. Rev. C **46**, 1834 (1992).

[18] K. Kwiatkowski *et al.*, Phys. Rev. C **49**, 1516 (1994).

[19] B. Heide and H.W. Barz, Nucl. Phys. **A588**, 918 (1995).

[20] R.T. de Souza *et al.*, Phys. Lett. **B300** 29 (1993).

[21] S.C. Jeong *et al.*, Phys. Rev. Lett. **72**, 3468 (1994).

[22] D.H. Boal *et al.*, Rev. Mod. Phys. **62**, 553 (1990).

[23] R. Trockel *et al.*, Phys. Rev. Lett. **59**, 2844 (1987).

[24] Y.D. Kim *et al.*, Phys. Rev. C **45**, 338 (1992).

[25] D. Fox *et al.*, Phys. Rev. C **50**, 2424 (1994).

[26] T. Glasmacher *et al.*, Phys. Rev. C **50**, 952 (1994).

[27] E. Bauge *et al.*, Phys. Rev. Lett. **70**, 3705 (1993).

[28] J. Lauret and R.A. Lacey, Phys. Lett. **B327**, 3705 (1993).

[29] G.F. Peaslee *et al.*, Phys. Rev. C **49**, R2771 (1994).

[30] M.B. Tsang *et al.*, Phys. Rev. Lett. **71**, 1502 (1993).

CHAPTER 2

MULTIFRAGMENTATION THEORY

Theories of multifragmentation can be classified into two main groups: (1) dynamical theories, which describe the collision process from the early stages to the break-up of the excited system, and (2) statistical theories, where an excited, equilibrated nuclear system decays statistically. In the next section, two examples of dynamical theories will be discussed. The first is an extension of Molecular Dynamics theory that includes quantum features and the second is based upon the Boltzmann-Uehling-Uhlenbeck equation. Both are transport codes that describe the time evolution of the nucleon phase-space density during the course of a nucleus-nucleus collision. In the section to follow, the Expanding-Emitting Source model and the Microcanonical Fragmentation Model are described. These two models represent different scenarios for the decay of an equlibrated, statistically-emitting system. The system evolves on a time scale concurrent with fragment emission in the former model; the system undergoes an instantaneous disassembly in the latter model.

A. Dynamical Theories

1. Quantum Molecular Dynamics Model

The Quantum Molecular Dynamics (QMD) Model is an n-body description of heavy-ion collisions at intermediate energies (E/A=30 to 1000) [1]. The nucleons are represented as Gaussian wave packets given by:

$$f_i(\mathbf{r},\mathbf{p}) = \left(\frac{1}{\pi\hbar}\right)^3 \exp\left[-\alpha^2(\mathbf{r}-\mathbf{r}_i)^2\right]\exp\left(-\frac{1}{\alpha^2\hbar^2}(\mathbf{p}-\mathbf{p}_i)^2\right), \tag{1}$$

where **r** and **p** are the mean position and momentum of the ith nucleon, respectively, and the width of the Gaussian, α, is an adjustable parameter [2]. Contrary to a strictly quantum approach, no dispersion of the Gaussian is assumed throughout the collision process. The sensitivity of the results to the assumed width have been investigated: doubling the width parameter, α, changes the mass yield by 20%. The initial centroids of the Gaussians are chosen to reproduce the density and momentum distributions of nuclei in the ground state [2]. A value of $\alpha = 0.50$ fm^{-1} is assumed in order to reproduce reasonably the binding energies for the initial nuclei with an appropriate effective interaction.

The effective nucleon-nucleon interaction typically used in this theory consists of three terms [3]:

(a) a repulsive, short-range Skyrme-type interaction that accounts for the bulk properties of the nucleus with a potential of the form:

$$v_{sk}(\mathbf{r},\mathbf{r}') = v_{02}\delta(\mathbf{r}-\mathbf{r}') + v_{03}\bar{\rho}^{\sigma}\left(\tfrac{1}{2}(\mathbf{r}+\mathbf{r}')\right)\delta(\mathbf{r}-\mathbf{r}'), \tag{2}$$

where $\bar{\rho}$ is the folded density:

$$\bar{\rho}(\mathbf{r}) = \sum_{i=1}^{A}\left(\frac{\alpha}{\sqrt{2\pi}}\right)^3 \mathrm{e}^{\alpha^2(\mathbf{r}-\mathbf{r}_i)^2/2}, \tag{3}$$

and v_{02}, v_{03}, and σ are adjustable parameters. The folded density has twice the width of the single-particle density.

(b) a long-range, attractive Yukawa-type interaction that is necessary to reproduce surface effects:

$$v_{yk}(\mathbf{r},\mathbf{r}') = v_{yk}^{0}\frac{\mathrm{e}^{-\mu|\mathbf{r}-\mathbf{r}'|}}{\mu|\mathbf{r}-\mathbf{r}'|}, \tag{4}$$

where v_{yk} and μ are adjustable parameters.

(c) an effective-charge Coulomb interaction:

$$v_C(\mathbf{r},\mathbf{r}') = \frac{e^2}{|\mathbf{r} - \mathbf{r}'|}, \tag{5}$$

where e is the elementary charge.

The parameters in the above equations are chosen such that the effective interaction is equivalent to a density-dependent nuclear equation-of-state with a potential of the following form:

$$U(\rho) = \alpha\left[\frac{\rho}{\rho_0}\right] + \beta\left[\frac{\rho}{\rho_0}\right]^\gamma, \tag{6}$$

where α, β, and γ are free parameters. This equation reproduces the saturation properties of infinite nuclear matter for a given value of nuclear compressibility, K. Typical values of K range from 144 to 380 MeV.

The initial projectile and target nuclei are prepared by randomly placing the nucleons in sphere of radius $R = 1.14 * A^{1/3}$ (A is the mass number of the nucleus), with a minimum distance between nuclei of 1.5 fm [3]. Using the Fermi-gas approximation and the local density of nucleons, the local Fermi momentum is calculated. The momentum of each particle is then chosen randomly between zero and the local Fermi momentum. The initial configuration of each nucleus is accepted if all particles are a certain minimum distance apart in phase space and the average binding energy is in the range -9.0 to -8.0 MeV/nucleon.

After initialization, the nuclei are boosted toward each other with the proper center-of-mass velocity. The position and momentum of each nucleon evolve under the influence of the mean field created by all other nucleons according to the classical equations of motion:

$$\frac{d\mathbf{r}_i}{dt} = \frac{\partial H}{\partial \mathbf{p}_i} \tag{7}$$

and

$$\frac{d\mathbf{p}_i}{dt} = -\frac{\partial H}{\partial \mathbf{r}_i}, \tag{8}$$

where H is the Hamiltonian of the system.

Two nucleons collide whenever they reach a minimum distance, d $\leq \sqrt{\sigma/\pi}$, where σ is the energy-dependent free nucleon-nucleon cross section [2]. The scattering angles are chosen randomly according to the measured angular distribution for elastic collisions. The Pauli exclusion principle is applied schematically by calculating the overlap between the Gaussian of a given nucleon and the Gaussians of all other nucleons. With the Gaussians normalized to one, a configuration is rejected with a probability, $P_b(\epsilon)$:

$$P_b(\epsilon) = \begin{cases} \epsilon, & \text{for } 0 \leq \epsilon \leq 1; \\ 1, & \text{for } 1 \leq \epsilon \end{cases} \tag{9}$$

where ϵ is the total overlap in position and momentum space. Since the correct phase-space occupation is maintained only on average, this treatment is only an approximation to the Pauli exclusion principle. The calculations are carried out over several time steps to a final time of around 300 fm/c. Many-particle correlations and density fluctuations cause the formation of clusters, which can be identified as fragments using a clustering algorithm [1].

QMD calculations have been successful at predicting experimentally observed mass yield, angular, and multiplicity distributions for high energy (E/A = 800 and 1050 MeV) Ne + Au collisions [3,4]. The theory also predicts sidewards flow [4] and the onset of multifragmentation [2], both of which have been observed experimentally. A major shortcoming of the model is that it underpredicts the observed IMF multiplicities (IMF: $3 \leq Z \leq 20$) [5]. This failure could result from a strong in-medium modification of the free nucleon-nucleon cross section which lowers the excitation energy of the system [3]. Another explanation is the fact that the theoretical heat capacity is much higher than that of true fermionic systems [5]. A system that can store a larger amount of energy will preferentially de-excite by evaporation of light charged particles as opposed to a multifragment break-up. An improved treatment of the Pauli exclusion principle is needed in order to reproduce more closely the thermodynamic properties of actual many-fermion systems.

2. Boltzmann-Uehling-Uhlenbeck Model

The Boltzmann-Uehling-Uhlenbeck (BUU) Model predicts the average trajectory of the nucleon phase-space density in a heavy-ion collision [6]. The phase-space density evolves under the influence of the mean-field potential created by all of the nucleons. The temporal evolution of the one-body phase space distribution, f, is obtained by solving the BUU equation:

$$\frac{\partial f_1}{\partial t} + \mathbf{v} \cdot \nabla_{\mathbf{r}} f_1 - \nabla_{\mathbf{r}} U \cdot \nabla_{\mathbf{p}} f_1 = \tag{10}$$

$$\frac{4}{(2\pi)^3} \int d^3k_2 d^3k_3 d\Omega v_{12} \frac{d\sigma}{d\Omega} \delta^3(\mathbf{k_1} + \mathbf{k_2} - \mathbf{k_3} - \mathbf{k_4})$$

$$\times \Big[f_1 f_2 (1 - f_3)(1 - f_4) - f_3 f_4 (1 - f_1)(1 - f_2) \Big].$$

The collision integral (right hand side of the BUU equation) depends upon the relative velocity, v_{12} of the colliding nucleons, which have initial momenta $\mathbf{k}_1$ and $\mathbf{k}_2$ and final momenta $\mathbf{k}_3$ and $\mathbf{k}_4$. The in-medium nucleon-nucleon differential cross section, $\mathrm{d}\sigma/\mathrm{d}\Omega$, is proportional to the energy-dependent free nucleon-nucleon differential cross section, $\mathrm{d}\sigma_{NN}/\mathrm{d}\Omega$ ($\mathrm{d}\Omega$ is the element of solid angle). The effects of the Pauli Principle are represented by the occupancy (f) and blocking (1-f) terms. The nuclear mean-field potential, U, is the density-dependent nuclear equation-of-state (EOS); the parameter sets are chosen to correspond to an incompressibility of K = 210 MeV (soft EOS), K = 235 (medium EOS), or K = 380 (stiff EOS) [7].

The BUU equation is solved using a pseudo-particle simulation, with each nucleon represented by 100 point-like test particles [6]. Cell sizes of 1 fm^3 and $(2\pi\hbar)^3$ are used to calculate the local densities in coordinate and phase space, respectively. The initially separated projectile and target nuclei are boosted towards each other with the appropriate center-of-mass velocity. The A_T + A_P particles follow curved trajectories under the influence of the mean field and undergo collisions which do not violate the Pauli exclusion principle. The simulations successfully describe pre-equilibrium nucleon emission, intrinsic excitation energies, and pion and strangeness production [4,7]. This approach has also been used to study phenomena related to initial compression, such as collective sidewards flow, transverse momentum transfer, and collective radial motion [3,4].

The technique of ensemble averaging is used in solving the BUU equation in order to smear out the large fluctuations of the mean field potential. Solutions obtained using this method give the average trajectory of the one-body phase-space density. Due to this lack of two-body or higher correlations, the BUU equation cannot describe the formation of fragments [8]. Recently efforts have been made to incorporate dynamic fluctuations by replacing the original collision term with a stochastic term [9]. Such fluctuations of the one-body distribution function are an essential ingredient for cluster formation [5].

B. Statistical Theories

1. Expanding-Emitting Source Model

The Expanding-Emitting Source (EES) Model is a rate-equation approach that also incorporates a temporal evolution of the excited nuclear system [10,11]. A system initially at normal nuclear matter density, ρ_0, undergoes isotropic expansion in response to thermal pressure. The expansion is opposed by an effective nuclear restoring force. Statistical decay during the expansion is treated by calculating the density of the residue at each instant in time, ρ, and using density-dependent transition rate expressions [10]. The instantaneous density and the emission process are coupled: changes in density affect the rate of particle emission which, in turn, leads to variations in the density through conservation of energy.

The calculation requires four initial conditions: the mass, charge, excitation energy and radial expansion velocity of the source. The density of energy states of the excited system is assumed to be the same as for a finite temperature Fermi gas [11]. The nuclear binding forces are parametrized using the following equation-of-state, which relates the binding energy per nucleon, $\mathrm{E}(\rho)/\mathrm{A}$ to the liquid drop binding energy, $\mathrm{E}_{ld}(\rho_0)$:

$$\mathrm{E}(\rho)/\mathrm{A} = \mathrm{E}_{\mathrm{ld}}(\rho_0)/\mathrm{A} + \left(\frac{K}{18}\right)\left(1 - \frac{\rho}{\rho_0}\right)^2, \tag{11}$$

where the finite nuclear compressibility, K, is an input parameter. For a value of K=144 MeV, the binding energy per nucleon has a parabolic dependence on the density and varies between $\mathrm{E}_{ld}(\rho_0)$ = -8 MeV at $\rho = \rho_0$ and zero at vanishing density. If the initial excitation energy of the residue is not sufficient to overcome this restoring force, the system undergoes density oscillations. In order for multiple fragments to be emitted, the free energy of the fragments must be lower than the free energy of the residue in which they form, a condition that occurs at low density [11]. Thus, the fragment emission rate sharply increases as the system reaches a density minimum, with most of the fragments being emitted during the first density minimum [7].

The dependence of the IMF multiplicity on the total charged-particle multiplicity in the reactions ^{129}Xe + ^{197}Au at E/A = 50 MeV and ^{36}Ar + ^{197}Au at E/A = 35 - 100 MeV have been reproduced using the EES model [7,12]. A system at low density is required to reproduce the large IMF multiplicities that are observed in these reactions. These comparisons provide information about the compressibility of the emitting system. With a soft equation-of-state (K = 144 MeV), the model is also successful in reproducing the IMF, charge and energy distributions in the reaction ^{3}He + ^{nat}Ag over the bombarding energy range 0.27 to 3.6 GeV [13]. The calculations predict the broadening of the Coulomb peaks toward lower energies and the flattening of the spectral tails that is observed with increasing bombarding energy.

Despite these successes, the EES model does not address the initial energy deposition that led to the excited residue. In particular, the initial radial kinetic energy is strongly influenced by the compression-decompression dynamics that occur in the early stages of a heavy-ion collision [7]. The model ignores pre-equilibrium emission and assumes that the residue is initially at thermal equilibrium. Additional aspects that are not treated are the effects of angular momentum on the fragment emission and sequential decay of excited fragments. These effects must be incorporated in order to achieve a complete temporal history of the multifragmentation process.

2. Microcanonical Fragmentation Model

The Microcanonical Fragmentation (McFrag) Model is a Monte Carlo method for calculating the break-up of a highly excited nucleus ($E^* \approx 1$ - 20 MeV/A) that has reached statistical equilibrium [14]. The system has expanded to low density and reached a "freeze-out" configuration where the average distance between fragments is slightly larger than the range of nucleon exchange. The statistical weight for each possible break-up scenario is evaluated at a microcanonical level: all final states that conserve the total energy, momentum, mass and charge are equally probable. Successive events are generated by making a small change in the previous decay channel (for e.g., the position of a single fragment). By using this Metropolis Monte Carlo technique [15], the code spends most of its time in the more important, more highly weighted areas of phase space.

The fragments are formed in a sphere of radius $R = 2.08 * A^{1/3}$ with an average interfragment distance of ≈ 2 fm [16]. The total energy of the system, E_{tot}, consists of the following components:

$$E_{tot} = E_C + E_B + E^* + K + K_\nu, \tag{12}$$

where E_c is the Coulomb energy of the fragments, E_B the binding energy, E^* the internal excitation energy of the fragments, K the kinetic energy of the fragments and K_ν the kinetic energy of the prompt neutrons [17]. This available energy is distributed over the internal and collective degrees of freedom and a statistical weight is calculated for each possible configuration. The total weight is a product of factors that take into account the number of partitions into N_c fragments, along with the momentum distribution, positions, and internal excitation of these fragments. Additional factors represent the weight due to the phase space occupied by prompt and evaporated particles. The excited primary fragments de-excite by evaporating neutrons, protons, and alpha particles as they undergo disassembly along time-dependent Coulomb trajectories.

At low excitation, the fragment yield is dominated by evaporation from a heavy residue. At intermediate excitation ($E^* \approx 400$ - 600 MeV), fission is the most important decay channel. Above 600 MeV, McFrag calculations predict the "cracking" of the nucleus into three or more IMFs. McFrag has successfully predicted the mass yields and isobaric distributions of fragments produced in the reaction p + ^{131}Xe at E

= 80 to 350 GeV [14]. The code also reproduces the dependence of IMF multiplicity on Z_{bound} (the total charge of all bound clusters) in the reaction Au + Cu at E/A = 600 MeV, in contrast to sequential binary decay models [18]. Although fragment-fragment correlation functions constructed from McFrag calculations agree well with experimental correlation functions constructed for the reactions ^{128}Xe + ^{nat}Cu at E/A = 600 MeV and ^{36}Ar + ^{197}Au at E/A = 110 MeV, the predicted kinetic energy spectra of the fragments do not reproduce the measured energy spectra [18,19]. The reduced Coulomb repulsion between fragments in the simultaneous breakup at low density and the lack of a radial expansion velocity in the model result in calculated fragment energy spectra that peak at a lower energy than experimentally observed spectra [20]. In contrast to the EES model, all of the fragments are emitted from a source at fixed excitation energy and thus have a narrower range in energies than is needed to reproduce the data.

C. Summary

Dynamical models of multifragmentation are useful in describing the energy deposition phase of intermediate-energy heavy-ion collisions. They are particularly successful in reproducing pre-equilibrium emission, compression phenomena, and intrinsic excitation energies during the formation of the highly excited nuclear system. Nuclei simulated in dynamical models are unstable at times longer than a few hundred fm/c due to numerical instabilities in the calculations. These approaches neglect the higher order correlations essential to fragment formation and stability.

Statistical models are successful in reproducing the IMF yields and source properties during the de-excitation of a highly excited nuclear system. The initial characteristics of the emitting source, such as charge, mass, and excitation energy, are input parameters and the system is assumed to be initially at thermal equilibrium.

The initial nucleus-nucleus collisions that led to the formation of the excited nuclear system are ignored in this type of model.

In an effort to overcome the difficulties associated with the above approaches, hybrid models have been constructed which incorporate the successful aspects of dynamical and statistical models. The predictions of a dynamical code provide initial conditions for statistical calculations. The coupling of the two different types of models in a hybrid approach has provided insight into the goal of a complete description of multifragmentation, from the initial stages of energy deposition to the final break-up of the highly excited nuclear system.

REFERENCES

[1] C.O. Dorso and J. Aichelin, Phys. Lett. **B345**, 197 (1995).

[2] S.R. Souza *et al.*, Nucl. Phys. **A571,** 159 (1994).

[3] J. Aichelin *et al.*, Phys. Rev. C **37**, 2451 (1988).

[4] J. Aichelin and H. Stöcker, Phys. Lett. **B176**, 14 (1986).

[5] R. Donangelo and S.R. Souza, Phys. Rev. C **52**, 326 (1995).

[6] W. Bauer *et al.*, Phys. Rev. C **34**, 2127 (1986).

[7] D. Bowman *et al.*, Phys. Rev. C **46**, 1834 (1992).

[8] B. Heide and H.W. Barz, Nucl. Phys. **A588,** 918 (1995).

[9] Ph. Chomaz *et al.*, Phys. Rev. Lett. **73**, 3512 (1994).

[10] W.A. Friedman, Phys. Rev. Lett. **60**, 2125 (1988).

[11] W.A. Friedman, Phys. Rev. C **42**, 667 (1990).

[12] R.T. de Souza *et al.*, Phys. Lett. **B268,** 6 (1991).

[13] K. Kwiatkowski *et al.*, Phys. Rev. C **49**, 1516 (1994).

[14] D.H.E. Gross, Zhang Xiao-ze, Xu Shu-yan, Phys. Rev. Lett. **56**, 1544 (1986).

[15] N. Metropolis *et al.*, J. Chem. Phys. **27**, 1078 (1953).

[16] D.H.E. Gross and Xiao-ze Zhang, Phys. Lett. **B161**, 47 (1985).

[17] Xiao-ze Zhang *et al.*, Nucl. Phys. **A461**, 641 (1987).

[18] O. Schapiro and D.H.E. Gross, Nucl. Phys. **A573** 143 (1994).

[19] D. Fox *et al.*, Phys. Rev. C **50**, 2424 (1994).

[20] K. Kwiatkowski *et al.*, Phys. Rev. Lett. **74,** 3756 (1995).

CHAPTER 3

EXPERIMENTAL DETAILS

The experiment was performed at the National Superconducting Cyclotron Laboratory at Michigan State University (MSU) [1]. Beams of ^{84}Kr accelerated by the K1200 cyclotron to E/A = 35, 55, and 70 MeV were extracted with beam intensities of 1-2 x 10^8 particles per second and were focused onto self-supporting ^{197}Au targets. The target thickness was 1.3 mg/cm^2 for the experiments at E/A = 35 and 55 MeV and 4 mg/cm^2 at E/A = 70 MeV. Charged particles emitted in the angular range $5.4° \leq \theta_{lab} \leq 160°$ were detected with the combined MSU Miniball/Washington University Miniwall 4π phoswich detector array [2]. For each of the rings $\theta_{lab} \geq 25°$, a single Miniball detector was replaced with an ion-chamber telescope [3]. These detectors provided reference single particle distributions for comparison to the distributions measured by the Miniball/Miniwall 4π array, particularly near threshold.

Hardware discriminator thresholds of 5 MeV and 10 MeV were imposed on the Z = 1 particles for the Miniball and Miniwall, respectively, to avoid triggering on low energy electrons. Double hits consisting of a light charged particle ($Z \leq 2$) and an intermediate mass fragment (IMF: $3 \leq Z \leq 20$) or of two IMF's were identified as a single IMF. Double hits consisting of two light charged particles were identified as a single light charged particle. Multiple hits were estimated to reduce the charged-particle multiplicity and the IMF multiplicity by 15-25% and 1.5-2.5%, respectively, depending on incident energy.

A. Miniball/Miniwall 4π Detector Array

The Miniball/Miniwall detector system consists of 296 plastic-scintillator-CsI(Tl) phoswhich detectors mounted in 15 independent rings coaxial about the beam axis. A half-plane section of the combined system is displayed in Figure 3.1. Each ring is labeled (rings 3′-11 for the Miniball and rings 12-17 for the Miniwall) and the number of detectors in each ring is given in parenthesis. The detectors in a given ring are identical in shape and have the same polar angle with respect to the beam axis. The solid angles and coverage in polar and azimuthal angles for individual detectors are listed in Table I. The total geometric efficiency of these detectors is $\approx$ 90% of 4π. Ring 17 was not used in the data analysis.

An artist's perspective of the original Miniball array is shown in Figure 3.2. In this experiment, rings 1 and 2 of the Miniball were replaced with the Washington University Miniwall detector array to provide increased granularity at the most forward angles [4,5]. Laboratory angles from θ_{lab} = 25° - 160° were covered by Miniball detectors which consisted of 40 μm plastic scintillator foils in front of 2 cm thick CsI(Tl) crystals. The thresholds for these detectors were $E_{th}/A \approx 2$ MeV (4 MeV) for $Z = 3$ ($Z = 10$) particles, respectively. Detectors in the Miniwall, which covered the angular range $5.4° \leq \theta_{lab} \leq 25°$, consisted of 80 μm thick plastic scintillator foils in front of 3 cm thick CsI(Tl) crystals. The energy thresholds for these detectors were $E_{th}/A \approx 4$ MeV (6 MeV) for $Z = 3$ ($Z = 10$) particles, respectively.

A schematic diagram of an individual detector is given in Figure 3.3. The back face of the CsI(Tl) crystal is glued with optical cement to a flat light guide made of ultra-violet transparent (UVT) plexiglas (12 mm thick) and a second cylindrical piece of UVT plexiglas (9.5 mm thick and 25 mm diameter). The cylindrical light guide is then glued to the front window of the photomultiplier tube. The cylindrical light guide and photomultiplier tube are surrounded by a cylindrical μ-metal shield (not shown in Figure 3.3). For Miniwall detectors and Miniball detectors in rings 3′-8, the front face of the phoswich assembly was covered by an aluminized mylar foil (0.15 mg/cm^2 mylar and 0.02 mg/cm^2 aluminum) to increase reflection at the front surface. At backward angles (rings 9-11) where the larger solid angles lead to higher electron, X-ray, and γ-ray counting rates, the front face was covered by an absorber foil (Pb-Sn alloy with 5 mg/cm^2 areal density) to suppress signals from these radiations.

1. Particle identification

The temporal decay of the light output from the CsI(Tl) crystal depends upon the atomic number, energy and mass of the detected particle [6–8]. Therefore, element identification can be obtained by pulse shape analysis of the detector signal [2]. The fluorescent light from the CsI(Tl) crystal can be expressed as a combination of exponentials:

$$L(t) = L_s exp(-t/\tau_s) + L_f exp(-t/\tau_f), \tag{1}$$

where L(t) is the light pulse amplitude at time t and L_s and L_f are the total light amplitudes for the slow and fast components, respectively [9]. While the slow time constant, $\tau_s \approx 7$ μs, is independent of the ionization density of the generated by the detected particle, the value of the fast decay constant, $\tau_s \approx$ 0.4-0.7 μs, and the relative intensity, L_f/L_s, both vary with the particle type. The ratio of the pulse heights at two different times can therefore be used to discriminate between different particle types.

Identification of particles with Z> 3 is difficult using this technique [9]. To improve the detection capabilities for particles of higher atomic number, the relative intensity, L_f/L_s, can be modified by the adding a thin plastic scintillator foil to the front face of the CsI(Tl) crystal. The light output from the foil increases with the Z of the detected particle. The superposition of this signal on the fast component of the CsI(Tl) crystal leads to good atomic number separation for particles up to Z=20 [4,5].

The shape of the anode signal from the photomultiplier tube is shown schematically in Figure 3.4. The "fast" component is due to scintillation from the plastic foil; the "slow" and "tail" components are due to the two-component scintillation in the CsI(Tl) crystal. The time gates for the charge integration of the three different components are indicated in Figure 3.4. The atomic number of the detected particles is determined by plotting the "fast" component versus the "slow" component, as shown in Figure 3.5. The distinct bands visible in that figure correspond to different elements up to Z≈15. The atomic number lines were linearized in order to draw the charged-particle gates.

The isotopes of hydrogen and helium are identified using the "tail" versus "slow" spectrum, as shown in Figure 3.6 [10]. The lower left portion is expanded in Figure 3.7 to show the Z=1 isotopes in greater detail. Although the Z=1 and Z=2 isotopes are evident in those figures, the different masses are difficult to separate in the "tail" versus "slow" representation. To separate the hydrogen and helium isotopes more easily, the "PDT" function was constructed [5]. The necessary parameters are shown schematically in Figure 3.8. The two lines $\text{tail}_1(\text{slow})$ and $\text{tail}_2(\text{slow})$ are drawn to encompass the entire area of the spectrum. The PDT function is given by:

$$PDT = 512 * (\Delta/\Delta_{max}), \tag{2}$$

where

$$\Delta = tail_1 - tail_r, \tag{3}$$

$$\Delta_{max} = tail_1 - tail_2. \tag{4}$$

The parameter tail_r is constructed using:

$$tail_r = tail + \delta, \tag{5}$$

where δ is a random number between -0.5 and 0.5, added to remove digitization from the displayed spectra. The resulting "slow" versus "PDT" spectrum is shown in Figure 3.9; the p, d, and t isotopes of hydrogen and the ^{3}He and ^{4}He isotopes of helium are clearly distinguishable. The dark line below the p, d, and t lines are hydrogen isotopes that have punched through the CsI(Tl) crystal. The line between the helium and lithium particles is due to double alpha hits in the detector. The same particle-identification procedures were also applied to the Miniwall detectors.

2. Energy calibration

The response function of the CsI(Tl) detectors in the Miniball/Miniwall detector array have been calibrated with different types of light charged particles and heavy ions [10,11]. Miniball detectors in rings forward of $\theta_{lab} = 40°$ were calibrated by measuring the elastic scattering of ^{4}He (E/A = 4.5-20 MeV), ^{6}Li (E/A = 8.9 MeV), ^{10}B (E/A = 15 MeV), ^{12}C (E/A = 6-20 MeV), ^{16}O (E/A = 16 and 20 MeV), ^{20}Ne (E/A = 10.6-19.8 MeV, and ^{35}Cl (E/A = 8.8-15 MeV) beams from a ^{197}Au target. Miniball detectors in rings backward of $\theta_{lab} = 40°$ were calibrated using the energies of light charged particles punching through the CsI(Tl) crystal and extrapolations of the average response of detectors at more forward angles. In addition, selected Miniball and Miniwall detectors were bombarded directly with low intensity ^{6}Li, ^{12}C, and ^{18}O beams ranging in energy from E/A = 22-80 MeV [13].

The scintillation light output, L, has been parameterized as:

$$L(E,Z) = \alpha(Z)E + \beta(Z)\left[e^{-\gamma(Z)E} - 1\right], \tag{6}$$

where E is the energy deposited in the CsI crystal, Z is the atomic number of the incident ion, and the adjustable parameters α, β, and γ are dependent upon the atomic number [8]. This functional form reproduces most of the nonlinear behavior of the CsI(Tl) light output at low energies as well as at large atomic number. The linear behavior at higher energies up to E/A ≈ 25 MeV is also well described by Eq. 6. The calibration data along with the parameterized fits are presented in Figure 3.10.

The error bars indicate the spread in multiple calibration points. The calibration is accurate to 5-10% at lower energies and 10-15% for energies larger than 30 MeV per nucleon. Additional details about the calibration procedure can be found in Ref. [13].

B. Ion-Chamber Telescopes

A cross-sectional view of a low threshold ion-chamber telescope is shown in Figure 3.11. The design of the telescope is patterned after earlier designs by Kwiatkowski *et al.* [12]. The housing consists of four pieces of 1 mm thick stainless steel welded to stainless steel flanges at the front and back faces of the detector. The three elements of the telescope are: (1) a 55 mm long axial-field ionization-chamber operated at 30 torr of CF_4, (2) a 500 μm thick passivated Si detector, and (3) a 3 cm thick CsI(Tl) crystal, read out by a photodiode [3]. The corresponding thresholds for particle identification are $E_{th}/A \approx 0.8$ MeV for $Z \leq 20$. The entrance window is a 1.5 μm aluminized Mylar foil which is capable of sustaining a differential pressure of at least 140 Torr without support wires. The edges of the axial field are shaped by seven copper rings; the center copper ring serves as the anode. Because this design has an inherently weak transverse field, a doubly aluminized polyethylene film (areal density 50-155 $\mu g/cm^2$) is stretched across the anode ring to provide more efficient charge collection.

The 500 μm ion-implanted, SiO_2 passivated-silicon detector is mounted directly behind the ion chamber on a Plexiglas spacer. This spacer provides alignment with the CsI(Tl) crystal and precise positioning with respect to the back flange of the detector. The Si detector, which has an active area of 30 mm X 30 mm, is mounted in transmission mode on a printed circuit board. The preamplifiers for the ionization chamber and silicon detector were designed by Michigan State University (MSU-NSCL). The preamplifiers are located external to the can, approximately 25 cm away, to limit the importance of cable capacitance.

The CsI(Tl) scintillator crystal is wrapped with Teflon tape around the sides and 1.5 μm aluminized Mylar on the front face (to provide reflection of scintillation). The back face of the CsI(Tl) crystal is optically coupled to a Plexiglas light guide which is in turn optically coupled to a 2 cm x 2 cm photodiode. Because the gain of the photodiode is unity, the charge out of the photodiode is processed through a charge-sensitive preamplifier (MSU-NSCL design) located in the gas volume. To reduce sensitivity of FETs in the preamplifier to electrical discharge in the gas volume, the preamplifier was potted in silicon elastomer (Dow-Corning Sylgard 184).

1. Particle Identification

Elemental and isotopic identification of charged particles entering the ion-chamber telescope was achieved by utilizing the ΔE-E technique [3]. For a charged particle traversing a detector medium, the stopping power (-dE/dx) is defined as the instantaneous rate of energy loss per unit length of matter [14]. The stopping power is a function of the ion's atomic number (Z), energy (E), and mass (M):

$$-\left(\frac{dE}{dx}\right) \propto \frac{MZ^2}{E}. \tag{7}$$

A plot of the energy loss (ΔE) in a transmission detector versus the residual energy (E) in a stopping detector is a series of curves corresponding to the different elements. As can be seen in Figure 3.12, the gas detector provides elemental identification from Z=1 to Z=14. If the transmission detector is of uniform thickness and is accurately calibrated, mass separation is possible. Due to the good planarity of the Si(IP), isotope separation can be achieved through oxygen (see Figure 3.13) and, in some cases, neon. The additional bands above the Z=1 and Z=2 isotopes in Figure 3.13 are due to pileup within the same detector of particles which originate from different beam pulses. These events can be rejected in future experiments by use of a multiple-hit time-to-digital converter.

2. Energy Calibration

The critical element in the energy calibration of the ion-chamber telescope is the Si(IP) detector. The Si(IP) crystal was calibrated using a precision electronic pulser and primary beams of ^{4}He, ^{12}C, and ^{16}O accelerated to $E/A = 22$ MeV and degraded to energies as low as $E/A = 12$ MeV [3]. In addition, the characteristic energies at which specific ions punch through the silicon wafer were utilized in the calibration. The different techniques resulted in consistent energy calibrations within 1-2% for the Si element. The ionization-chamber section of the telescope was calibrated using a precision pulser. As a check of the uncertainty in this method, points were selected on the characteristic elemental curves in the ionization chamber-Si(IP) ΔE-E two dimensional plot. The ionization chamber was then calibrated using the energy deposited in the Si(IP) crystal and energy loss calculations. Calibrations using these two methods agree to within 5 and 10% for the ionization-chamber element. Since the amount of energy loss in the ionization chamber is of order a few tenths of an MeV, the accuracy of the calibration for the total energy is essentially determined by the Si calibration.

The CsI(Tl) detector was exposed to direct beams of d, ^{4}He, ^{12}C, and ^{16}O accelerated by the K1200 cyclotron at Michigan State University. In Figure 3.14, the measured light output deposited by these beams in addition to punchthrough p, d, t, ^{3}He, and ^{4}He particles is plotted as a function of the energy deposited in the crystal. The solid line in both panels of the figure represents a linear fit to the light charged particles. The deviation of the oxygen and carbon data from the solid line is probably due to a "quenching" effect [15]. The effect is more evident in the lower panel where the thinner Si(IP) detector (136 μm) results in a lower threshold for particles entering the the CsI(Tl). Calibration of the CsI(Tl) detector for heavy ions requires careful attention to account for the quenching effect.

In the next chapter, the atomic number and energy distributions measured in the Miniball/Miniwall detectors and ion-chamber telescopes are compared. In particular, the effects of energy thresholds on these distributions are explored. The atomic number, energy, and angular distributions are then used to characterize the sources of fragment emission in the ^{84}Kr + ^{197}Au collisions.

TABLES

Table 3.I. Coverage in solid, polar, and azimuthal angles for individual detectors in the Miniball/Miniwall array. The Miniball rings are labeled 3′-11; the Miniwall rings are labeled 12-17. Ring 17 was not used in this experiment.

Ring	# Detectors	θ (deg)	$\Delta\theta$	$\Delta\phi$	$\Delta\Omega$(msr)	IC $\Delta\Omega$(msr)	Si (μm)
3′	28	28.0	6.0	12.86	11.02	5.52	494.0
4	24	35.5	9.0	15.0	22.9	9.76	494.0
5	24	45.0	10.0	15.0	30.8	13.98	494.0
6	20	57.5	15.0	18.0	64.8	21.69	136.0
7	20	72.5	15.0	18.0	74.0	23.99	494.0
8	18	90.0	20.0	20.0	113.3	23.99	494.0
9	14	110.0	20.0	25.71	135.1	23.99	494.0
10	12	130.0	20.0	30.0	127.3	23.99	494.0
11	8	150.0	20.0	45.0	125.7	23.99	494.0
12	24	21.88	6.25	15.0	10.64		
13	24	16.63	4.25	15.0	5.56		
14	26	13.0	3.0	13.85	2.85		
15	22	10.0	3.0	16.36	2.59		
16	16	6.95	3.1	22.5	2.57		
17	16	4.38	2.05	22.5	1.11		

REFERENCES

[1] G.F. Peaslee *et al.*, Phys. Rev. C **49**, R2771 (1994).

[2] R.T. de Souza *et al.*, Nucl. Instr. Meth.**A295**, 109 (1990).

[3] D. Fox *et al.*, Nucl. Instr. Meth.**A368**, 709 1996.

[4] C. Williams, Ph.D. Thesis, Michigan State University (1996).

[5] W.C. Hsi, Ph.D. Thesis, Michigan State University (1995).

[6] M.L. Halbert, Phys. Rev. **107**, 647 (1957).

[7] D.G. Sarantites *et al.*, Nucl. Instr. Meth. **A264**, 319 (1988).

[8] N. Colonna *et al.*, Nucl. Instr. Meth. **A321**, 529 (1992).

[9] J. Alarja *et al.*, Nucl. Instr. Meth. **A242**, 352 (1986).

[10] Y.D. Kim, Ph.D. Thesis, Michigan State University (1991).

[11] L. Phair *et al.*, Nucl. Phys. **A564**, 453 (1993).

[12] K. Kwiatkowski *et al.*, Nucl. Instr. Meth. **A299**, 166 (1990).

[13] C. Schwarz *et al.*, NSCL Annual Report, 248 (1993).

[14] P. Marmier and E. Sheldon, Physics of Particles and Nuclei (Academic Press, New York, 1970).

[15] D. Fox *et al.*, Nucl. Instr. Meth. **A374**, 63 (1996).

FIGURES

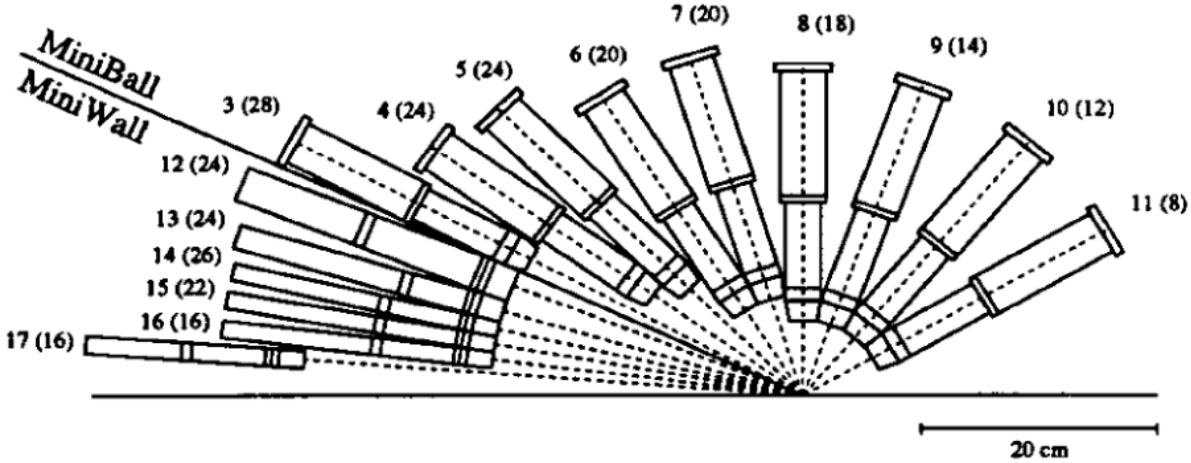
MiniBall
MiniWall
3 (28)
4 (24)
5 (24)
6 (20)
7 (20)
8 (18)
9 (14)
10 (12)
11 (8)
12 (24)
13 (24)
14 (26)
15 (22)
16 (16)
17 (16)
20 cm

Figure 3.1. Half-plane section of the Miniball/Miniwall detector array. Each ring is labeled (rings 3′-11 for the Miniball and rings 12-17 for the Miniwall) and the number of detectors in each ring is given in parentheses.

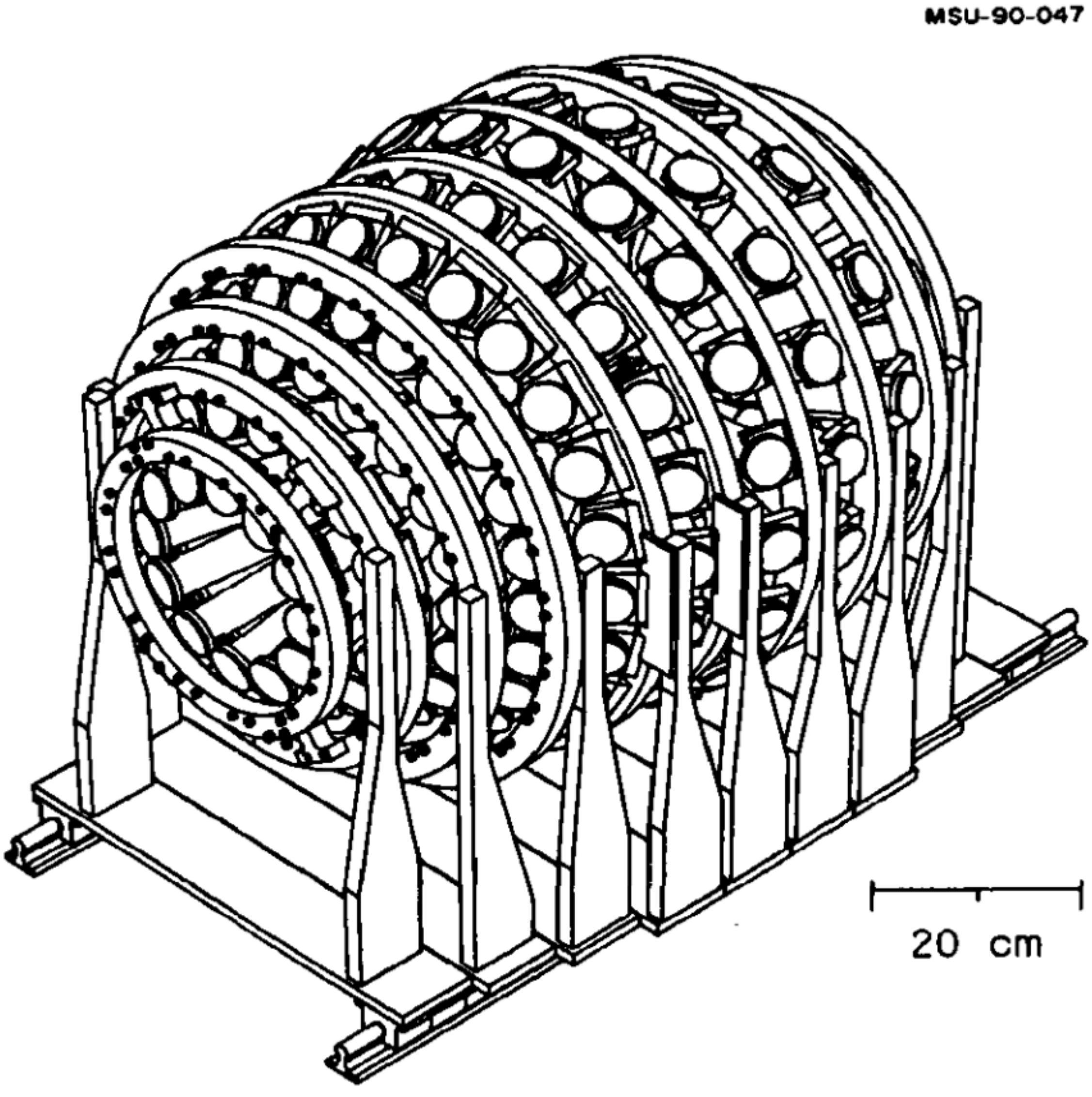
MSU-90-047
20 cm

Figure 3.2. Artist's perspective of the original Miniball detector array.

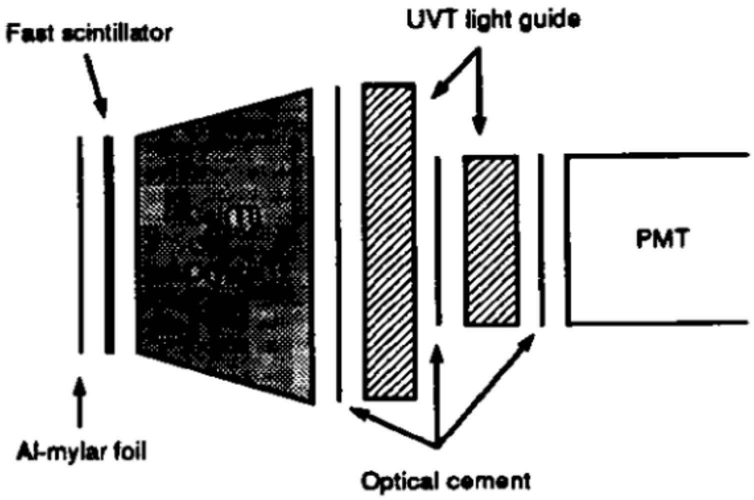
Fast scintillator
UVT light guide
PMT
Al-mylar foil
Optical cement

Figure 3.3. Schematic diagram of an individual phoswich detector.

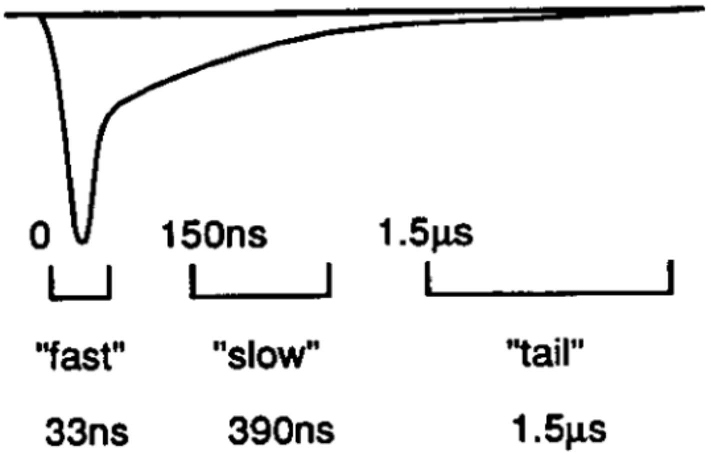
0
150ns
1.5μs
"fast"
"slow"
"tail"
33ns
390ns
1.5μs

Figure 3.4. Schematic anode signal from the photomultiplier tube of a phoswich detector along with the timing and widths of the "fast", "slow", and "tail" gates.

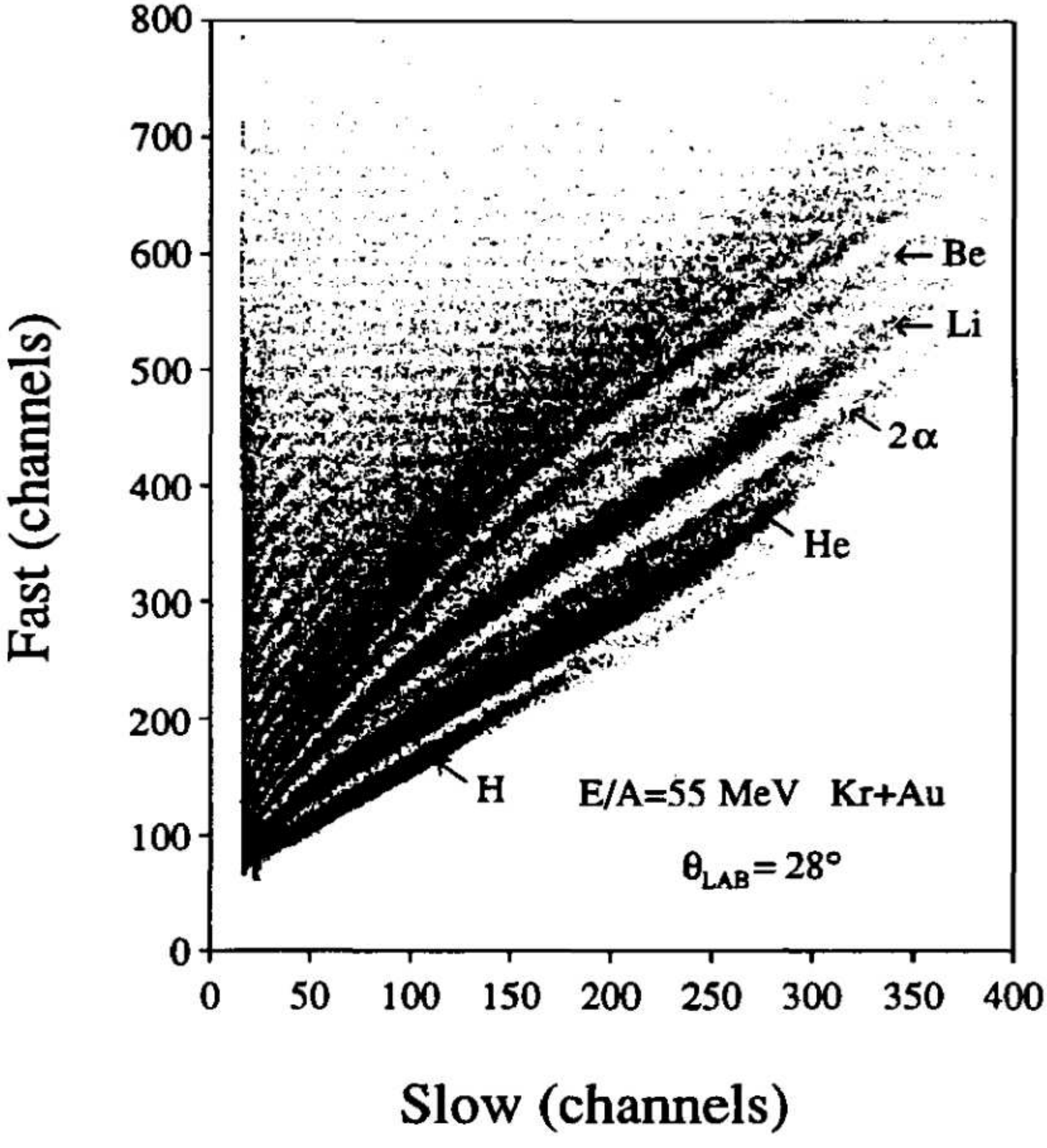

Figure 3.5. "Fast" versus "slow" spectrum measured in ring 3′ (θ_{lab} = 28 °) in the reaction ^{84}Kr + ^{197}Au at E/A = 55 MeV

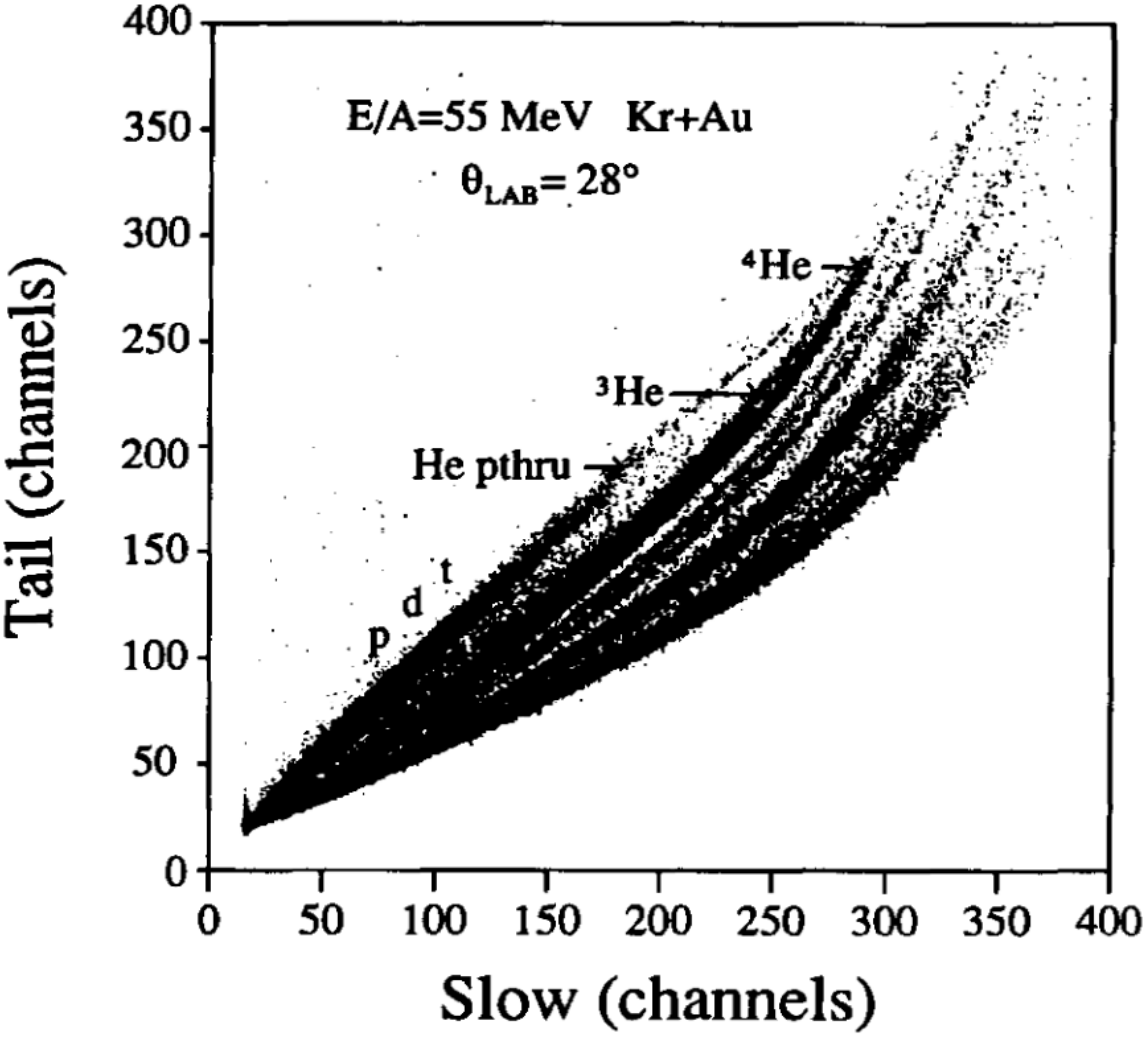

Figure 3.6. "Tail" versus "slow" spectrum measured in ring 3′ (θ_{lab} = 28 °) in the reaction ^{84}Kr + ^{197}Au at E/A = 55 MeV

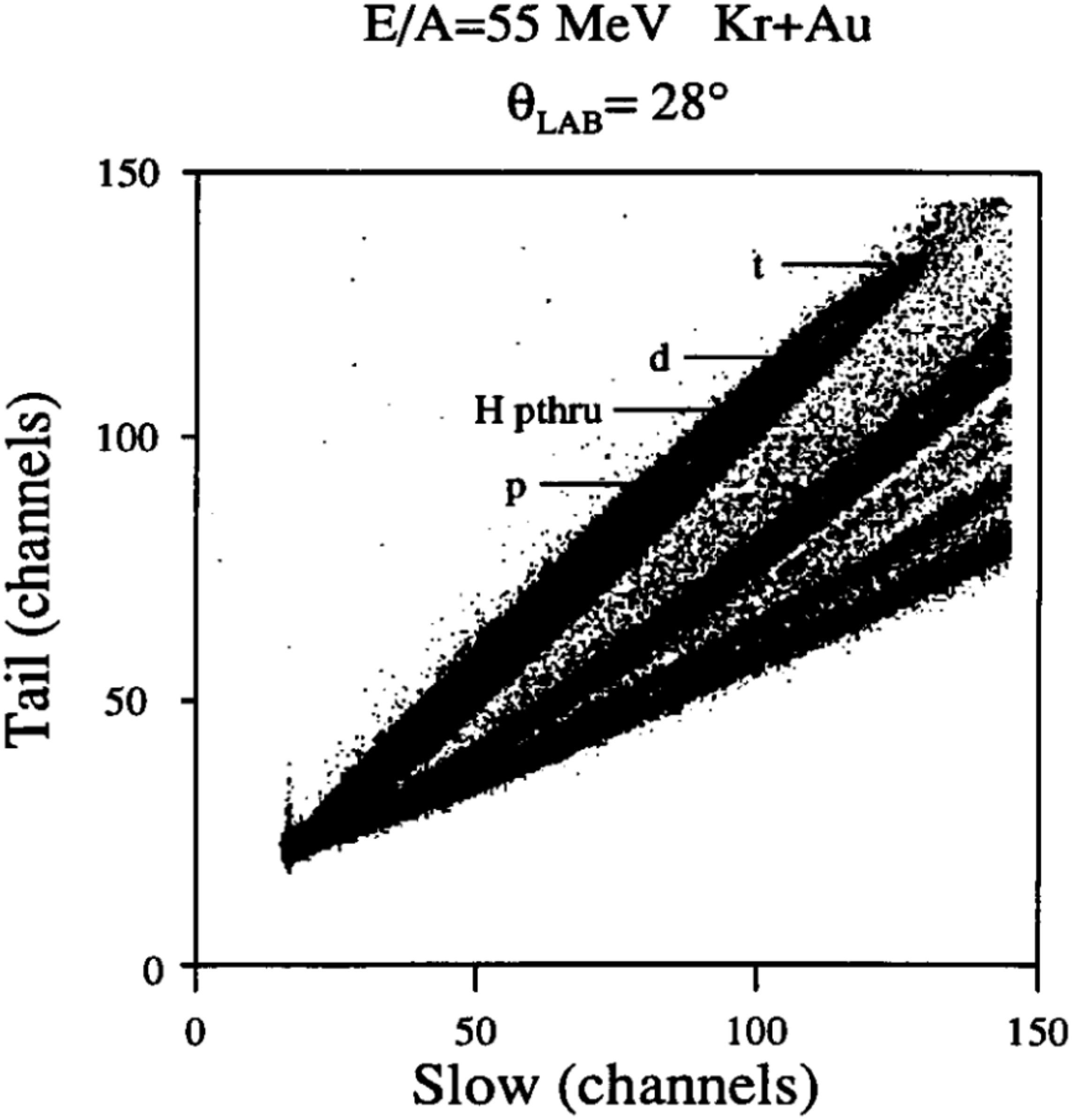

Figure 3.7. Expanded view of the lower left region in Figure 3.6 showing the Z=1 isotopes.

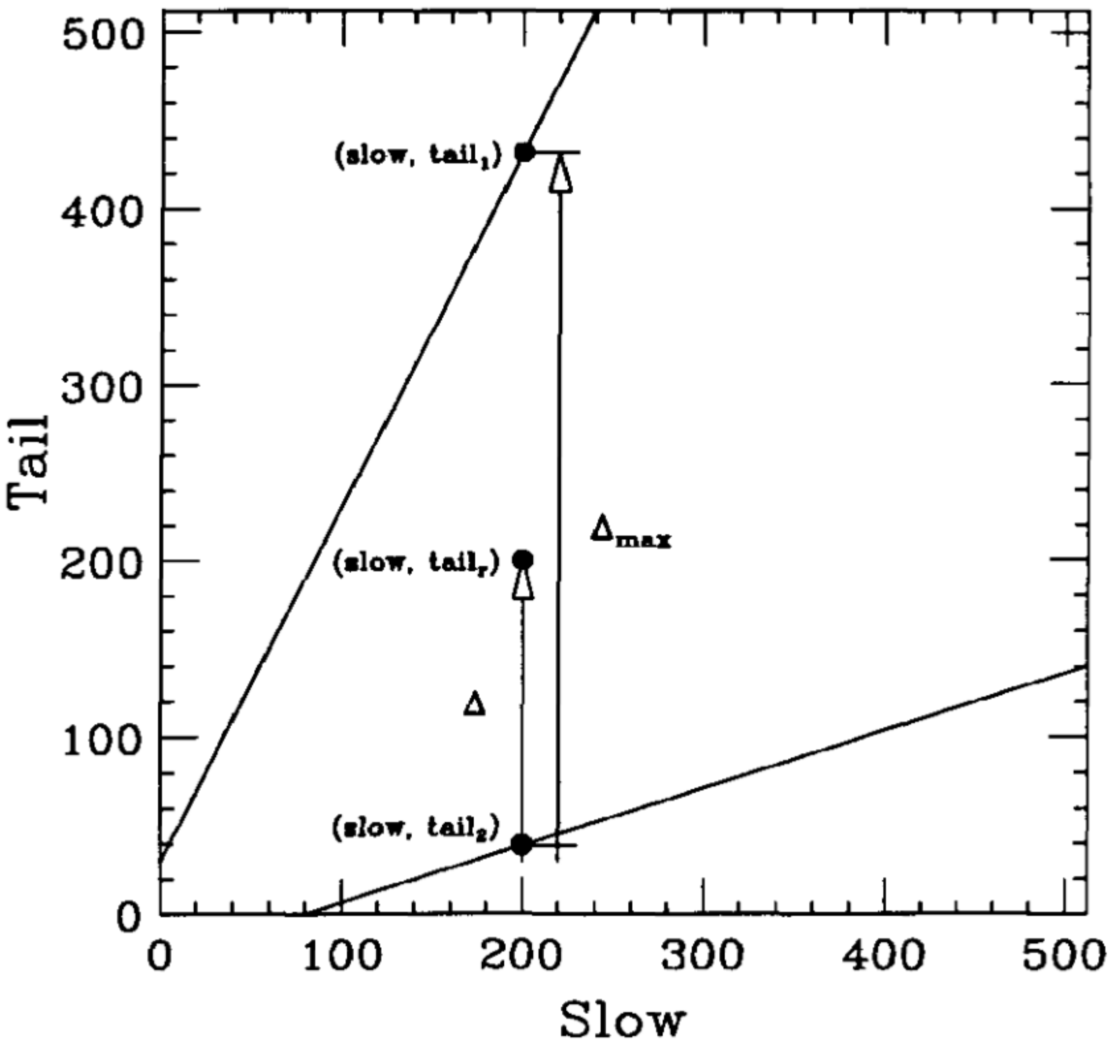

Figure 3.8. Schematic tail versus slow plot which describes variables used in constructing the PDT function.

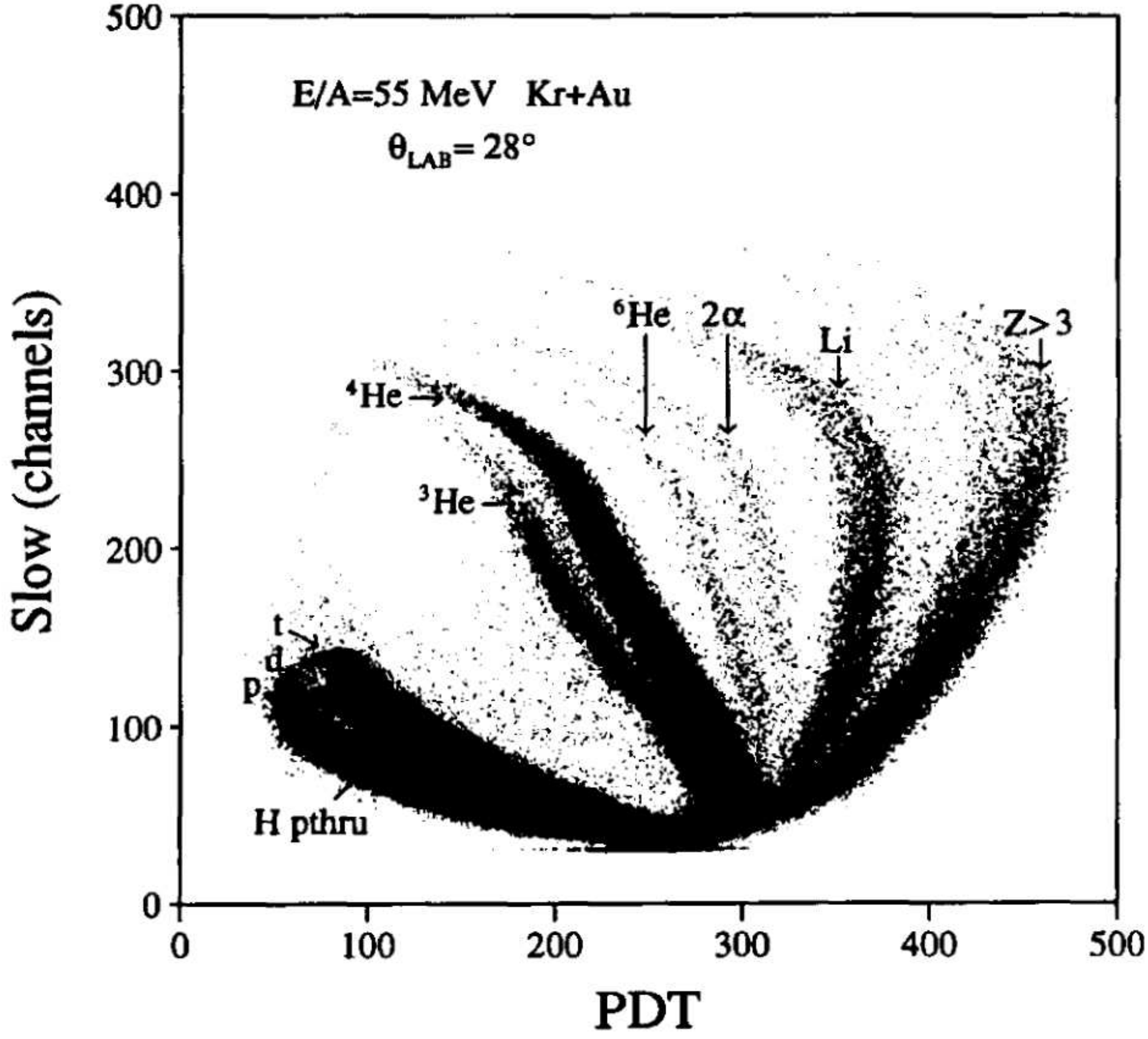

Figure 3.9. "Slow" versus PDT spectrum measured in ring 3′ ($\theta_{lab} = 28$ °) in the reaction ^{84}Kr + ^{197}Au at E/A = 55 MeV. See text for a discussion of the PDT function.

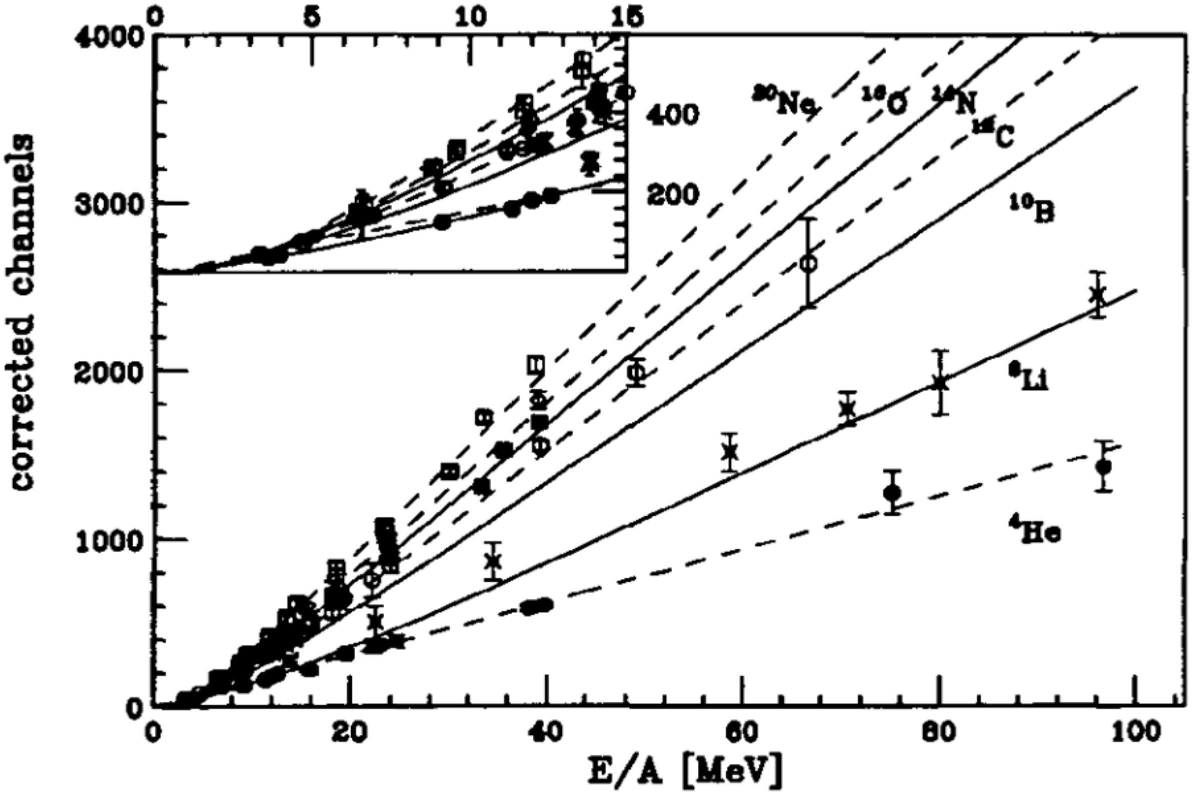

Figure 3.10. Calibration data for ^{4}He (solid circles), ^{6}Li (open fancy crosses), ^{10}B (crosses), ^{12}C (open circles), ^{14}N (solid squares), ^{16}O (open diamonds), and ^{20}Ne (open squares) [5]. The lines are fits with the form given by Eq. 6 (solid lines for odd charge elements and dashed lines for even charge elements).

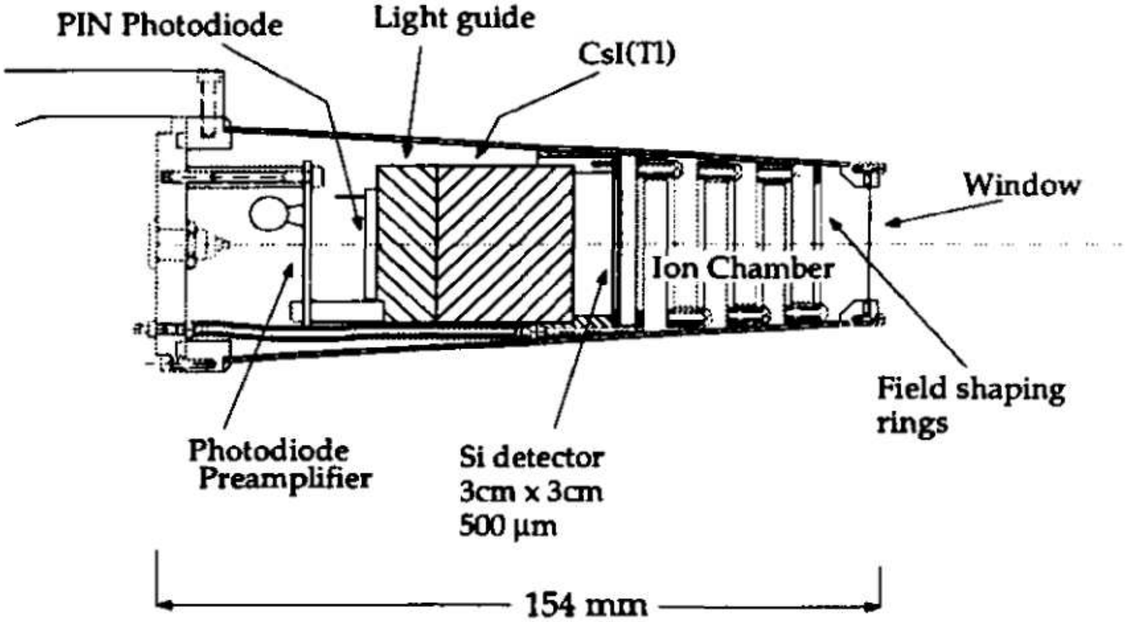
PIN Photodiode
Light guide
CsI(Tl)
Window
Ion Chamber
Field shaping rings
Photodiode Preamplifier
Si detector
3cm x 3cm
500 µm
154 mm

Figure 3.11. Cross-sectional view of an ion-chamber telescope (from Ref. [3]).

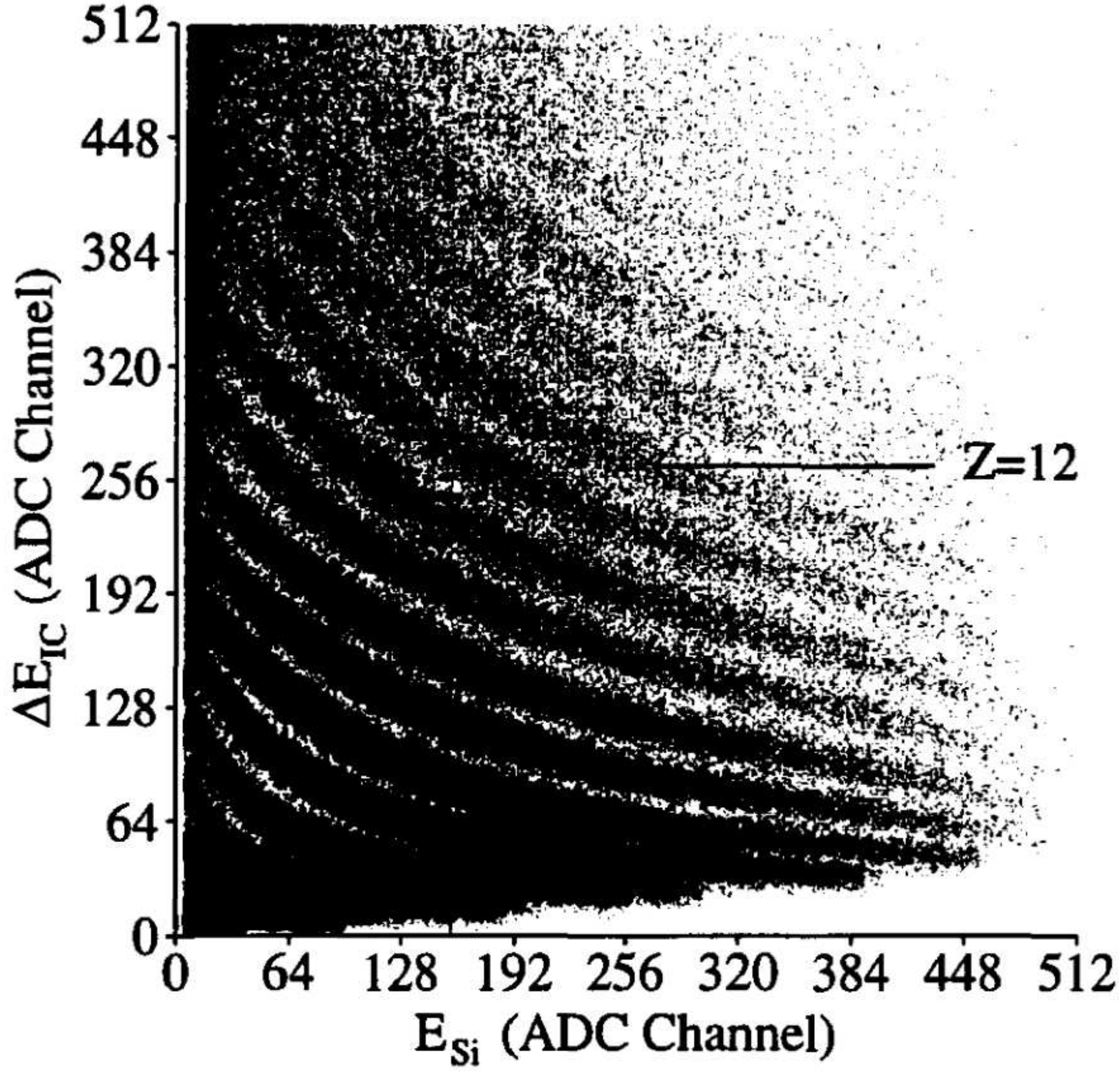

Figure 3.12. Two-dimensional plot of energy deposited in ion chamber versus energy deposited in Si(IP) detector (from Ref. [3]).

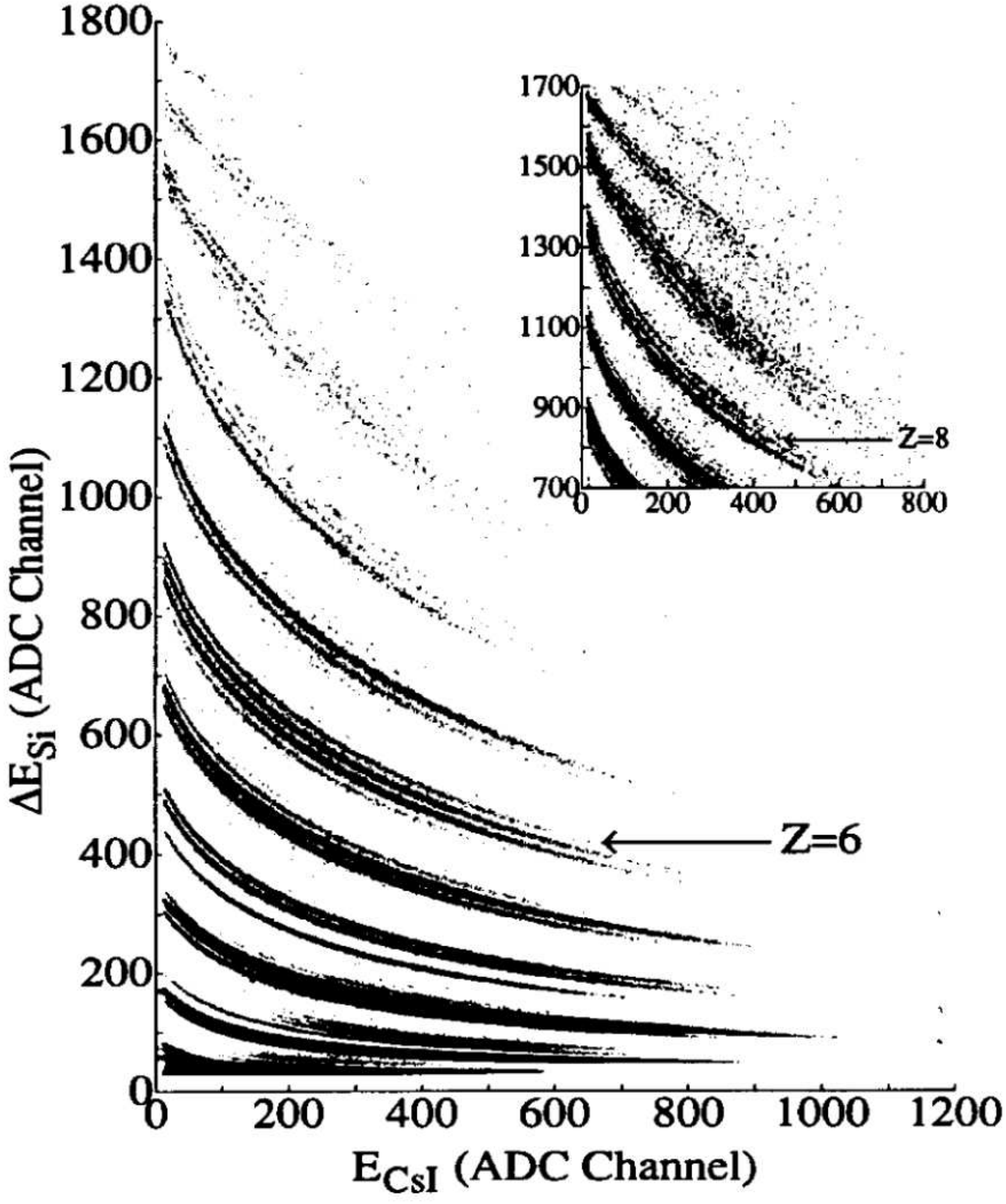

Figure 3.13. Two-dimensional plot of energy deposited in Si(IP) detector versus energy deposited in CsI(Tl) crystal (from Ref. [3]).

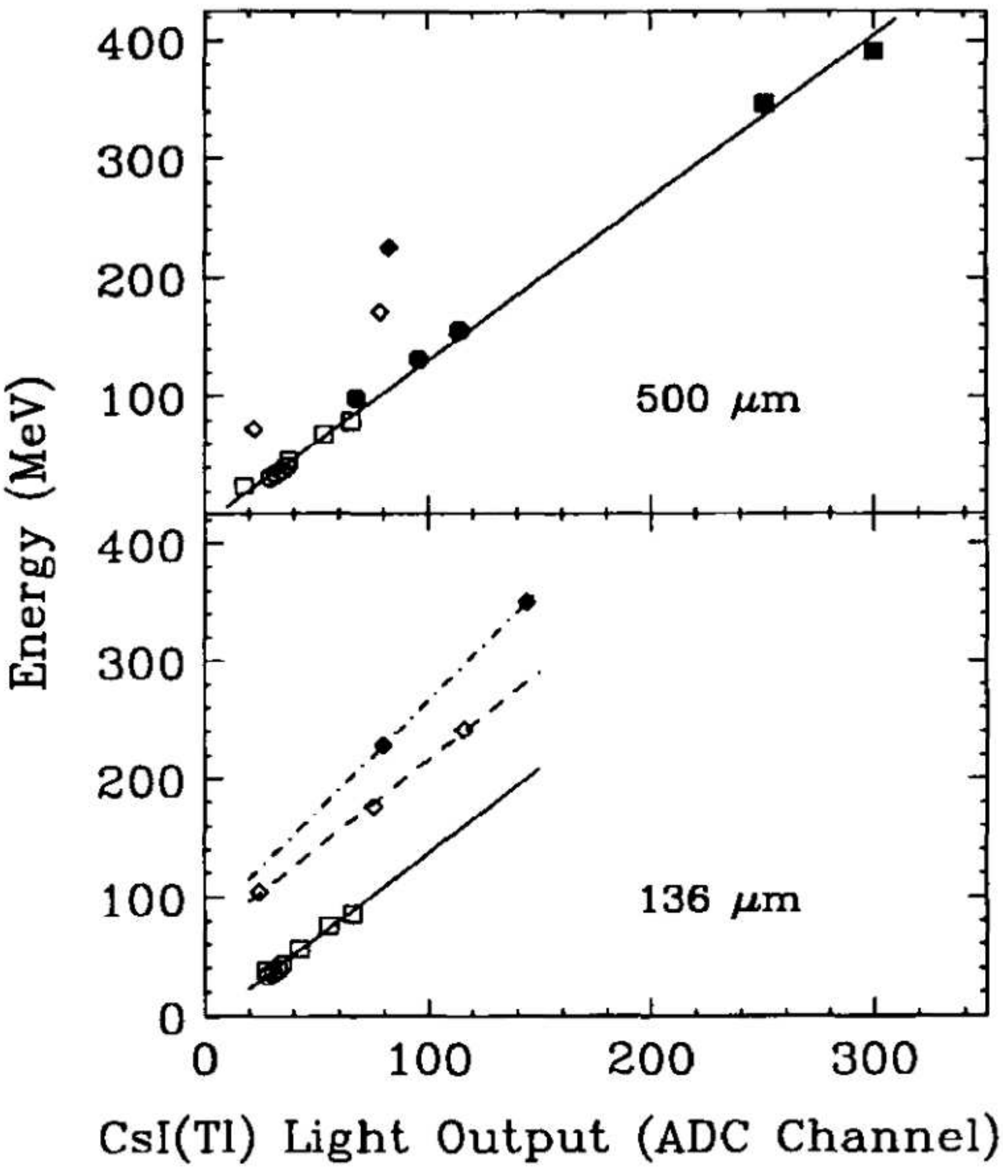

Figure 3.14. Dependence of light output on deposited energy for various particles (from Ref. [3]): p,d, and t isotopes (closed circles) and ^{3,4}He nuclei (closed squares) which punch through the CsI(Tl) crystal, deuteron (open circles) and α (open squares) beams of 22 MeV/u, 16 MeV/u, and 12 MeV/u which pass through the Si(IP) detector, and ^{12}C (open diamonds) and ^{16}O (closed diamonds) beams of 22 MeV/u and 17 MeV/u (top panel) and 22, 17, and 12 MeV/u (bottom panel).

CHAPTER 4

FRAGMENT EMISSION IN THE REACTION ^{84}KR + ^{197}AU AT E/A = 35 - 70 MEV

In intermediate-energy nuclear reaction studies, the emitted particles serve as probes of the highly excited system. The total number of detected charged particles reflect the violence of the collision [1,2]. The emission pattern of the particles and features of their kinetic energy spectra can be used to deduce the characteristics of the decaying source, such as its excitation energy and density [3–5]. In this chapter, various observables measured in the reaction ^{84}Kr + ^{197}Au at E/A = 35, 55, and 70 MeV are examined in order to characterize the sources of fragment emission in these collisions. Characteristics of the kinetic energy spectra and the IMF multiplicity distributions are compared to those measured for several systems over a large range in bombarding energy to investigate the systematics of multifragmentation.

A. General Reaction Characteristics

1. Multiplicity Distributions

The charged-particle multiplicity, N_c, can be used as a rough scale for the excitation energy of a highly excited nuclear system [1]. Assuming that the charged-particle multiplicity is strongly correlated with energy deposition, events with the largest number of charged particles are associated with the systems of highest excitation. The charged-particle multiplicity distributions for the reaction ^{84}Kr + ^{197}Au at E/A = 35, 55, and 70 MeV are shown in Figure 4.1. The distributions are characterized by a relatively featureless plateau and a near-exponential falloff at the highest multiplicities. In this high multiplicity tail, the correlation between N_c and excitation energy becomes dominated by fluctuations of the charged-particle multiplicity and this excitation energy scale breaks down at the highest values of N_c. The distributions for the Kr system are similar to those measured in the reactions ^{14}N + ^{197}Au at E/A = 100, 130, and 156 MeV [6] and ^{36}Ar + ^{197}Au at E/A = 50, 80 and 110 MeV [1], also shown in Figure 4.1. The maximum multiplicity observed in each reaction increases with increasing available center-of-mass energy from $N_c \approx 15$ for ^{14}N + ^{197}Au at E/A = 100 (available energy: 1307 MeV) to $N_c \approx 40$ for ^{84}Kr + ^{197}Au at E/A = 70 (available energy: 4122 MeV).

The charged-particle multiplicity can be used to construct a reduced-impact parameter scale by following a geometrical prescription [7]. In this geometrical picture, decreasing impact parameter corresponds to increasing overlap between the target and projectile and therefore an increasing amount of internal energy deposition. A correlation between charged-particle multiplicity and internal energy is assumed in order to relate N_c to the impact parameter [8]. The reduced-impact parameter, $\hat{b}$, is defined in terms of the probability for detecting N_c charged particles, $P(N_c)$:

$$\hat{b} = \frac{b}{b_{max}} = \left[\int_{N_c(b)}^{\infty} dN_c P(N_c) \right]^{1/2}, \tag{1}$$

where b_{max} is the maximum interaction radius, defined at $N_c = 2$. The value of the reduced-impact parameter is equal to 1 for the most peripheral interactions and 0 for the most central interactions. This scale is used to select on central collisions ($\hat{b} \leq 0.2$) which result in systems of the highest excitation. The minimum N_c corresponding to central collisions is depicted as arrows in Figure 4.1.

The dependence of the mean IMF multiplicity on the charged-particle multiplicity is shown for the ^{14}N, ^{36}Ar, and ^{84}Kr systems in Figure 4.2. For the ^{14}N reactions, the average IMF multiplicity is close to 1 for the highest values of N_c. Multifragmentation does not describe the average behavior of the systems formed in the ^{14}N + ^{197}Au reactions. As the bombarding energy is increased from E/A = 50 to 110 MeV, the ^{36}Ar + ^{197}Au reactions produce systems in the multifragmentation regime, i.e., on average more than two IMFs are emitted. The Kr-induced reactions produce the highest average fragment multiplicities, as many as 6 at E/A = 70 MeV. Whether these high fragment multiplicities are due to increased thermal energy of the system or compressional effects, which become increasingly important for heavier projectiles, is an important question that is currently being addressed.

2. Z_{sum} Distributions

An important question concerning the multifragment decay of these systems is whether or not a single heavy residue survives. The size of the residue is related to the violence of the collision; more violent collisions are expected to result in a smaller residue. A quantity that is useful for investigating the possible existence of a residue is the total detected charge, Z_{sum}. The correlation between Z_{sum} and the charged-particle multiplicity for ^{84}Kr + ^{197}Au at E/A = 35 and 70 MeV is presented in Figure 4.3. The shades of grey represent different levels of relative probability on a logarithmic scale. The most probable value of Z_{sum} increases monotonically with increasing charged-particle multiplicity (decreasing impact parameter). In Figure 4.4, the probability distributions, $P(Z_{sum})$ for different intervals in N_c are shown for E/A = 55. The distribution for central collisions is essentially a broad Gaussian spanning a large range in Z_{sum}. For some of the events the total charge of the system (115) is detected.

The first and second moments of the $P(Z_{sum})$ distribution are displayed in Figure 4.5. The mean value of Z_{sum} increases monotonically for all three energies with increasing multiplicity, reaching a maximum value of ≈ 80 at E/A = 35 MeV and ≈ 100 at E/A = 70 MeV. When corrected for the geometric efficiency of the detector array (0.90), these values correspond to ≈ 77% and 97% of the total charge of the system for E/A = 35 and 70 MeV, respectively. For the most central collisions, the values of Z_{sum} suggest that only a small residue survives for the collisions at E/A = 35 MeV and that essentially no residue remains at the highest bombarding energy. As the charged-particle multiplicity increases, the second moment of the $P(Z_{sum})$ distribution increases up to maximum value then saturates; this value corresponds to ≈ 11 and 10 at E/A = 35 and 70, respectively. This saturation in the second moment could be due to the upper limit of $Z_{sum} = 115$ (total charge of the system) which constrains the width of the $P(Z_{sum})$ distribution at high N_c.

3. Atomic Number Distributions

The atomic number (Z) distributions measured in the reaction ^{84}Kr + ^{197}Au at E/A = 55 MeV are depicted in Figure 4.6. The distributions represented by the solid points in the figure were measured using the low threshold ion-chamber telescopes. The yield for Z=4 is suppressed because ^{8}Be is unstable and decays into two alpha particles. The yield for Z=6 is enhanced due to the stability of ^{12}C. The solid lines in Figure 4.6 represent the same Z distributions with the Miniball energy thresholds applied. The energy thresholds for particle identification were $E_{th}/A = 0.8$ for the ion-chamber telescopes compared to $E_{th}/A \approx$ 2-4 MeV for Z=3-10 in the Miniball detectors. The effect of the higher thresholds is small at the most forward angles; however, at backward angles the difference is more pronounced, particularly for particles with large atomic number. The dashed line is the original distribution using energy thresholds equal to twice that of the Miniball detectors, shown to demonstrate further the dramatic effect of detector thresholds on measuring fragment distributions.

The detailed shape of the Z distribution is important in characterizing multifragmentation. In early studies of multifragmentation, measurements demonstrated that the Z distributions followed a power law: $P(Z) \propto Z^{-\tau}$ [9]. The values of the parameter τ extracted from fits to the Z distributions were ≈ 2.6, similar to values predicted for a liquid-gas system near its critical point. This observation was interpreted as evidence that multifragmenting systems exhibit critical behavior. More recently, the Z-distributions measured in heavy-ion reactions have been compared to the predictions of other theories that describe critical phenomena, such as 3-D percolation and the liquid-gas mean-field limit [10]. These comparisons are sensitive to the moments of the Z distributions.

The effect of the detector energy thresholds on the shape of the measured Z-distributions can be investigated quantitatively by performing power-law fits. Representative fits with the form $P(Z) \propto Z^{-\tau}$ are plotted for $E/A = 35$ (panel (a)) and 70 MeV (panel (b)) in Figure 4.7. The Z distributions measured in the ion-chamber telescopes and the Miniball detectors are represented by solid and open circles, respectively. The distribution measured in the Miniball has been re-normalized so that the cross section at Z=3 is equal to the cross section measured in the ion-chamber telescopes. At the forward angle ($\theta_{lab} = 35.5°$), the Z distributions are very similar, resulting in comparable values of τ. At the backward angle ($\theta_{lab} = 110°$), the Z distribution is steeper than that measured in the ion-chamber telescopes because of the higher threshold. Consequently, the value of τ obtained when fitting the Miniball distribution is larger than that obtained when fitting the ion chamber distribution. In fact, the distributions measured in the Miniball at backward angles are better described by an exponential (the open circles in panel (b) of Figure 4.7 essentially follow a straight line in dP/dZ versus Z).

The τ parameters extracted at each angle for the ion-chamber telescopes and Miniball detectors are plotted in Figure 4.8. Fragments emitted near $\theta_{lab} = 90°$ are strongly affected by energy loss in the target, resulting in an artificial suppression of higher Zs. The results from that region are therefore excluded. The value of τ obtained by fitting the angle-integrated ($25° \leq \theta_{lab} \leq 160°$) Z-distributions are indicated by solid and dashed lines for the ion-chamber telescopes and Miniball detectors, respectively. The values of τ are similar for distributions measured in each type of detector at the forward angles. At backward angles, the values extracted from the ion chamber measurements are fairly constant; τ increases slightly from ≈ 1.4 to 2. For the Miniball measurements, τ increases to values between 4 and 5 as the polar angle is increased to $\theta_{lab} = 150°$. Similar results are obtained at E/A = 70 MeV (bottom panel of Figure 4.8). These comparisons demonstrate that detector thresholds must be taken into account when interpreting features of the Z distributions, in particular the τ parameter from power-law fits.

B. Fragment Energy Spectra

1. Ion-Chamber Telescope Energy Spectra

In order to study the low energy fragments produced in the ^{84}Kr + ^{197}Au collisions, one detector in each ring of the Miniball with polar angle $\theta_{lab} \geq 25°$ was replaced with a low threshold ion-chamber telescope. Low energy thresholds are essential if one wants to measure the low energy portion of the spectrum near the "Coulomb peak". Features in this region of the spectrum reflect characteristics of the decaying source, most importantly the size and density of the system at the time of emission [11]. The low thresholds are also important when measuring energy spectra of high Z particles at backward angles, due to the forward momentum of the system. In this section, we focus on the fragment energy spectra measured in the ion-chamber telescopes and how the features of these spectra are related to characteristics of the emitting source.

Charged-particle multiplicity distributions measured in the Miniball and Miniwall with different trigger conditions are shown in Figure 4.9. The peripheral interactions are suppressed for the distribution triggered on a "hit" (detected-charged particle) in the ion-chamber telescopes (shown in panel (b)) as compared to the distribution triggered on two or more hits in the Miniball/Miniwall (panel (a)). This result can be understood as follows: the emitting system has a velocity component along the beam direction due to the momentum transfer from the projectile. The angular distributions are consequently forward-focused in the laboratory. The ion-chamber telescopes measured the cross section from $\theta_{lab} = 25° - 160°$. The minimum polar angle of $\theta = 25°$ for detection in the ion-chamber telescopes preferentially selects more central collisions since only the more violent collisions result in particles with sufficient energy to be emitted at polar angles $\theta_{lab} \geq 25°$. Requiring the detection of an IMF in the ion-chamber telescopes (panel (c)) further suppresses peripheral collisions because peripheral collisions have insufficient excitation energy to emit a fragment to $\theta_{lab} \geq 25°$.

Fragment kinetic energy spectra associated with central and midcentral collisions are shown in Figures 4.10-4.15. An impact parameter range of $\hat{b}$ = 0-0.4, corresponding to events with $N_c \geq 21$, 29, and 33 for collisions at E/A = 35, 55, and 70 MeV respectively, was used to select these events. Central and midcentral events were chosen in order to minimize the effects of angular momentum present in peripheral interactions and preferentially select events of the highest excitation. The kinetic energy spectra measured for lithium fragments emitted in the reaction ^{84}Kr + ^{197}Au at E/A = 35 MeV are presented in Figure 4.10. The spectra measured at each angle can be approximately described by a Maxwell-Boltzmann distribution characterized by a single temperature. The high energy tails of the spectra at backward angles have a steeper slope than at forward angles. This difference in slopes might be due to non-equilibrium emission, which is strongly forward-peaked in the laboratory. The Coulomb peak is well defined over the entire angular range.

Carbon energy spectra emitted in the same reaction are shown in Figure 4.11. The gap in the energy spectrum (from ≈ 140 - 200 MeV) for the ion-chamber telescope located at $\theta_{lab} = 35.5°$ is caused by incomplete biasing of the detectors. This results in a larger effective dead layer in the "back" of the Si detector. The effect is more pronounced for larger atomic number; high energy particles are relatively unaffected by this dead layer. At the backward angles, the Coulomb peak of the carbon energy spectra at low energy becomes broad. At $\theta_{lab} = 150°$, no peak is evident. Features similar to those observed for E/A = 35 MeV are also present in the lithium and carbon energy spectra at E/A = 55 and 70 MeV, shown in Figures 4.12-4.15. The spectra at forward angles become "harder" (less steep) with increasing bombarding energy. Systematic changes in features of the energy spectra, such as the Coulomb peaks and slope parameters, with increasing Z and beam energy will be discussed in greater detail in Section C.

2. Comparisons With Independent Calibrations

In Figure 4.16, lithium energy spectra measured in the ion-chamber telescopes ($b/b_{max} \leq 0.4$) are compared to lithium energy spectra measured in the Miniball detectors ($b/b_{max} \leq 0.2$) in the reaction ^{84}Kr + ^{197}Au at E/A = 55 MeV. The two independent measurements are in very good agreement below 200 MeV at forward angles. Above 200 MeV, the slope of the high energy tails in the spectra measured in the Miniball detectors is less steep than in the spectra measured with the ion-chamber telescopes. For carbon fragments, shown in Figure 4.17 for the same bombarding energy, the spectra measured in the ion-chamber telescopes and the Miniball detectors agree over the entire energy range at $\theta_{lab} = 35.5°$. At angles $\theta_{lab} \geq 35.5°$, the high energy tails measured in the Miniball detectors are less steep than the high energy tails measured in the ion-chamber telescope.

At the backward angles, the fragments do not punch through the Si detector. The Si energy calibrations are more accurate than the Miniball calibrations (1-2% for the Si versus 15% for the Miniball). The fact that the disagreement between the high energy tails is present also at backward angles suggests that the Miniball calibrations are the main source of the discrepancy. Because of the higher energy thresholds in the Miniball detectors, the Coulomb peak is not measured for lithium fragments detected at backward angles. For the carbon fragments, only a small portion of the energy spectrum is measured in the Miniball detectors at backward angles (see Figure 4.17).

Double differential cross sections for fragments emitted in the reaction ^{84}Kr + ^{197}Au at E/A = 35 MeV have been measured by Milkau *et al.* [12]. In Figure 4.18, inclusive lithium energy spectra measured at θ_{lab} = 40°, 55°, and 70° in that experiment are compared with the thesis measurement in the ion-chamber telescopes at

θ_{lab} = 45°, 57.5°, and 72.5°, respectively. The Milkau measurement used telescopes consisting of triple Si surface barrier detectors (25 μm, 300 μm, and 1000 μm) followed by an E detector. The E detector was a 2 cm bismuth germanate scintillator read out by photodiode at θ_{lab} = 40° and 55° and a Si(Li) detector with a thickness of 5000 μm at θ_{lab} = 70°.

As can be seen in Figure 4.18, there is good agreement between the two measurements. The spectra have not been re-normalized; the cross sections agree well over the entire range of energies at the three angles. The lithium spectrum measured by Milkau *et al.* at θ_{lab} = 40° has a slightly larger cross section in the region ≈140 MeV. This feature could be attributed to the difference in angle of measurement θ_{lab} = 40° for Milkau *et al.* compared to 45° for the ion-chamber telescopes. The energy spectrum measured at θ_{lab} = 35.5° in the ion-chamber telescopes is displayed as a solid line in panel (a) of Figure 4.18. The cross section measured by Milkau *et al.* is closer to the θ_{lab} = 35.5° measurement at E ≈140 MeV, but is closer to the measurement at θ_{lab} = 45° for $E \geq 175$ MeV. The feature near E ≈ 140 MeV in the Milkau spectrum might also be due to the dead layer between the second and third ΔE Si detectors. The punchthrough energies for these detectors are displayed as arrows in panel (c) of fig. 18. The agreement between the two independent measurements is also good for carbon fragments (fig. 19). The high energy tail for the carbon spectrum measured at θ_{lab} = 40° (open circles in Panel (a) of Figure 4.19) is intermediate between the measurements of θ_{lab} = 35.5° and 45 ° in the ion-chamber telescopes (closed circles).

The energy spectra measured in the ion-chamber telescopes agree well with the energy spectra measured by Milkau *et al.* over the entire energy range. The detector telescopes used by Milkau *et al.* consisted of surface barrier detectors which can be calibrated with accuracies of a few percent [12]. Based on this agreement between the ion chamber measurements and Milkau's measurements, the discrepancy between the high energy tails measured in the ion-chamber telescopes and the Miniball detectors can be attributed to the 15% uncertainty in the Miniball energy calibrations.

C. Moving-Source Fits

1. Backward-Angle Spectra

The fragment kinetic energy spectra have been analyzed using moving-source fits [3,4,13–15] to determine the systematic changes in spectral features with increasing Z and bombarding energy. Two questions we have focused on in this analysis are: 1) Are the fragments emitted primarily from a single equilibrated source and 2) are the slopes of the energy spectra an indicator of the temperature of the emitting system? The answer to these questions is complicated by the presence of multiple sources in the ^{84}Kr + ^{197}Au collisions at E/A = 35-70 MeV. According to the fireball model [16], at higher energies (> 100 MeV) the different sources are better defined. A portion of the projectile overlaps with the target, resulting in a hot zone, (a "fireball"), that completely decouples from the remaining projectile-like and target-like fragments. At the intermediate energies studied in this thesis, the sources are not as well defined. In order to differentiate among the contributions from the different sources, an analysis assuming multiple moving sources has been performed.

In light-ion reactions, the cross section measured at the backward angles in intermediate energy reactions has been shown to be consistent with emission from the target-like fragment (TLF) or "equilibrium" source [4,14]. The fragment energy spectra measured at backward angles for central and midcentral collisions ($b/b_{max} \leq 0.4$) in the reaction ^{84}Kr + ^{197}Au at E/A = 35, 55, and 70 MeV are displayed in Figure 4.20. For a given atomic number, the slopes of the high energy tails decrease with increasing beam energy. For a given bombarding energy, as the atomic number is increased, the Coulomb peak becomes broad. The disappearance of the Coulomb peak has been attributed to emission from a source of lower density [11]. If the TLF undergoes an expansion in response to thermal pressure [1,17], fragments emitted late in the de-excitation process will experience a reduced Coulomb repulsion as compared to fragments emitted earlier in the de-excitation. The backward-angle energy spectra appear to be consistent with a scenario where the higher Z's are emitted later than the lighter fragments. A clusterization of nucleons may be occurring prior to fragment emission. In that case, one would expect the heavier fragments to be emitted later than the lighter ones due to the longer time needed for clusterization.

The backward-angle fragment spectra (θ_{lab} = 110°, 130°, and 150°) have been parameterized using the following form:

$$\frac{d^2\sigma}{dEd\Omega} = \frac{N}{T^{3/2}}(E - V_C)^{1/2} exp[-(E - V_C)/T], \tag{2}$$

which describes the energy distribution for particles emitted in the rest frame of the decaying source [18]. In this equation, the particles are emitted from the volume as opposed to the surface of the emitting source. The parameter N is the normalization constant, T is the slope parameter, and V_C is the minimum Coulomb barrier for the particle. The distribution is transformed to the laboratory frame using

$$\left[\frac{d^2\sigma}{dEd\Omega}\right]_{lab} = \left[\frac{1-(v/c)^2}{A}\right]^{1/2} \left[\frac{d^2\sigma}{dEd\Omega}\right]_{E=E'}, \tag{3}$$

where

$$A = 1 - 2\rho cos\theta_{lab} + \rho^2 - (v/c)^2 sin^2\theta_{lab}, \tag{4}$$

v is the source velocity, and $\rho = v/v_{lab}$ [19]. The relationship between the particle's velocity in the rest frame, v′, and the laboratory, v_{lab}, is given by

$$v'^2 = \frac{[v_{lab}^2 + v^2 - 2vv_{lab}cos\theta_{lab} - (v/c)^2 v_{lab}^2 sin^2\theta_{lab}]}{[1 - (vv_{lab}/c^2)cos\theta_{lab}]^2}. \tag{5}$$

Single-source fits to the lithium and carbon energy spectra measured at backward angles in the reaction ^{84}Kr + ^{197}Au at E/A = 55 MeV are displayed in Figure 4.21. In the top panels, all four fitting parameters (N, T, V_C, and v) were allowed to vary and the best values were determined by minimizing the χ^2 per degree of freedom. The best values of the parameters for fragments of Z = 3 - 7 emitted in the reactions at 35, 55, and 70 MeV are listed in Table I. The fits are most sensitive to the cross-section measured at $\theta_{lab} = 110°$. This can be seen in the fits to the lithium spectra, where the high energy tails of the spectra measured at $\theta_{lab} = 130°$ and 150° are steeper than the slope predicted by the fit. This fact is further demonstrated in the lower panels of Figure 4.21, where the slope parameter is fixed at the indicated values. The change in spectral shape as the value of the slope parameter is increased is more pronounced at $\theta_{lab} = 110°$ than at the other two angles. This effect is presumably due to the larger cross-section measured at $\theta_{lab} = 110°$ which gives this angle a larger weighting in the fit.

The fragment kinetic energy spectra consist of a convolution of emissions occurring over a range in times as the source de-excites [21]. In this scenario, the temperature of the source ranges from the highest values at the beginning of the emission process down to the lowest values at the end. Consequently, the asymptotic logarithmic slopes, or slope parameters, from the moving-source fits to the backward angles should not be interpreted as the temperature of the TLF. Nonetheless, the high energy portion of the spectrum is dominated by emission from systems of highest excitation, and the slope parameter might reveal information about the initial excitation of the system [21,20,22].

The dependence of the slope parameter for the TLF source , T_{TLF}, on the Z of the fragment is plotted for the three bombarding energies in Figure 4.22. At a given bombarding energy, T_{TLF} increases with increasing Z, then saturates for the largest Zs. This suggests that the heavier IMFs are emitted from systems of higher temperature, or equivalently, higher excitation. For a given Z, T_{TLF} increases with increasing bombarding energy. The available center-of-mass energy, assuming full linear momentum transfer, increases from 2061 MeV at E/A = 35 MeV to 4122 MeV at E/A = 70 MeV. The excitation energy of the system is expected to increase with increasing available energy. The dependence of the slope parameter on bombarding energy in Figure 4.22 is consistent with sources of higher excitation at the higher bombarding energies.

2. Two-source Fits

The fragment energy spectra measured in the ion-chamber telescopes over the angular range $\theta_{lab} = 31°$ to $160°$ have been fit with two sources, each of the form given in Eqs. (2)-(5). The parameters for the TLF source are fixed to the values obtained from the single-source fits to the backward-angle energy spectra. As representative of fits to the IMF energy spectra, the fits to beryllium fragments emitted in the reaction ^{84}Kr + ^{197}Au at E/A = 55 MeV are displayed in Figure 4.23. The contribution attributed to the TLF source is depicted as dashed lines in that figure. The second component, corresponding to emission from a source at intermediate rapidity (IRS), is depicted as dot-dashed lines. The physical origin of the IRS, or non-equilibrium, source is not completely understood. Although it has been proposed that non-equilibrium fragments originate from damped collisions [23], non-equilibrium emission has also been observed in light-ion reactions [24]. Also, the energy, angular, and Z-distributions of non-equilibrium IMFs are consistent with a distinct mechanism, where the memory of all projectile properties is destroyed by multiple nucleon-nucleon collisions [15]. The solid line is the sum of the two sources. The cross-section at each angle is reasonably described by the two sources.

Selecting on central and midcentral collisions suppresses the contribution from the projectile-like source at intermediate angles ($25° \leq \theta_{lab} \leq 100$ °). However, the cross-section measured at $\theta_{lab} = 25°$ shows some contamination of emission from the projectile-like source and is therefore not included in the fits. The detector located at $\theta_{lab} = 90°$ is also not included, since the spectra in this detector are strongly affected by energy loss in the target. The IRS parameters from fits to fragments of Z = 3 - 7 emitted in the reactions at E/A = 35, 55, and 70 MeV are listed in Table I. The slope parameter of the IRS source increases steadily with increasing bombarding energy but does not have a strong dependence on Z. The Coulomb parameters, V_C, are similar to those obtained in fits to the backward-angle spectra. The Coulomb parameters should not be interpreted as a Coulomb barrier, particularly at the higher Zs where the Coulomb peak becomes less distinct. A single Coulomb parameter cannot describe the low energy portion of the energy spectrum, i.e., emission near the barrier. The actual barrier is not well defined due to fluctuations in the charge distribution of the source and sub-barrier emission. The source velocities of the IRS source are equal to nearly half the beam velocity at each energy and are 2-3 times larger than the TLF source velocities. The source velocities do not show a strong dependence upon the Z of the fragment.

Moving-source fits to inclusive light-charged-particle spectra emitted in similar systems over the bombarding energy range E/A = 9-800 MeV/A reveal a steady increase in the IRS slope parameter with incident energy [3]. An increase in slope parameter for the IRS source with bombarding energy was also observed by Jacak *et al.* in inclusive measurements of E/A = 42-151 MeV Ar- and Ne-induced reactions on Al, Ca, and Au targets [25]. Wile *et al.* have demonstrated that the slope parameters extracted for the non-equilibrium source are sensitive to energy thresholds, angular coverage, and assumptions about emission from the equilibrium source. They found the slope parameter for the non-equilibrium source to be constant over the bombarding energy range E/A = 30-100 MeV in collisions of ^{14}N ions with ^{nat}Ag and ^{197}Au targets and they attributed Jacak's results to the effects of a limited angular acceptance and high detector thresholds [15].

The results from two-source fits to the ^{84}Kr + ^{197}Au system indicate that slope parameter of the IRS source increases steadily with increasing bombarding energy. However, the spectra were constructed for central and midcentral collisions ($\hat{b} \leq 0.4$). Selecting on this range in impact parameter removes the non-equilibrium component associated with peripheral collisions. Therefore, it is difficult to make direct comparisons to inclusive results.

D. Multifragmentation Systematics

1. Non-thermal Behavior in Multifragment Decay

To explore the systematics of multifragmentation, several systems have been studied over a large range of bombarding energies at the National Superconducting Cyclotron Laboratory. These systems include ^{14}N+^{197}Au at E/A = 100-156 MeV [6], ^{36}Ar+^{197}Au at E/A = 35-110 MeV [1], ^{84}Kr+^{197}Au at E/A = 35-70 MeV [26], and ^{129}Xe+^{197}Au at E/A = 40-60 MeV [27]. The ^{84}Kr+^{197}Au experiment is representative of the type of data taken for these reactions. In this section, the fragment energy spectra will be compared to determine the extent to which the excitation energy is equilibrated in these reactions. In order to select collisions resulting in a composite system with the highest excitation and the least angular momentum, events were selected with $b/b_{max} \leq 0.2$, using the reduced-impact parameter scale discussed previously.

The kinetic energy spectra for boron fragments emitted in central collisions of ^{84}Kr projectiles with ^{197}Au target nuclei at E/A = 55 MeV are shown in Figure 4.24(a). The more forward angles have a less steep exponential tail showing a non-negligible probability for preferential emission of high energy fragments at forward angles even for central collisions. To eliminate the trivial momentum of the composite system along the beam axis due to the momentum transfer from the projectile, one can construct the transverse kinetic energy, defined as $E_{trans} = Esin^2\theta$, where E and θ are the laboratory energy and emission angle, respectively. In the absence of collective effects [28–30], the transverse kinetic energy should represent a good measure of the thermalized energy available to the fragments. The transverse kinetic energy distributions constructed from these spectra are displayed in Figure 4.24(b). The high energy portion of these spectra can be characterized by a simple exponential.

As can be seen in Figure 4.24(b), the slope of this exponential changes very little as a function of angle. Note that the distribution at 57.5° dominates the tail of the distribution. General sequential statistical decay models predict that the high energy portion of the spectrum is populated by emission from systems of the highest excitation while the low energy portion of the spectrum is populated by emission during later stages of the de-excitation cascade from a less excited system [31,32]. The asymptotic logarithmic slopes of the transverse kinetic energy distributions therefore might provide information about the initial excitation of the composite system.

In Figure 4.25, the slope parameters for boron fragments produced in the different reactions are plotted versus the multiplicity associated with central collisions. The open circles represent the ^{14}N+^{197}Au system at E/A = 100, 130, and 156 MeV; solid squares depict ^{36}Ar+^{197}Au at E/A = 35, 50, 80, and 110 MeV; solid circles represent ^{84}Kr+^{197}Au at E/A = 35, 55, and 70 MeV/A ; the solid stars indicate the ^{129}Xe+^{197}Au system at E/A = 40 and 60 MeV. A linear trend is evident for all these systems, which span N_C from 15 to 38 and T (slope parameter) from 11 to 31.5 MeV. For the lightest projectiles studied, ^{14}N, the slope of $T(E_t)$ with respect to N_c is nearly flat, perhaps indicating a saturation of energy deposition for light heavy-ions ($A \leq 20$) by a nucleon-nucleon collision mechanism in this energy range. The magnitude of the measured slope parameter is also interesting. For the heaviest beams at the highest incident energies, the slope parameter reaches values greater than 30 MeV. Such large values of the slope parameter, far in excess of the binding energy of the system are too high to be attributed to a thermal temperature of the system.

If the multiplicity is proportional to the excitation energy of the system, and the slope parameter is proportional to the temperature of the system, then an increasing monotonic relationship between these two quantities is expected. A similar relationship between multiplicity and the deduced excitation of the system has recently been observed within a single system [33]. If a Fermi-gas model were appropriate and the level density were assumed to be constant, a quadratic relationship between these two variables would be expected. The reason for the lack of a quadratic relationship between the multiplicity and slope parameter might be the dependence of the level density on excitation energy and source volume. Essentially the same trend is observed for all IMFs in the range $3 \leq Z \leq 9$ as indicated by the error bars shown in Figure 4.25.

An additional consideration in the interpretation of the trend observed in Figure 4.25 is the emission of IMFs from multiple sources. The emission at backward angles ($\theta_{lab} \geq 90°$) can be characterized by a target-like residue while emission at forward and middle angles (($\theta_{lab} \leq 90°$) manifests a component attributable to emission from a source of intermediate rapidity. The importance of the intermediate rapidity source increases with increasing projectile mass. Moving-source fits of the kinetic energy spectra and angular distributions from the ^{84}Kr+^{197}Au system were performed to assess the contributions of the two sources (see Section C). The slope parameters for the target-like source of boron fragments from the ^{84}Kr+^{197}Au system are compared to slope parameters from the systems ^{14}N + ^{197}Au and ^{36}Ar + ^{197}Au in Figure 4.26. The slope parameters are plotted versus the multiplicity associated with central collisions. The ^{36}Ar results [34,35] were parameterized using the form

$$\frac{d^2\sigma}{dEd\Omega} = N(E_{lab} - V_C)^{1/2} exp[-(E/T)], \tag{6}$$

where

$$E = E_{lab} - V_C + E_0 - 2(E_0(E_{lab} - V_C)cos\theta_{lab})^{1/2}, \tag{7}$$

and $E_0 = (1/2)mv^2$. For comparison, the ^{14}N and ^{84}Kr data have also parameterized using Eqs. (6) and (7); the resulting slope parameters are 10-15% higher than those obtained using Eqs. (2)-(5). The slope parameter does not exceed 20 MeV for this source, suggesting that the slope parameter of the transverse kinetic energy distribution may be attributed to the non-equilibrium source.

More detailed simulations consisting of two isotropically-emitting sources (an equilibrium and a non-equilibrium source) show that the slope parameter of the transverse kinetic energy distribution is approximately equal to the apparent temperature of the non-equilibrium source. The physical origin of this large apparent temperature for IMF emission associated with central collisions is presently unclear however it is certainly too large (T = 30 MeV) to represent a thermal temperature. The large magnitude of the slope parameter for the heaviest projectiles at the highest incident energies studied could be due to the onset of collective effects. Experimental evidence for a collective expansion has been reported for several heavy-ion systems at intermediate energies [28–30]. For the ^{14}N systems where the collective expansion is expected to be small, the slope parameters of the transverse kinetic energy distributions are nearly equal to the slope parameter for the target-like source (T $\approx$ 10 MeV). For the heaviest projectiles at the highest bombarding energies where the collective effects are expected to be more important, the largest differences are observed between the transverse energy and TLF slope parameters.

2. Comparisons to the Predictions of the QMD Model

To explore the role of the collision dynamics in multifragment emission, simulations were performed using the QMD model [36]. Central collisions in the reactions ^{14}N + ^{197}Au at E/A = 156 MeV, ^{36}Ar + ^{197}Au at E/A = 80 MeV, and ^{84}Kr + ^{197}Au at E/A = 70 MeV were studied to see if the experimentally observed transverse kinetic energy distributions can be reproduced using a dynamical treatment.

The QMD approach is described in Chapter 2, Section A.1. A "soft" equation of state was selected for the effective interaction (K = 200 MeV). Each simulated event was calculated for 900 time steps of 0.2 fm each to a final time of 180 fm/c. At the final time step, the nucleons were clustered with the Minimum Spanning Tree algorithm [37]. Nucleons within 4 fm of each other were considered part of the same cluster. The effective charge of each cluster was assigned using the mass and the following parameterizations:

$$Z_{eff} = \frac{A + 1.1}{2.} \quad (A \leq 20) \tag{8}$$

and

$$Z_{eff} = \frac{A}{1.98 + 0.015 * A^{2/3}} \quad (A > 20), \tag{9}$$

where A is the mass of the cluster. The integer of the value of Z_{eff} was used for A $\leq$ 20 and the value was rounded for clusters with A > 20. After the clusters were defined, the final momenta of the particles were obtained using an n-body classical Coulomb trajectory calculation [38]. The simulations were filtered through the detector apparatus for comparison with the data.

A simulated central collision (b = 0.5 fm) in the reaction ^{84}Kr + ^{197}Au at E/A = 70 MeV is presented in Figure 4.27. The positions of the nucleons in the ^{84}Kr projectile (closed circles) and in the ^{197}Au target (open circles) are shown in the x-z plane in the center-of-mass system. At the beginning of the calculation (t = 0 fm), the ^{84}Kr and ^{197}Au nuclei are clearly separated. The two nuclei move towards each other with equal momenta in the center-of-mass system. At t = 60 fm/c, nucleons from the projectile emerge on the other side of the target. At later times, three regions become evident in the diagram: the projectile nucleons at large, positive z-values, a target-like residue near z=0 consisting mainly of target nucleons, and an intermediate zone with nearly equal numbers of target and projectile nucleons. At the final time step (t = 180 fm/c), the three regions are fairly well separated.

In Fig. 4.28, the intermediate-mass-fragment and total-charged-particle multiplicities are presented for simulated central collisions in the reaction ^{14}N + ^{197}Au at E/A = 156 MeV and ^{84}Kr + ^{197}Au at E/A = 70 MeV. An IMF was defined as a cluster with 3 $\leq$ Z $\leq$ 20, excluding A = 5. For the ^{14}N + ^{197}Au system, fragments begin to appear at t = 60 fm/c. At t = 80 fm/c, multiple fragments are formed in some events and the the mean value of the charged-particle multiplicity is nearly double that at t = 60 fm/c. The distributions change only gradually from t = 80 fm/c to the final time step of 180 fm/c. The value of $< N_{IMF} >$ at t = 180 fm/c is 0.16 and 0.15 before and after filtering, respectively. This value is quite low compared to the experimentally observed value of $< N_{IMF} > \approx 1.3$ for the ^{14}N + ^{197}Au system. In contrast to the ^{14}N + ^{197}Au system, the mean values of N_{IMF} and N_c observed in the ^{84}Kr + ^{197}Au simulation increase steadily from t = 80 fm/c to the final time step. The value of $< N_{IMF} >$ at t = 180 fm/c is 5.7 before filtering and 5.2 after filtering. The filtered value is in good agreement with the value of $< N_{IMF} > \approx 6$ observed in central collisions of the reaction ^{84}Kr + ^{197}Au at E/A = 70 MeV.

Atomic number distributions from the QMD simulations are presented in Figure 4.29. The final time step (t = 180 fm/c) is shown for central collisions in the reaction ^{14}N + ^{197}Au at E/A = 156 MeV (top panel) and ^{84}Kr + ^{197}Au at E/A = 70 MeV (bottom panel). As can be seen in Figure 4.29, two distinct classes of fragments are emitted from the ^{14}N + ^{197}Au system: the IMFs ($Z \leq 20$) and the remaining residue ($Z \approx$ 50-80). For the ^{84}Kr + ^{197}Au system, the residue has a broad distribution in Z_{eff} and the maximum has shifted to lower values; the two distinct classes of particles are no longer evident in the atomic number distribution.

The kinetic energy distributions produced in the QMD simulations show remarkable similarities to the experimentally observed distributions. Kinetic energy distributions for $Z_{eff} = 3$ fragments at selected angles are shown for the reaction ^{84}Kr + ^{197}Au in Figure 4.30. The spectra are shown before (top panel) and after (bottom panel) the n-body Coulomb trajectory calculation. As expected by the Coulomb acceleration, the peaks of the distributions are shifted to higher values after the n-body calculation. The spectra appear consistent with Boltzmann-like distributions at each angle, and the slope of the high energy tail increases from forward to backward angles.

The transverse kinetic energy spectra for $Z_{eff} = 4$ fragments for the three systems studied are compared in Figure 4.31. The distributions are simple exponentials before n-body Coulomb trajectory calculation is performed (top panel). The n-body calculation shifts the distribution to higher values of E_t (bottom panel); the slope of the high E_t tail is essentially the same. The spectra were filtered through the experimental device and the asymptotic logarithmic slopes of the E_t distributions were extracted. The resulting slope parameters for $Z_{eff} = 5$ fragments are compared with the experimental values for boron fragments in Figure 4.25. Although the values for the ^{14}N + ^{197}Au and ^{36}Ar + ^{197}Au systems are in reasonable agreement, the value for the ^{84}Kr + ^{197}Au system is 20% too low. This discrepancy may be related to the fact that the heat capacity is too large in the QMD model as compared to true fermionic systems [39]. The simulated charged-particle multiplicity is too high for the ^{84}Kr + ^{197}Au system: 43.3 compared to the experimental value of 39.8. The high heat capacity results in the retention of heat by the system and favors the evaporation of light charged particles as opposed to decay by the emission of fragments. The excess heat that is stored also reduces the amount of energy available for collective expansion of the system. Alternatively, the collective motion transverse to the beam could be too low in the simulation due to the fact that a "soft" equation-of-state is used for the effective interaction. Although a soft equation-of-state is needed to reproduce the IMF multiplicities, a "stiff" equation-of-state may be needed to reproduce the experimentally observed collective effects.

3. Evidence for the Reducibility of Multifragment Emission

Recent experimental evidence supports the theory that multiple fragment emission probabilities are reducible to an elementary binary probability, p, i.e., that multifragmentation is reducible to a combination of nearly independent emission processes [40,41,27]. In the following analysis, the reaction ^{84}Kr + ^{197}Au at E/A = 35-70 MeV is examined within this formalism to determine if similar results are obtained for systems where multiple sources are present and dynamical effects are expected to be important. The method is also applied to the reaction ^{14}N + ^{197}Au at E/A = 100-156

MeV where systems of modest excitation are formed [6].

The elementary probability, p, for a binary decay to occur at any given "try" is

$$p = \frac{\Gamma}{\hbar\omega_0} = e^{-B/T}, \tag{10}$$

where Γ is the partial decay width associated with a given binary channel, ω_0 is the characteristic frequency, B is the barrier, and T is the temperature. In this framework, the decaying system has the opportunity to try m times to emit an "inert" fragment with constant probability, p. The probability of emitting exactly n fragments is then given by a binomial distribution:

$$P_n^m = \frac{m!}{n!(m-n)!} p^n (1-p)^{m-n}. \tag{11}$$

and the average multiplicity and variance are

$$\langle n \rangle = mp \tag{12}$$

and

$$\sigma^2 = \langle n \rangle (1-p). \tag{13}$$

Values of p and m can thus be extracted from the mean and variance of the IMF multiplicity distributions at any excitation energy.

If the probability p has a thermal dependence, then a plot of log(1/p) vs 1/T (Arrhenius plot) should be linear, where T is the temperature of the source. In the context of the Fermi-gas model, the relationship between the source temperature, T, and excitation energy, E, is given by T ∝ $\sqrt{E}$ [42]. The observable E_t, the total transverse energy of all detected particles, is assumed to be proportional to the excitation energy of the source. A temperature scale can therefore be constructed using the above relationships: T ∝ $E_t^{-1/2}$. Plots of log(1/p) vs. $E_t^{-1/2}$ were found to be linear over the entire range of excitation energy for the systems ^{36}Ar + ^{197}Au at E/A = 80 and 110 MeV by Moretto *et al.* [40].

Arrhenius plots constructed for the system ^{84}Kr + ^{197}Au at E/A = 35, 55, and 70 MeV are shown in Figure 4.32. A threshold of $E > 0$ was imposed on the IMFs in constructing the IMF multiplicity distributions. The plots are linear over a very limited range in E_t; at the lowest and highest values of E_t, the value of $1/p$ saturates. The mean and variance of the N_{IMF} distributions, shown in Figure 4.33, have a smooth dependence on E_t. The value of m peaks at $E_t \approx 400$ MeV, decreases and then saturates at high E_t for the systems ^{84}Kr + ^{197}Au at E/A = 55 and 70 MeV. At E/A = 35 MeV, the value of m is nearly constant over the entire range of E_t.

One possible explanation for the saturations in the Arrhenius plot might be a breakdown in the assumption that E_t represents the excitation energy of the system. In particular, light charged particles that punch through the detectors would contribute to such a breakdown, since they are most likely pre-equilibrium and do not reflect the excitation of the excited residue. As can be seen in Figure 4.34, excluding the punchthroughs results in an Arrhenius plot that is straight for the reaction ^{84}Kr + ^{197}Au at E/A = 70 MeV (solid squares). In order to make a less device-dependent selection, all particles with longitudinal velocity, $v_z \geq 7$ cm/ns were additionally excluded.

The selection of this value for the longitudinal velocity is justified by examination of the longitudinal velocity distributions. The v_z distributions for alpha particles and boron fragments emitted in peripheral collisions ($b/b_{max} \geq 0.8$) of the reaction ^{84}Kr + ^{197}Au at E/A = 70 MeV are shown in the top and bottom panels, respectively, of Figure 4.35. The arrows in both panels indicate the cutoff value of $v_z = 7$ cm/ns. The peak at $v_z \approx 9$ cm/ns in both distributions is attributed to particles originating from non-equilibrium processes. Particles with a $v_z \leq 5$ cm/ns are attributed to emission from the equilibrium source. Particles with a longitudinal velocity higher than 7 cm/ns were excluded in the analysis. The high v_z cut has a much smaller effect on the Arrhenius plot than the initial constraint of excluding the punchthroughs. The resulting line, shown in Figure 4.36 as open diamonds, is fairly straight over essentially the entire range in E_t. The change in the line for the high v_z cut is due mainly to eliminating LCPs with high v_z: a cut in high v_z for only the light charged particles has the same effect on the slope of the line as a high v_z cut on all particles. After removing the punchthroughs and high v_z particles, the mean and variance exhibit a smoother dependence with E_t at all three energies (Figure 4.36). The subtle changes in the mean and variance produce dramatic effects in m: the peak in the value of m at low E_t is eliminated.

For the ^{36}Ar + ^{197}Au systems, eliminating the punchthroughs and high v_z particles changes the slope of the line in the Arrhenius plot. For these systems, punchthrough lithium fragments have also been excluded. If the punchthrough lithiums are included, the line curves "downward" at low E_t (toward higher probability). Eliminating the high v_z particles has a very small additional effect on the slope of the line. The effects of excluding punchthrough particles and eliminating particles with high v_z for the reaction ^{36}Ar + ^{197}Au at E/A = 110 MeV are shown in Figure 4.37. The mean and variance of the IMF distribution and the value of m as a function of E_t are shown for the ^{36}Ar + ^{197}Au systems in Figure 4.38. The punchthrough and v_z cuts eliminate the increase in m at low E_t observed by Moretto *et al.* [40] for the reaction at E/A = 110 MeV (Figure 4.38, panel c).

The ^{84}Kr + ^{197}Au and ^{36}Ar + ^{197}Au systems with cuts are compared in Figure 4.39. The lines for all bombarding energies converge at a value of $1/p \approx 2$ or $p \approx 0.5$. If the emission probability is described by Eq. (10), then a value of $p = 1$ corresponds to a disappearance of the barrier, B, or an extremely high temperature of the emitting system. The ^{36}Ar + ^{197}Au and ^{84}Kr + ^{197}Au appear to reach the same limit of $B/T \approx 0.7$ at high E_t. There is a smooth progression of increasing slope with increasing beam velocity (MeV/A). The increase in slope could be due to a change in the proportionality constant between E_t and E with increasing bombarding energy [40] or a change in the emission barrier. The trend observed in Figure 4.39 may be a progression from dynamically-driven multifragmentation to thermally-driven multifragmentation. Dynamical breakup is expected to be more important for the heaviest projectiles at the lowest bombarding energies. For the system ^{84}Kr + ^{197}Au at E/A = 35, the break-up might be due to dynamical effects, such as shape instabilities [43]. In this case the multifragmentation probability would not be strongly dependent on the excitation energy, resulting in a smaller slope of the Arrhenius plot. In contrast, dynamical breakup is not expected to be as important for the system ^{36}Ar + ^{197}Au at E/A = 110 MeV, which exhibits the strongest correlation between emission probability and excitation energy.

Arrhenius plots constructed for the reaction ^{14}N + ^{197}Au at E/A = 100, 130, and 156 MeV are displayed in Figure 4.40. The lines have a slight curvature toward higher 1/p values (lower probability) at E/A = 130 and 156 MeV and toward lower 1/p values (higher probability) at E/A = 100 MeV. Eliminating punchthrough and high v_v particles does not change the shape of the lines. The lines converge at high E_t at a value of $1/p \approx 8$, or $p \approx 0.125$. This probability is lower than the value of $p \approx 0.5$ and $p \approx 0.7$, where the lines converge for the ^{36}Ar + ^{197}Au and ^{84}Kr + ^{197}Au systems, respectively. The ^{14}N + ^{197}Au systems do not appear to be reaching the high-excitation-energy regime where the ^{36}Ar + ^{197}Au and ^{84}Kr + ^{197}Au converge at high E_t. The value of m extracted for the ^{14}N + ^{197}Au systems, plotted in panel c of Figure 4.41 (no cuts), reaches an asymptotic value of ≈ 10, similar to the value observed in the ^{36}Ar + ^{197}Au and ^{84}Kr + ^{197}Au systems with punchthrough and high v_z cuts. Eliminating punchthrough and high v_z particles does not suppress the increase in the value of m at low E_t for the ^{14}N + ^{197}Au reactions at E/A = 130 and 156 MeV. This deviation from a constant value of m at low E_t may reflect a different fragment production mechanism than is observed at higher values of E_t.

TABLES

Table 4.I. Table of parameters for two-source fits to the energy spectra of fragments emitted in the reaction ^{84}Kr + ^{197}Au at E/A = 35, 55, and 70 MeV. The Normalization constants, N_i are given in units of ($sr^{-1}MeV^{-2}$). The slope parameters, T_i, and Coulomb parameters, V_{C_i}, are in units of MeV. The source velocities are expressed as a fraction of the speed of light, c = 30.0 cm/ns.

E/A	Z	TLF				IRS			
		N_1	T_1	V_{C_1}	v_1/c	N_2	T_2	V_{C_2}	v_2/c
35	3	189.9	10.0	26.0	0.052	313.9	16.3	21.9	0.141
	4	69.0	11.6	26.5	0.047	99.6	15.4	31.1	0.126
	5	85.7	12.5	33.9	0.054	119.0	16.8	32.3	0.136
	6	73.9	13.4	36.0	0.052	123.7	17.7	35.4	0.131
	7	45.6	12.8	29.9	0.042	99.8	19.8	37.0	0.129
55	3	325.3	13.0	32.2	0.070	365.2	21.2	29.0	0.177
	4	113.3	13.5	28.1	0.058	166.2	22.2	27.1	0.149
	5	119.6	14.3	30.7	0.055	187.8	22.2	34.1	0.146
	6	96.3	15.3	38.9	0.057	171.4	22.1	38.0	0.141
	7	80.5	15.1	50.7	0.065	79.6	21.6	50.9	0.149
70	3	112.3	13.8	36.8	0.072	176.8	26.3	29.2	0.184
	4	43.9	15.5	28.5	0.058	72.1	27.1	28.8	0.159
	5	68.8	17.9	45.0	0.075	40.8	24.5	50.1	0.188
	6	51.6	18.5	44.5	0.066	42.6	24.8	51.2	0.167
	7	30.6	18.6	58.6	0.069	22.5	24.3	58.6	0.163

REFERENCES

[1] R.T. de Souza *et al.*, Phys. Lett. **B268**, 6 (1991).

[2] D.R. Bowman *et al.*, Phys. Rev. C **46**, 1834 (1992).

[3] G.D. Westfall *et al.*, Phys. Lett. **B116**, 118 (1982).

[4] M. Fatyga *et al.*, Phys. Rev. Lett. **58**, 2527 (1987).

[5] S.J. Yennello *et al.*, Phys. Rev. Lett. **67**, 671 (1991).

[6] Y. Lou *et al.*, Nucl. Phys. A, in press.

[7] C. Cavata *et al.*, Phys. Rev. C **42**, 1760 (1990).

[8] L. Phair *et al.*, Nucl. Phys. **A548**, 489 (1992).

[9] J.E. Finn *et al.*, Phys. Rev. Lett. **49**, 1321 (1982).

[10] M.L. Gilkes *et al.*, Phys. Rev. Lett. **73**, 1590 (1994).

[11] K. Kwiatkowski *et al.*, Phys. Rev. Lett. **74**, 3756 (1995).

[12] U. Milkau *et al.*, Z. Phys. **A346**, 227 (1993).

[13] M. Fatyga *et al.*, Phys. Lett. **B185**, 321 (1987).

[14] S.J. Yennello *et al.*, Phys. Rev. C **41**, 79 (1990).

[15] J.L. Wile *et al.*, Phys. Rev. C **45**, 2300 (1992).

[16] G.D. Westfall *et al.*, Phys. Rev. Lett. **37**, 1202 (1976).

[17] D. R. Bowman *et al.*, Phys. Rev. Lett. **67**, 1527 (1991).

[18] R. Wada *et al.*, Phys. Rev. C **39**, 497 (1989).

[19] Methods of Experimental Physics, Volume 5 Part B: Nuclear Physics, L. Marton, Academic Press, New York, 1963, Appendix B.

[20] I.M. Govil *et al.*, Phys. Lett. **B197**, 515 (1987).

[21] J.R. Huizenga *et al.*, Phys. Rev. C **40**, 668 (1989).

[22] W. Bauer, Phys. Rev. C **51**, 803 (1995).

[23] B. Borderie *et al.*, Phys. Lett. **B205**, 26 (1988).

[24] K. Kwiatkowski *et al.*, Phys. Lett. **B171**, 41 (1986).

[25] B.V. Jacak *et al.*, Phys. Rev. C **35**, 1751 (1987).

[26] G.F. Peaslee *et al.*, Phys. Rev. C **49**, R2271 (1994).

[27] K. Tso *et al.*, Phys. Lett. **B361**, 25 (1995).

[28] R. T. de Souza *et al.*, Phys. Lett. **B300**, 29 (1993).

[29] W. C. Hsi *et al.*, Phys. Rev. Lett. **73**, 3367 (1994).

[30] S. C. Jeong *et al.*, Phys. Rev. Lett. **72**, 3468 (1994).

[31] R.J. Charity *et al.*, Nucl. Phys. **A483**, 391 (1988).

[32] W.A. Friedman, Phys. Rev. C **42**, 667 (1990).

[33] A. S. Hirsch, preprint, Purdue University (1995)

[34] Y. D. Kim *et al.*, Phys. Rev. C **45**, 338 (1992).

[35] L.W. Phair, Ph.D. Thesis, Michigan State University (1993).

[36] J. Aichelin, Phys. Rep. 202, 233 (1991).

[37] C.O. Dorso and J. Aichelin, Phys. Lett. **B345**, 197 (1995).

[38] T. Glasmacher, C.K. Gelbke, and S. Pratt, Phys. Lett. **B314**, 265 (1993).

[39] R. Donangelo and S.R. Souza, Phys. Rev. C **52**, 326 (1995).

[40] L. G. Moretto *et al.* Phys. Rev. Lett. **74**, 1530 (1995).

[41] L. Phair *et al.*, Phys. Rev. Lett. **75**, 213 (1995).

[42] L.G. Moretto, D.N. Delis, and G.J. Wozniak, Phys. Rev. Lett. **71**, 3935 (1993).

[43] H.M. Xu *et al.*, Phys. Rev. C **49**, R1778 (1994).

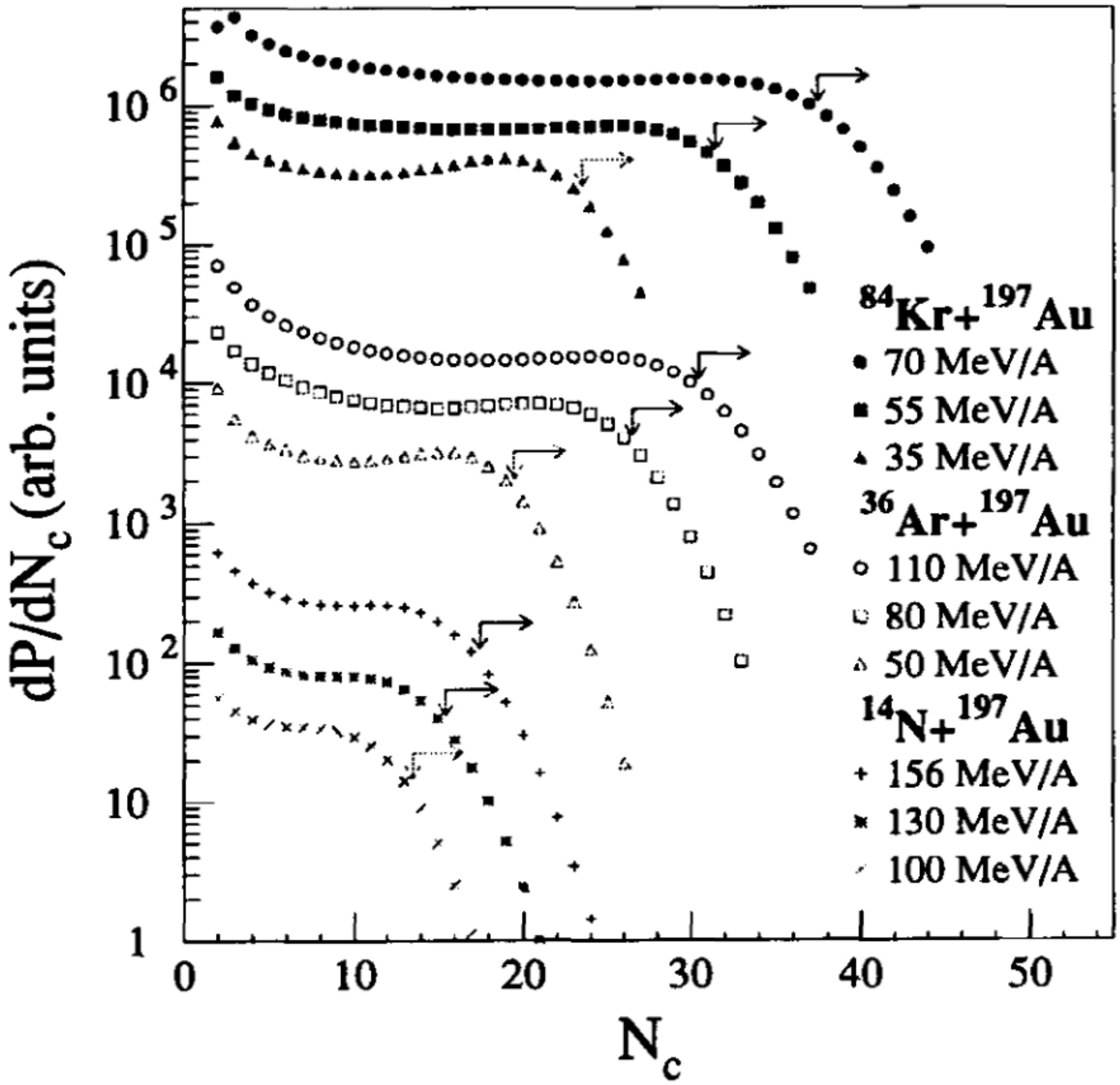

Figure 4.1. Charged-particle multiplicity distributions measured in the reactions ^{84}Kr + ^{197}Au at E/A = 35-70 MeV, ^{36}Ar + ^{197}Au at E/A = 50-110 MeV, and ^{14}N + ^{197}Au at E/A = 100-156 MeV.

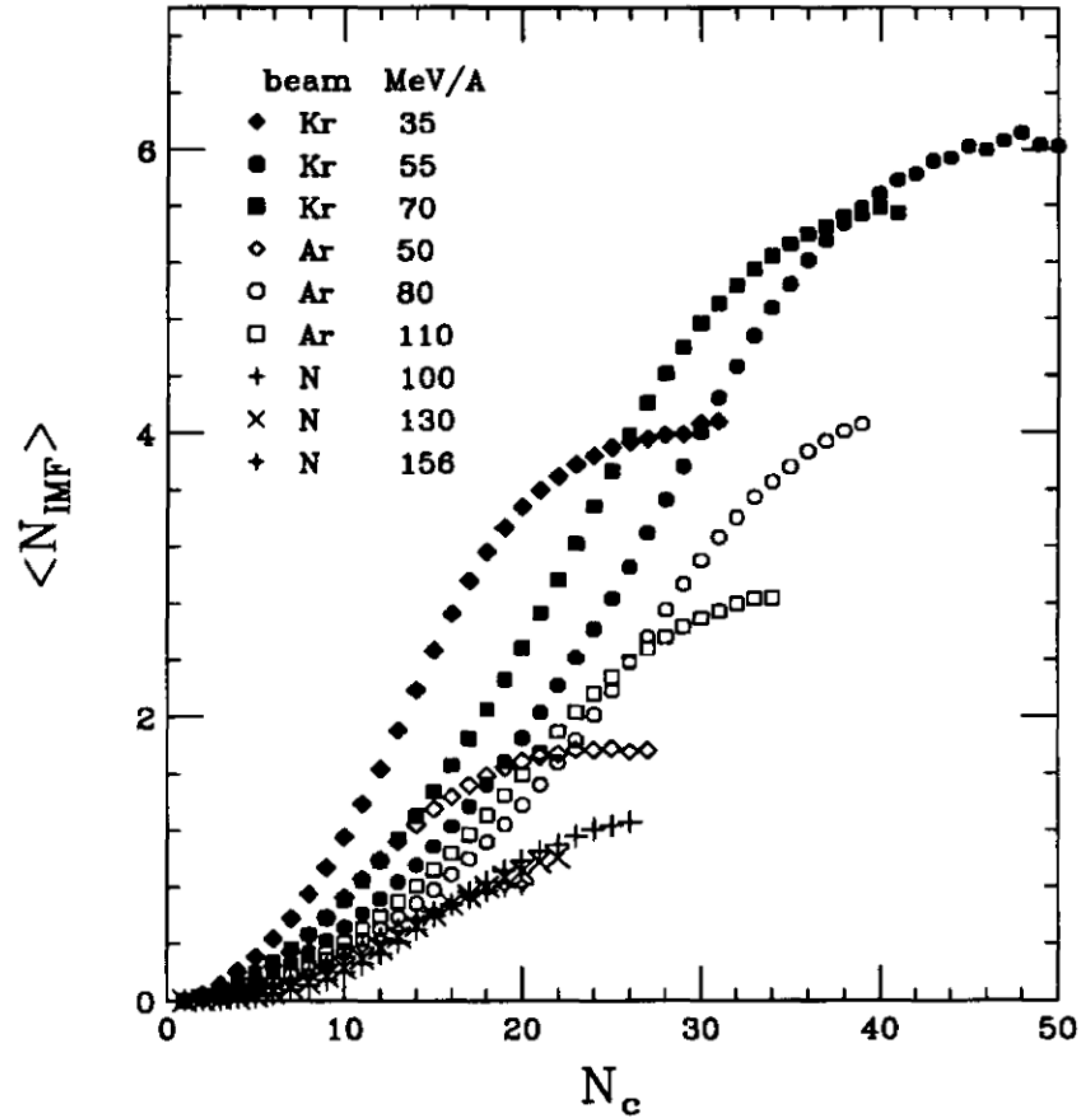

Figure 4.2. Dependence of the mean IMF multiplicity on the charged-particle multiplicity for the reactions ^{84}Kr + ^{197}Au at E/A = 35-70 MeV, ^{36}Ar + ^{197}Au at E/A = 50-110 MeV, and ^{14}N + ^{197}Au at E/A = 100-156 MeV.

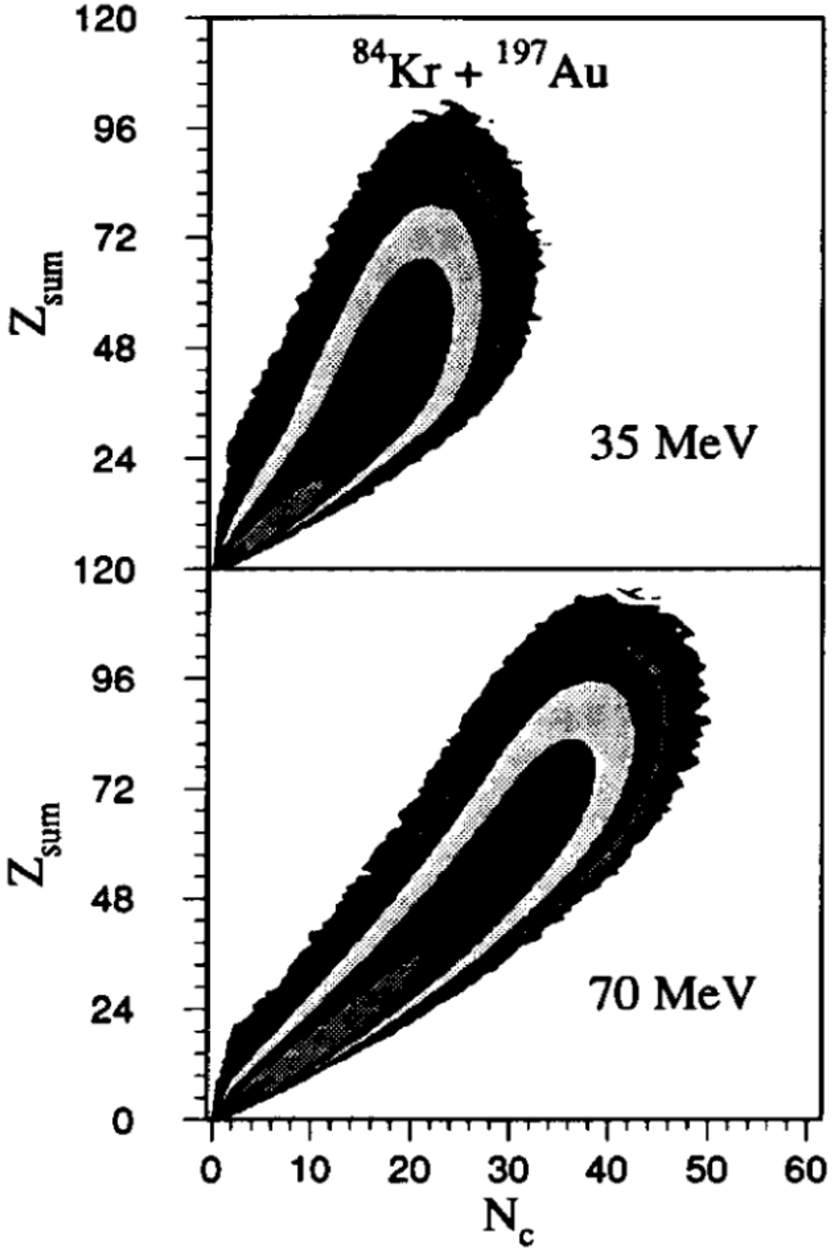

Figure 4.3. Dependence of the total detected charge, Z_{sum}, on the charged-particle multiplicity for the reaction ^{84}Kr + ^{197}Au at E/A = 35 MeV (top panel) and E/A = 70 MeV (bottom panel).

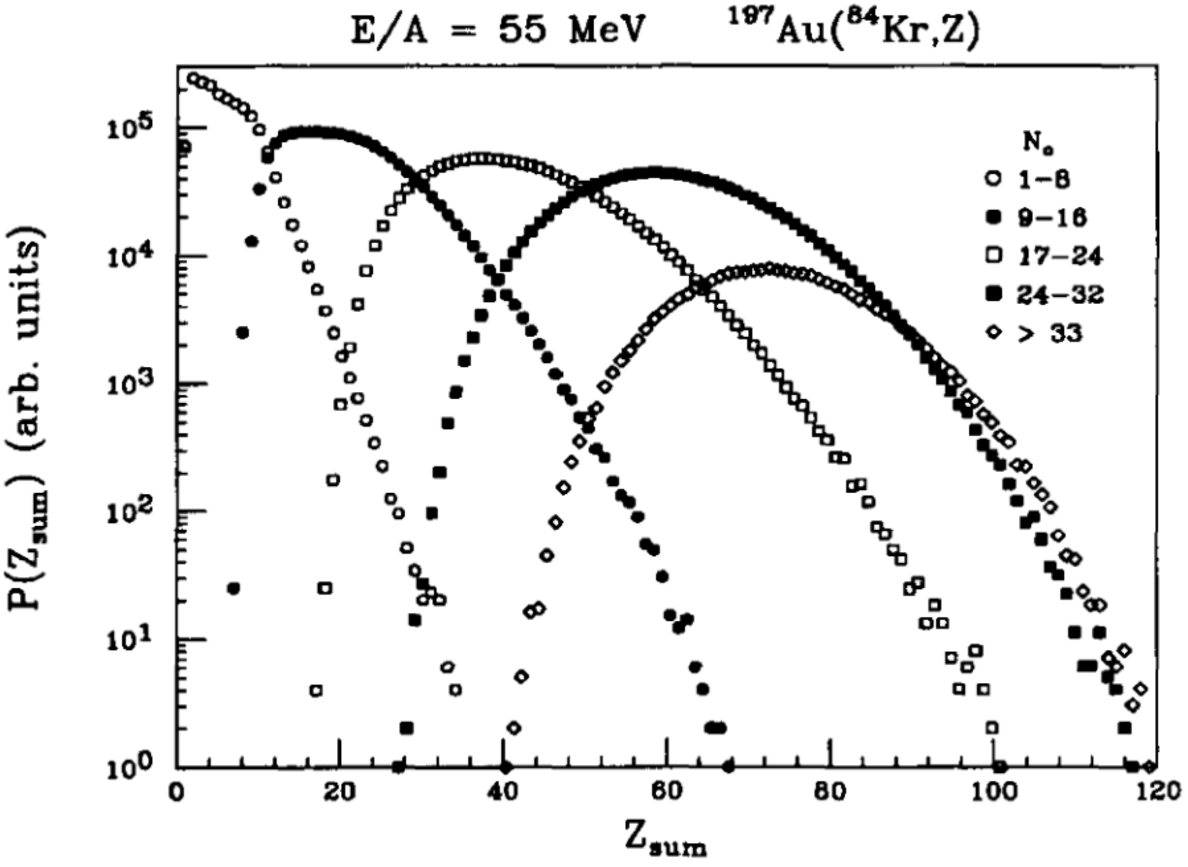

Figure 4.4. Total detected charge distributions for different cuts in charged-particle multiplicity in the reaction ^{84}Kr + ^{197}Au at E/A = 55 MeV.

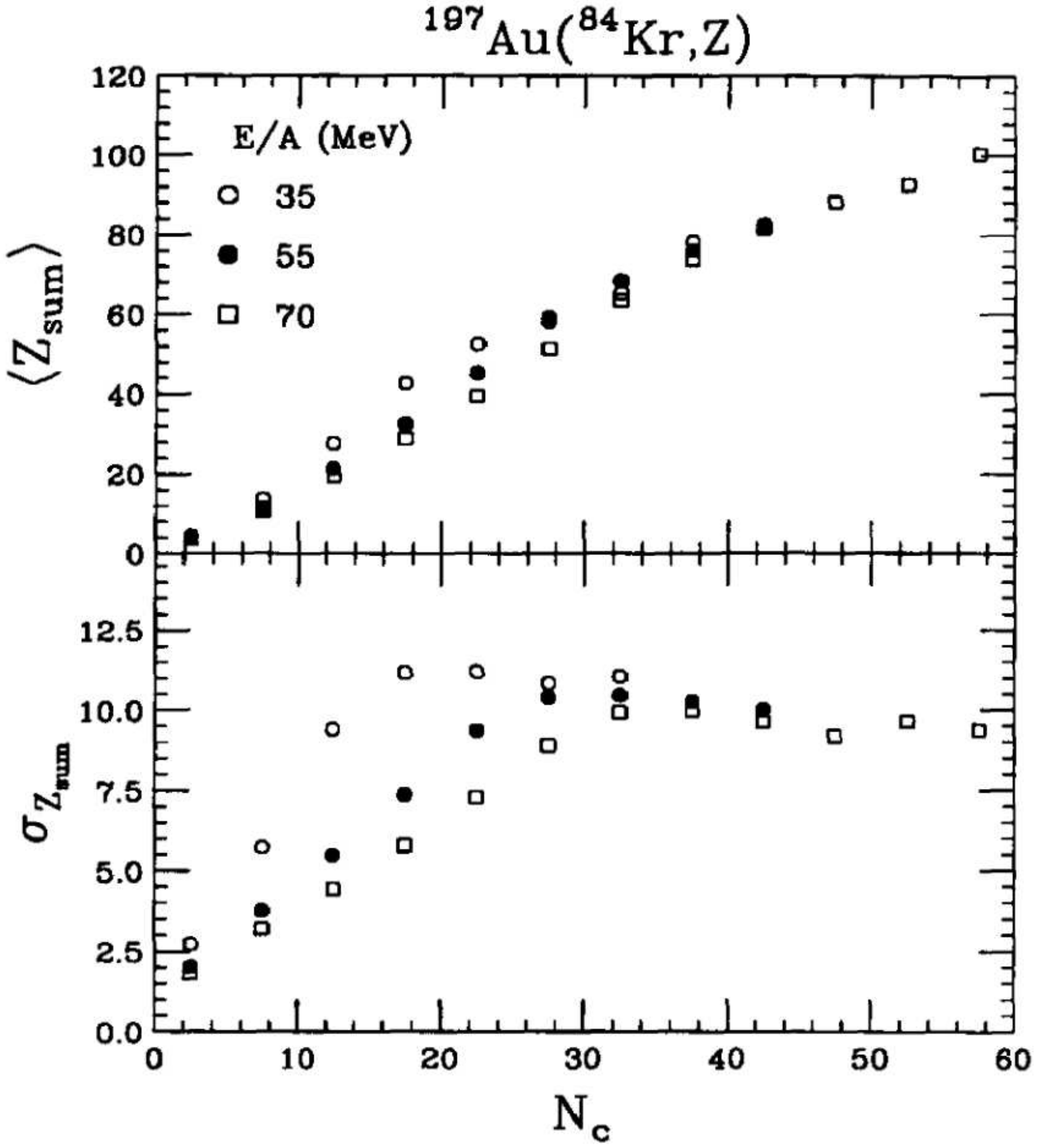

Figure 4.5. Dependence of the mean (top panel) and the variance (bottom panel) of the total detected charge distribution on the charged-particle multiplicity in the reaction ^{84}Kr + ^{197}Au at E/A = 35 (open circles), 55 (closed circles), and 70 MeV/A (open squares).

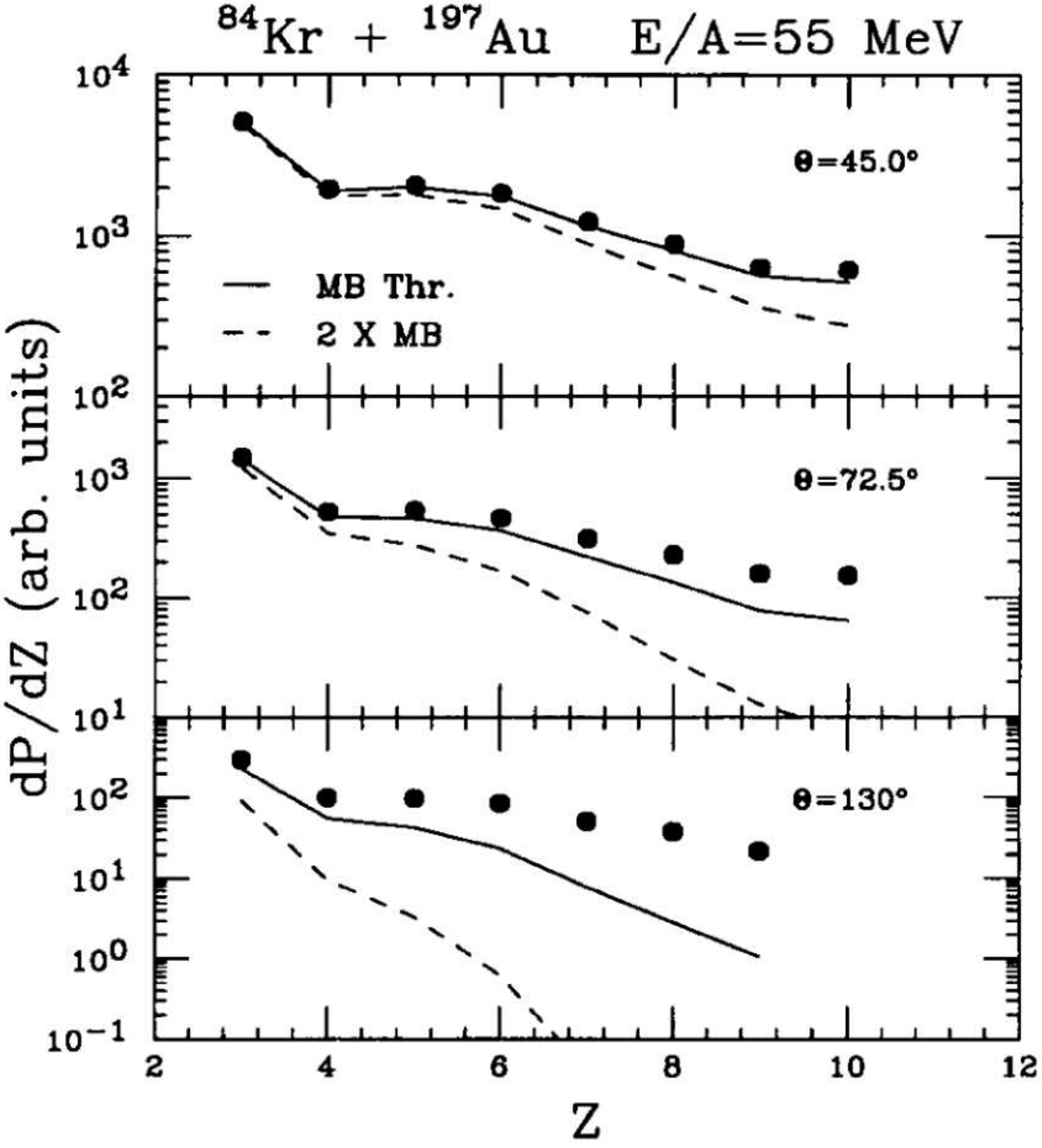

Figure 4.6. Inclusive Z distributions measured in the ion-chamber telescopes at θ_{lab} = 45° (top panel), 72.5° (middle panel), and 130° (bottom panel) in the reaction ^{84}Kr + ^{197}Au at E/A = 55 MeV. The solid and dashed lines correspond to software thresholds equal to the Miniball thresholds and twice the Miniball thresholds, respectively.

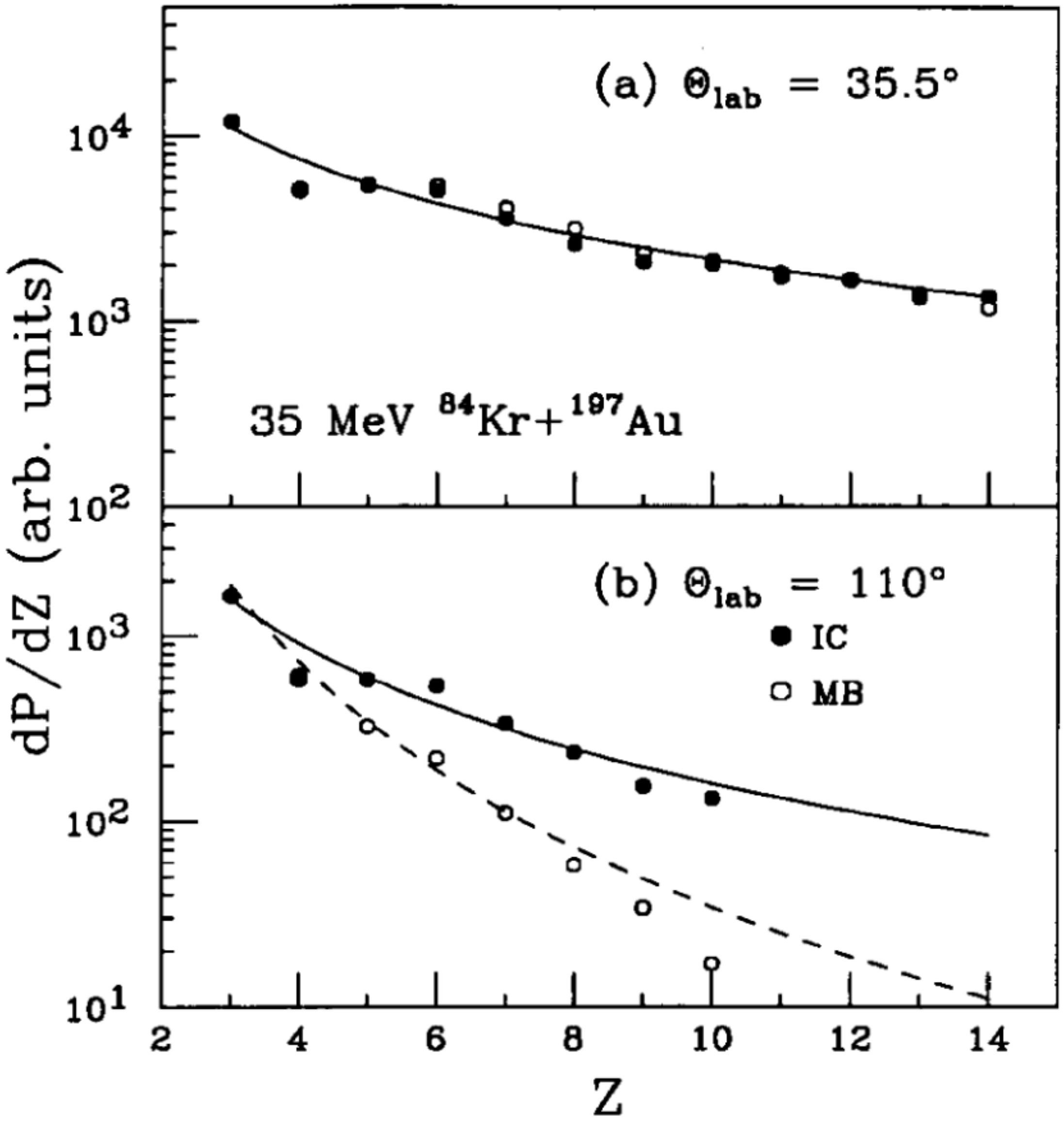

Figure 4.7. (a) Inclusive Z distributions measured in the ion-chamber telescopes (solid points) and the Miniball detectors (open points) at $\theta_{lab} = 35.5°$ in the reaction ^{84}Kr + ^{197}Au at E/A = 35 MeV. The line corresponds to a power-law fit with the form $P(Z) \approx Z^{-\tau}$. (b) The same as in panel (a) expect at $\theta_{lab} = 110°$. The solid and dashed lines correspond to power-law fits to the data measured in the ion-chamber telescope and Miniball detectors, respectively. The values of the fit parameter, τ, are displayed in Figure 4.8.

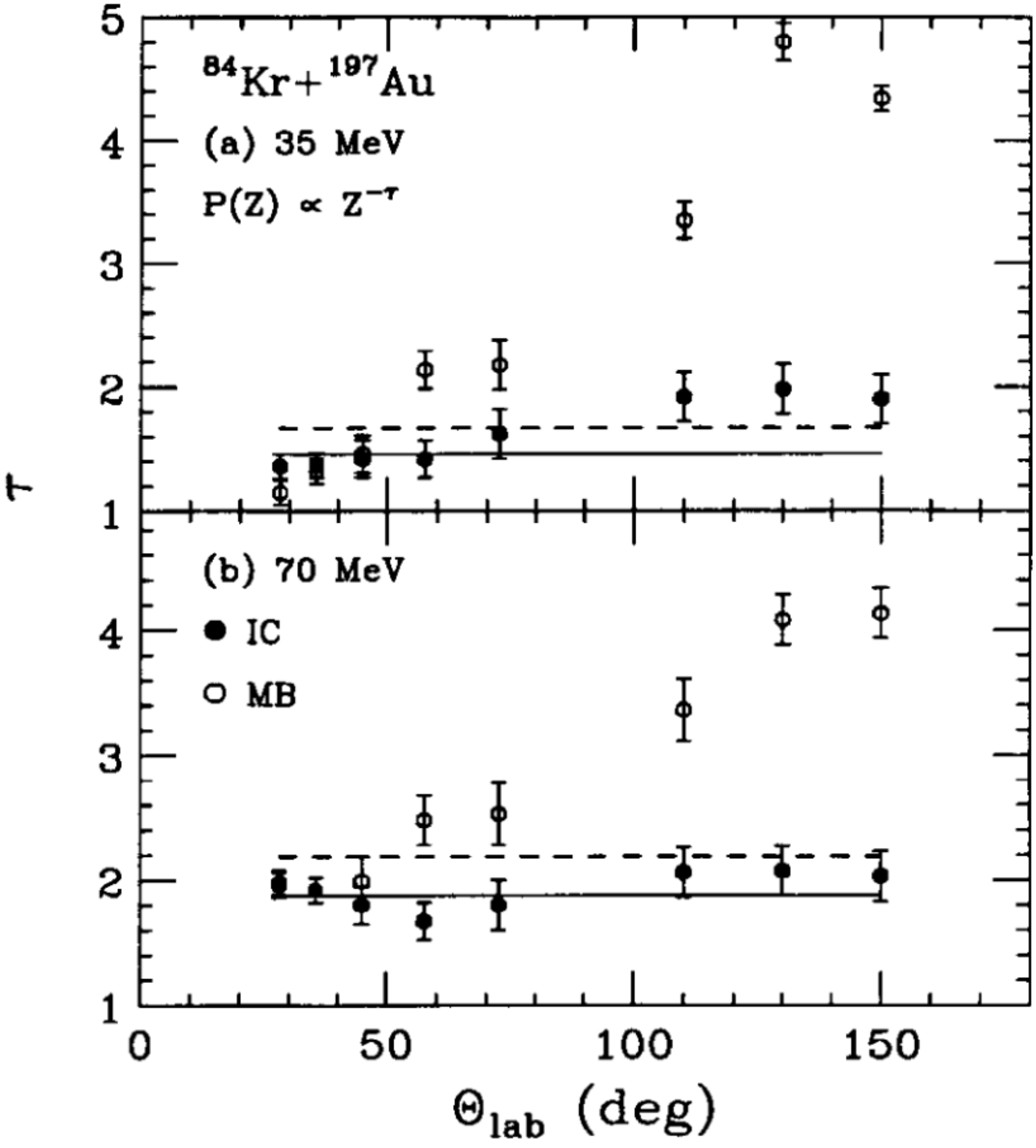

Figure 4.8. (a) Dependence of the τ parameter on θ_{lab} from power-law fits to the Z distributions measured in the ion-chamber telescopes (solid points) and the Miniball detectors (open points) in the reaction ^{84}Kr + ^{197}Au at E/A = 35 MeV. (b) The same as in panel (a) except at E/A = 70 MeV.

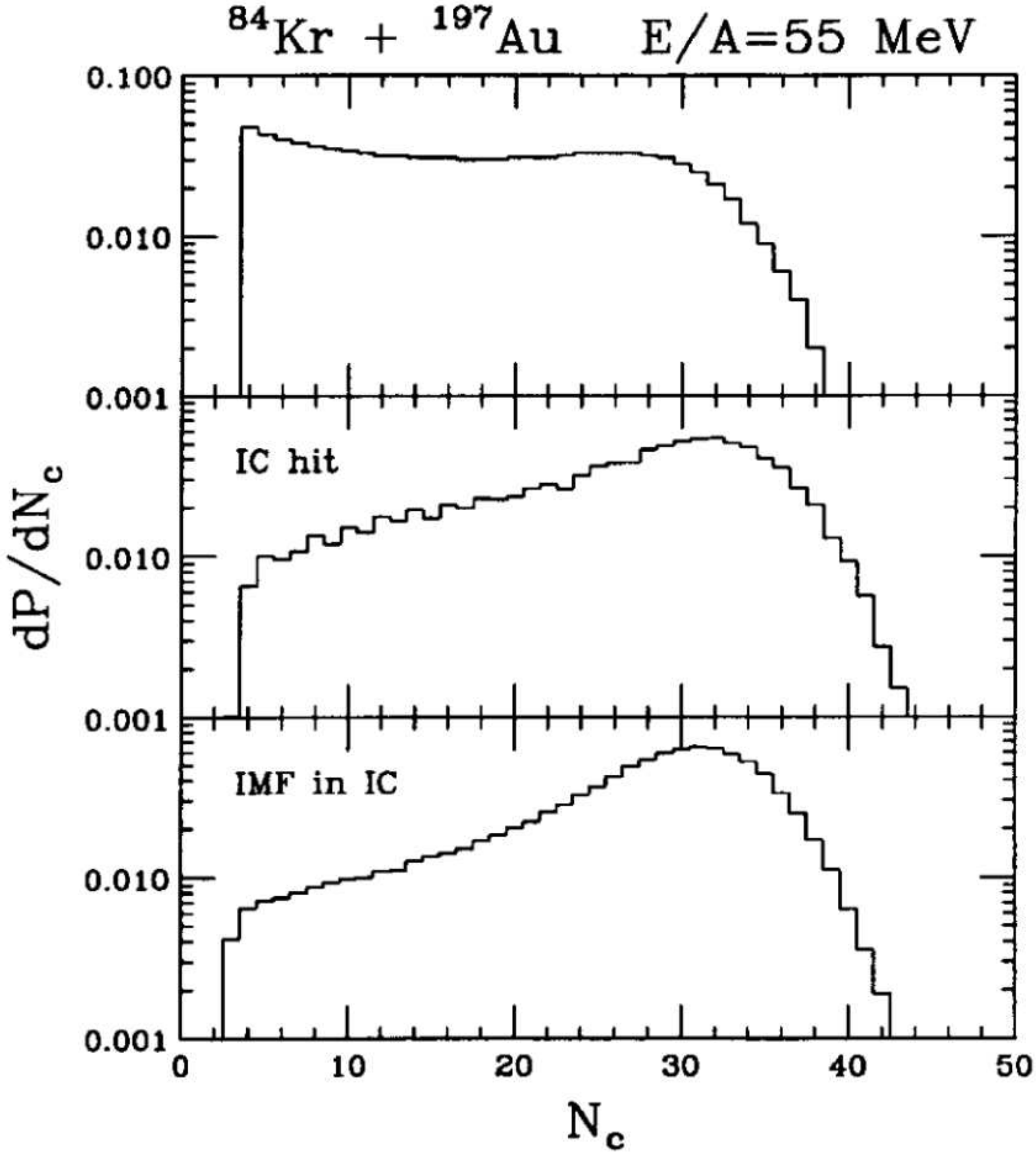

Figure 4.9. (a) The charged-particle multiplicity distribution measured in the reaction ^{84}Kr + ^{197}Au at E/A = 55 MeV with the requirement of detecting two or more charged particles in the Miniball/Miniwall detector array. (b) The same as in panel (a) with the additional requirement of detecting a charged particle in an ion-chamber telescope. (c) The same as in panel (a) with the additional requirement of detecting an IMF in an ion-chamber telescope.

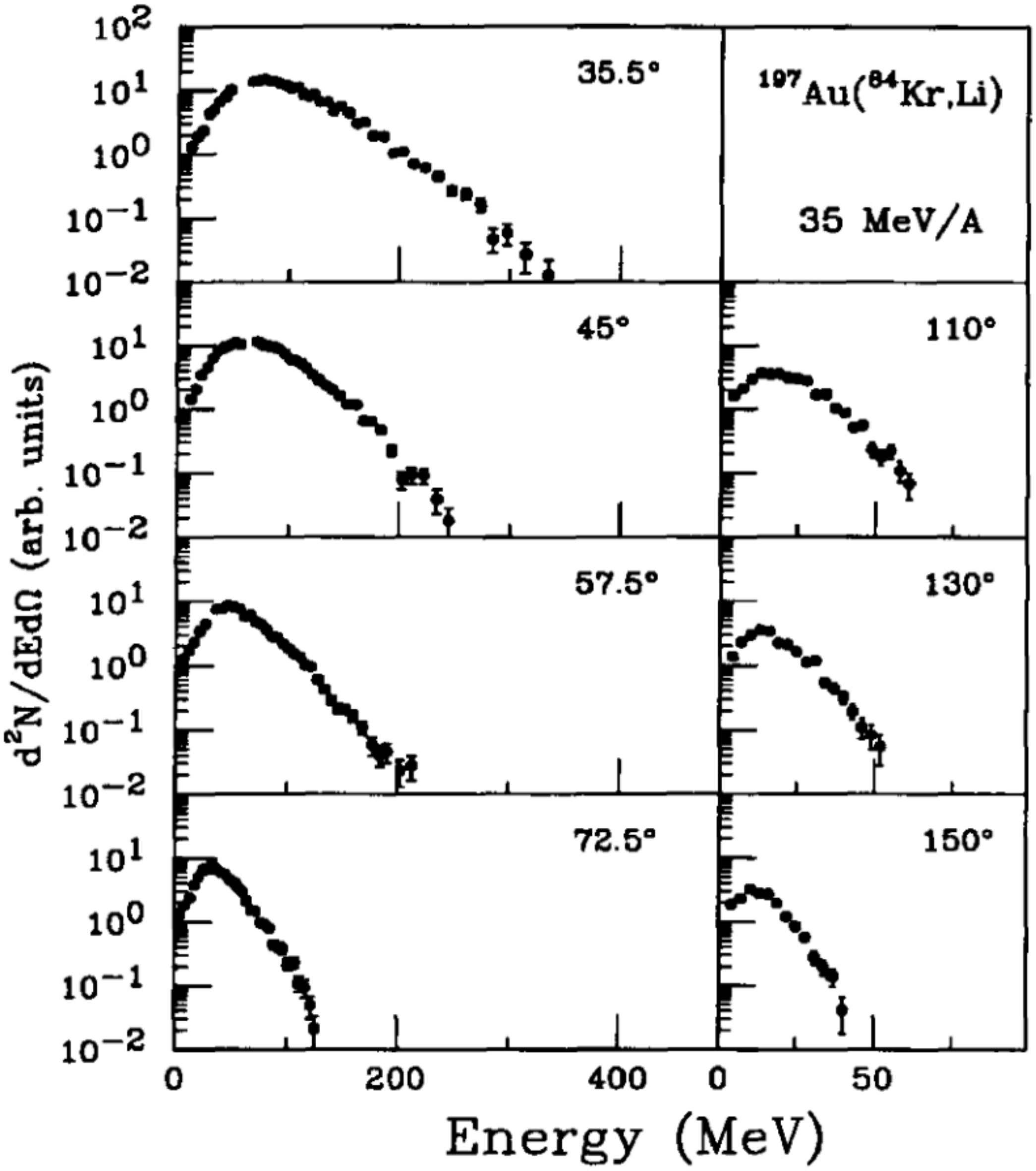

Figure 4.10. Kinetic energy spectra of lithium fragments measured in the ion-chamber telescopes for central and midcentral collisions ($b/b_{max} \leq 0.4$) in the reaction ^{84}Kr + ^{197}Au at E/A = 35 MeV.

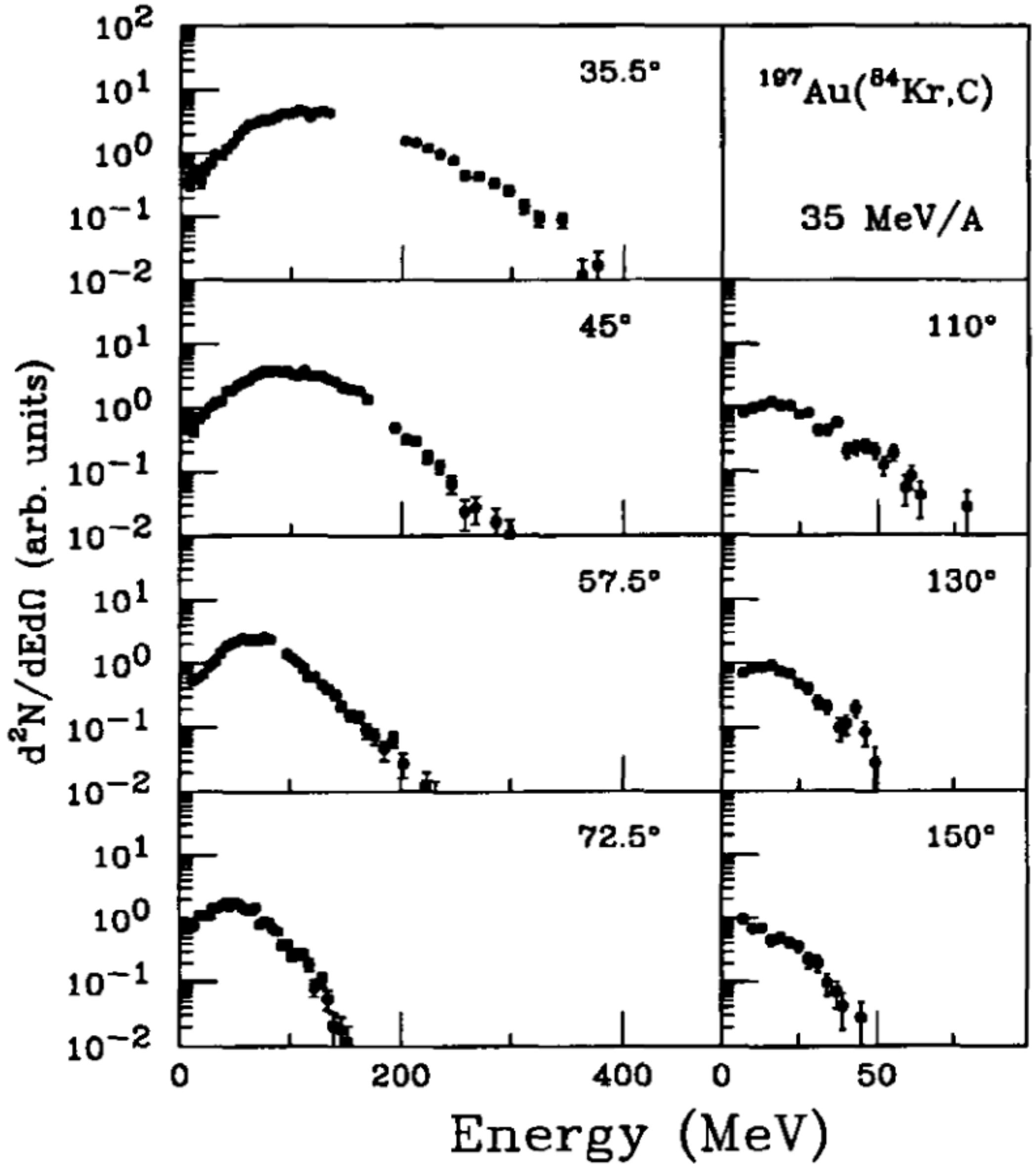

Figure 4.11. The same as in Figure 4.10 except for carbon fragments.

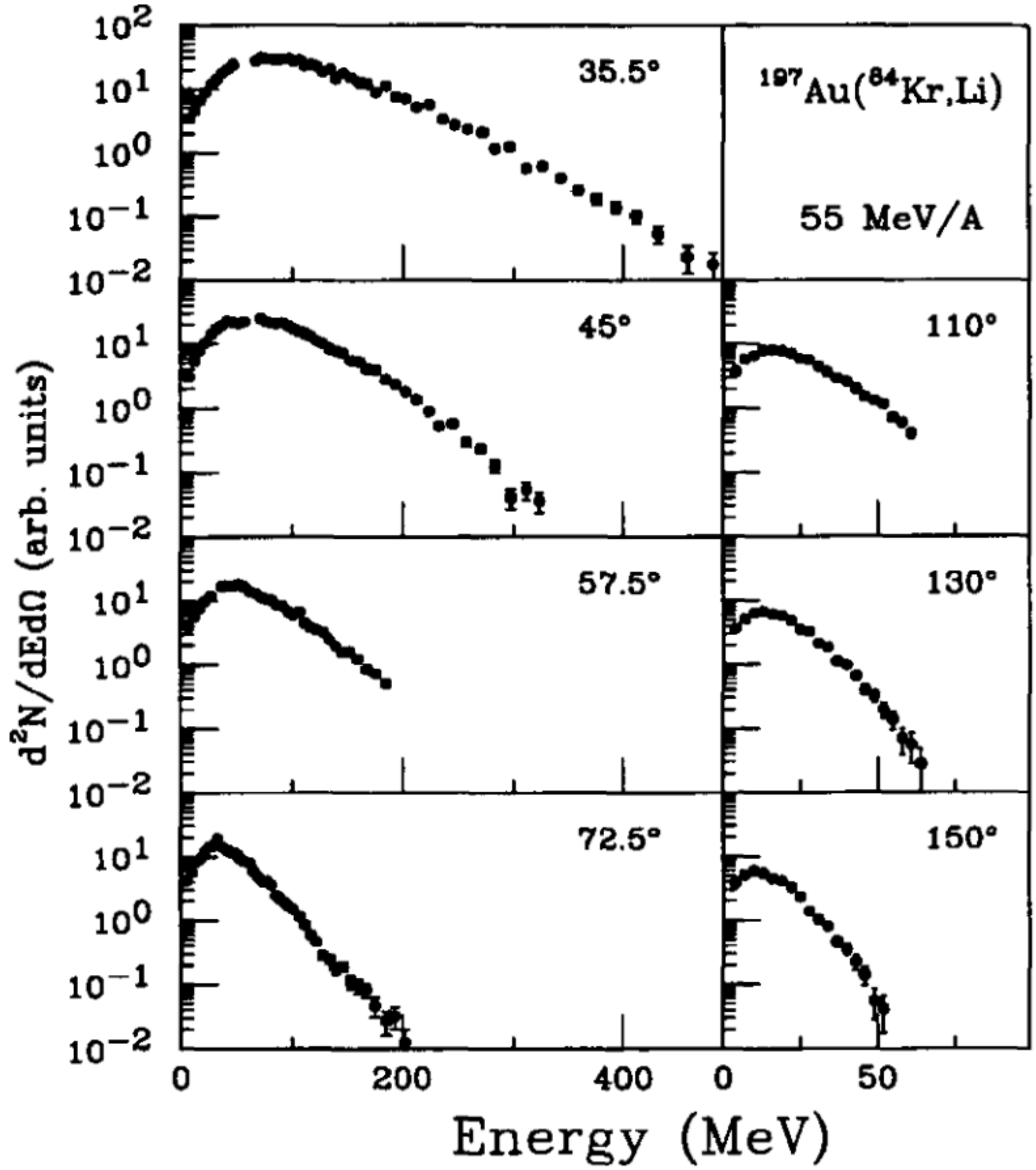

Figure 4.12. The same as in Figure 4.10 except at E/A = 55 MeV.

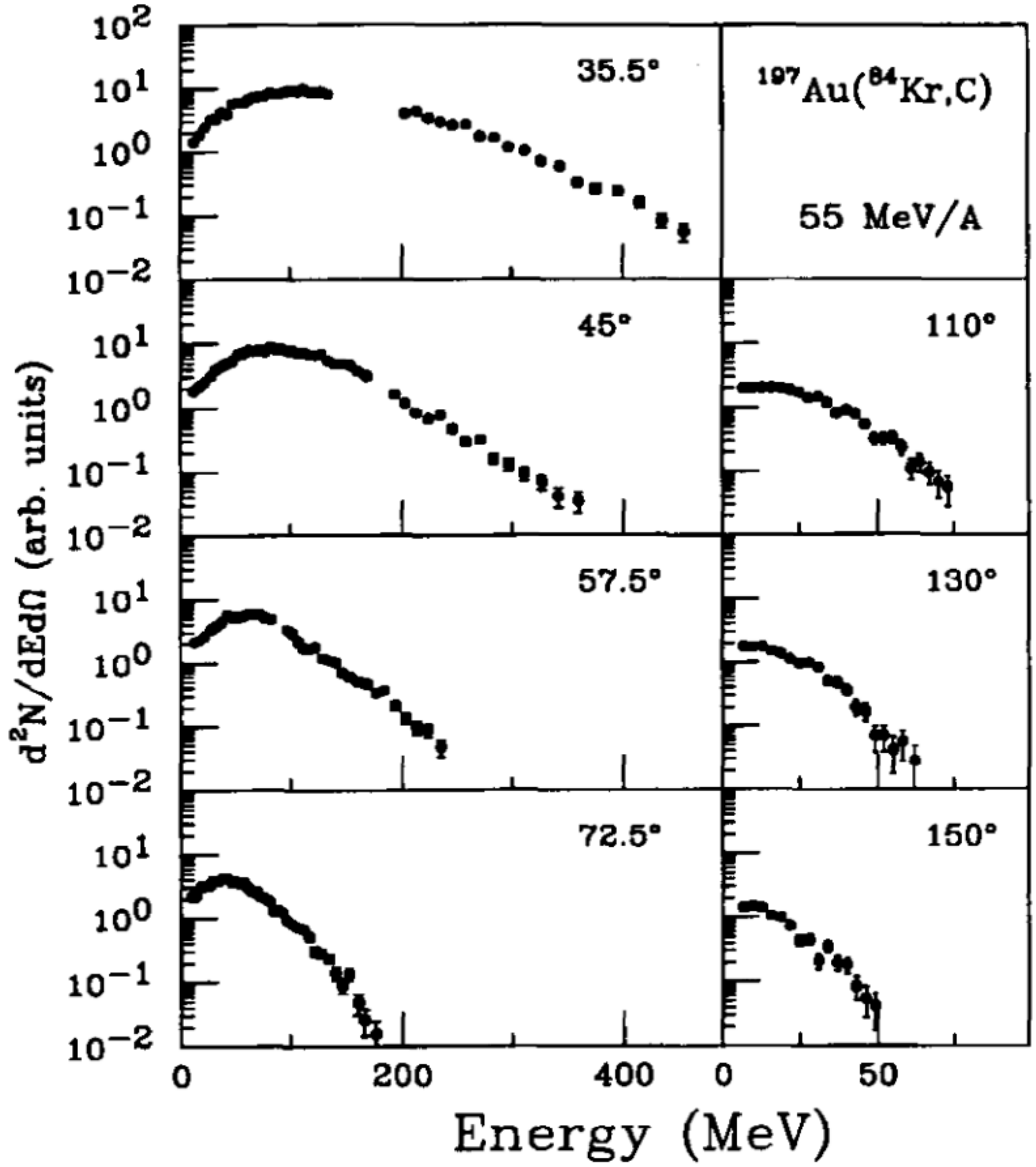

Figure 4.13. The same as in Figure 4.10 except for carbon fragments at E/A = 55 MeV.

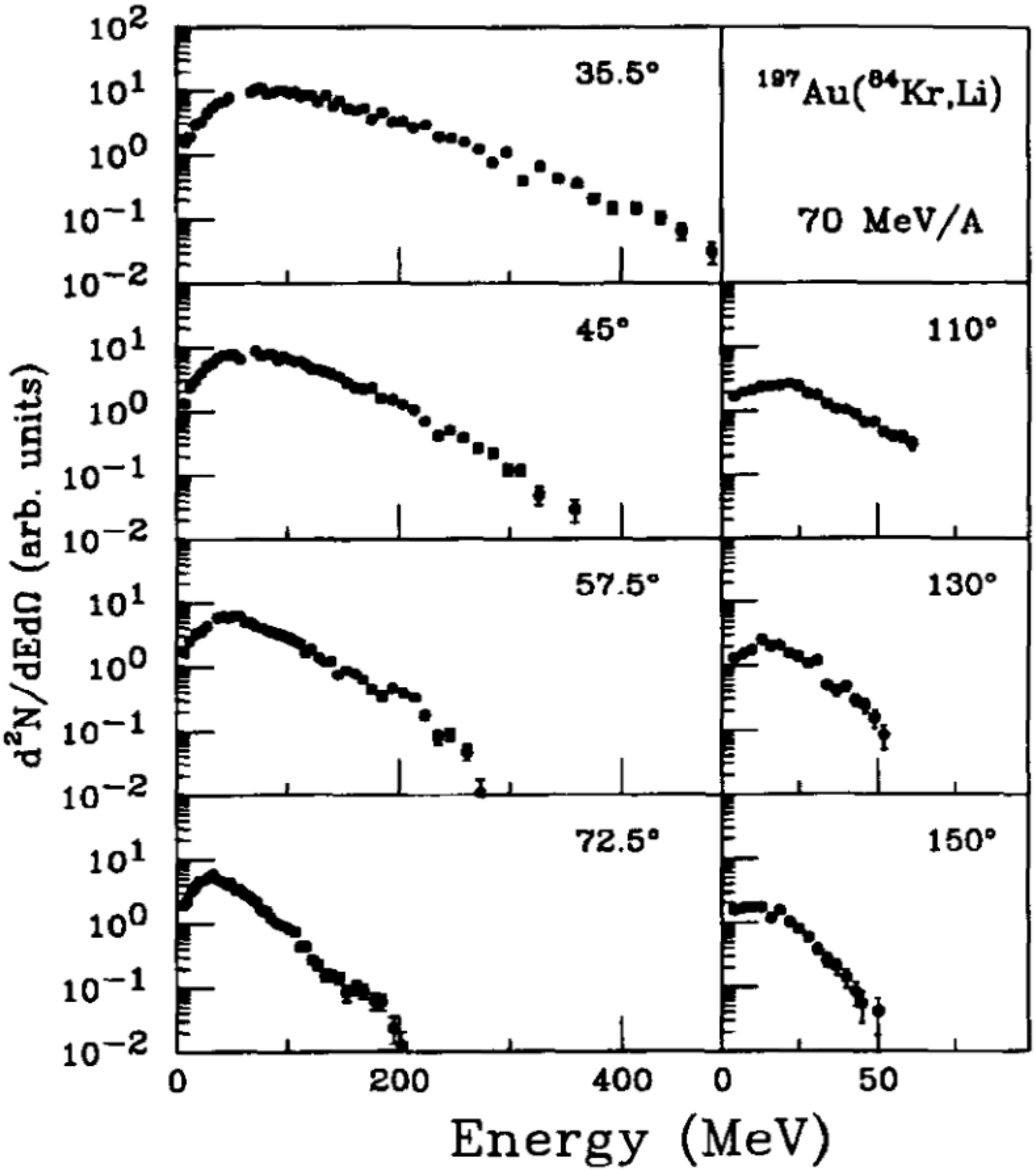

Figure 4.14. The same as in Figure 4.10 except at E/A = 70 MeV.

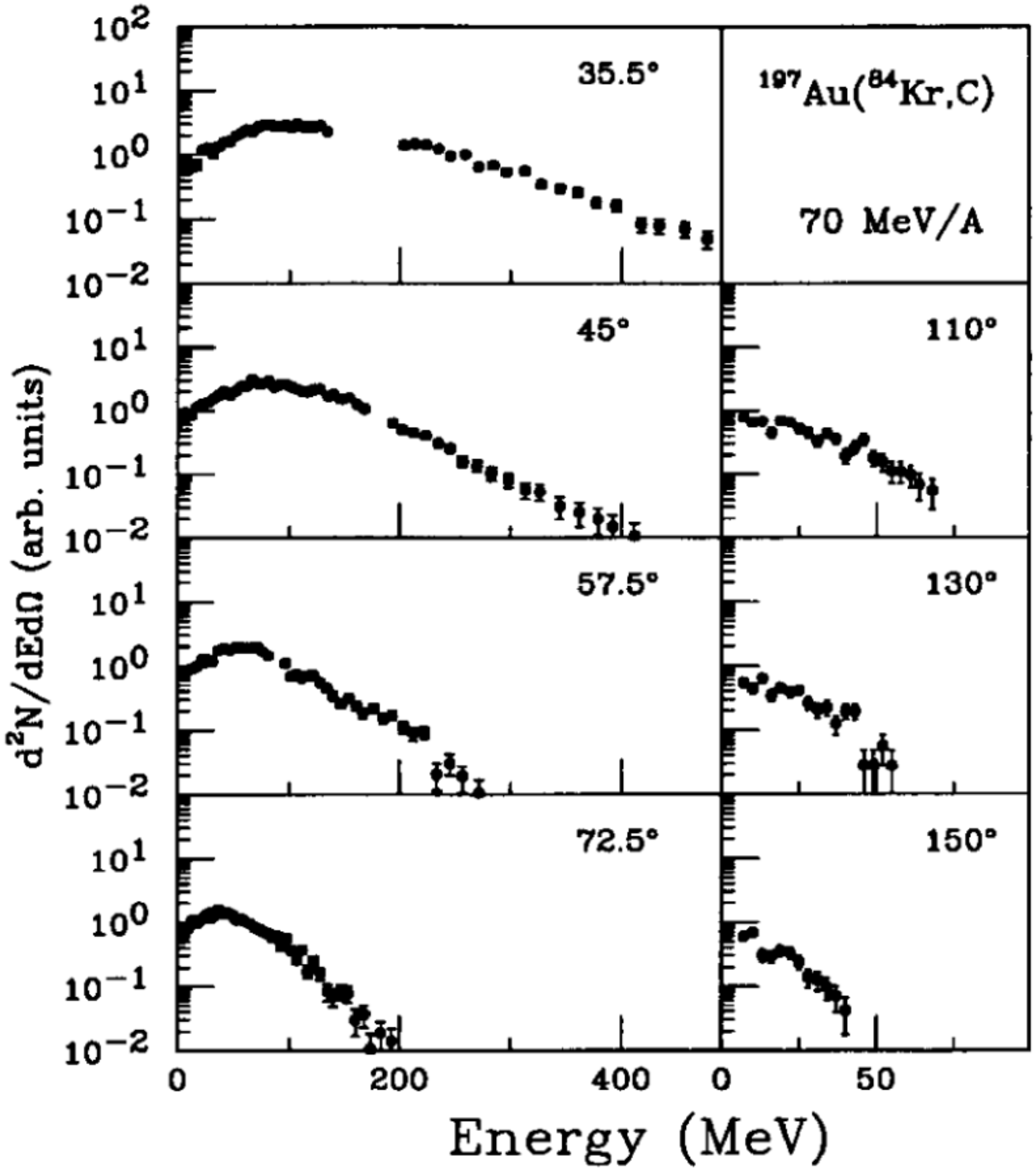

Figure 4.15. The same as in Figure 4.10 except for carbon fragments at E/A = 70 MeV.

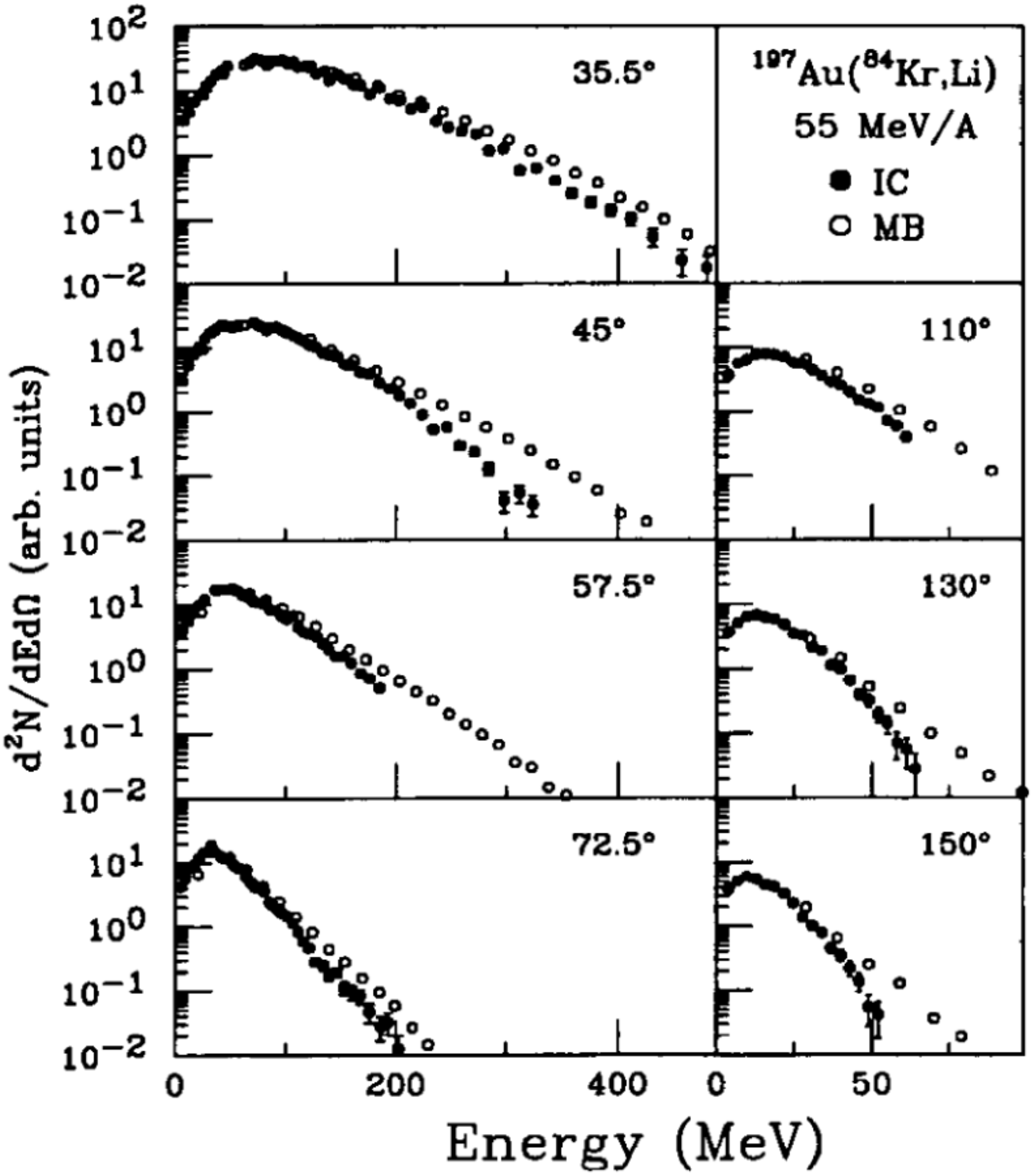

Figure 4.16. Comparison between kinetic energy spectra for lithium fragments measured in the ion-chamber telescopes ($b/b_{max} \leq 0.4$, solid points) and the Miniball detectors ($b/b_{max} \leq 0.2$, open points) in the reaction ^{84}Kr + ^{197}Au at E/A = 55 MeV.

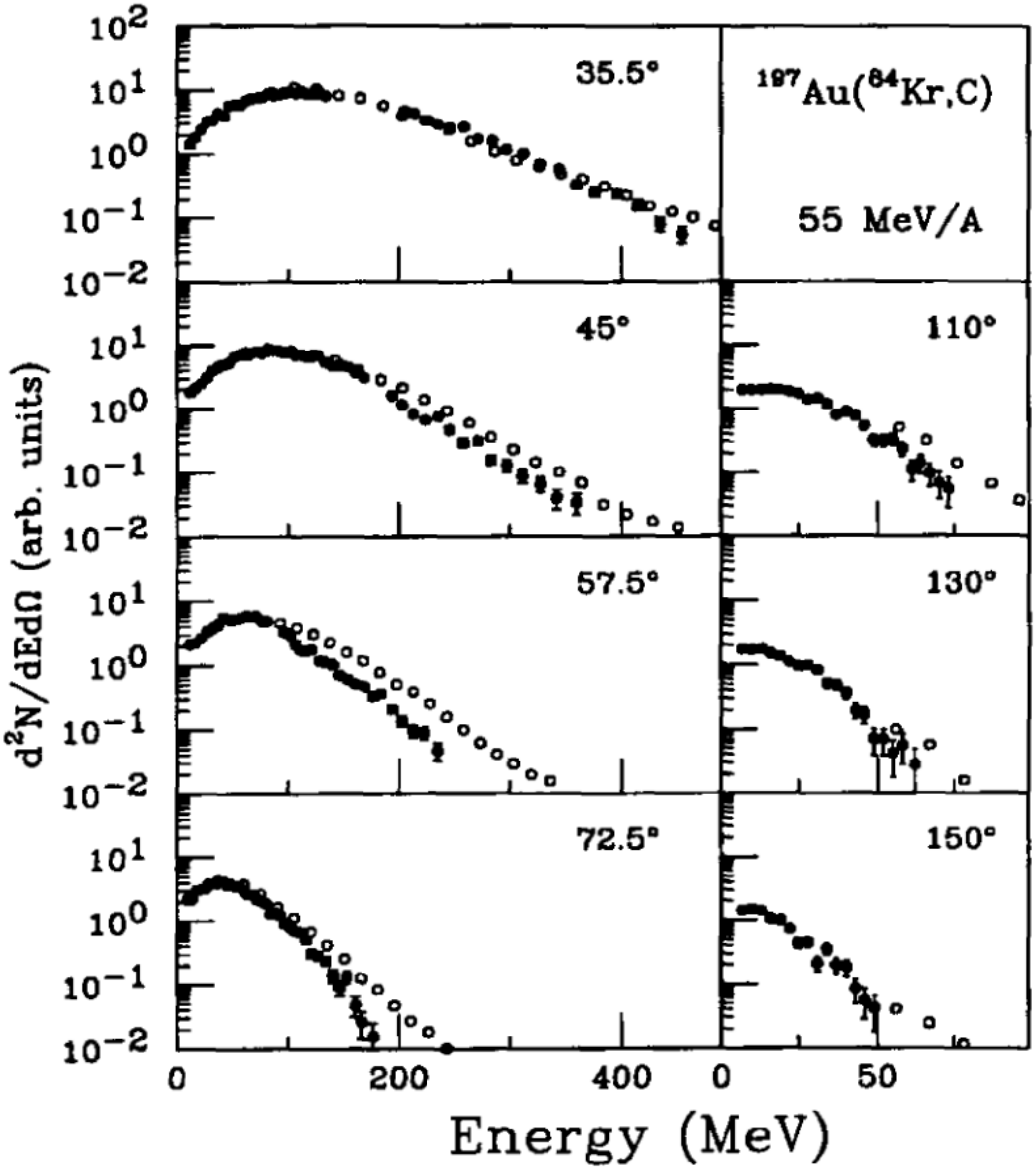

Figure 4.17. The same as in Figure 4.16 except for carbon fragments.

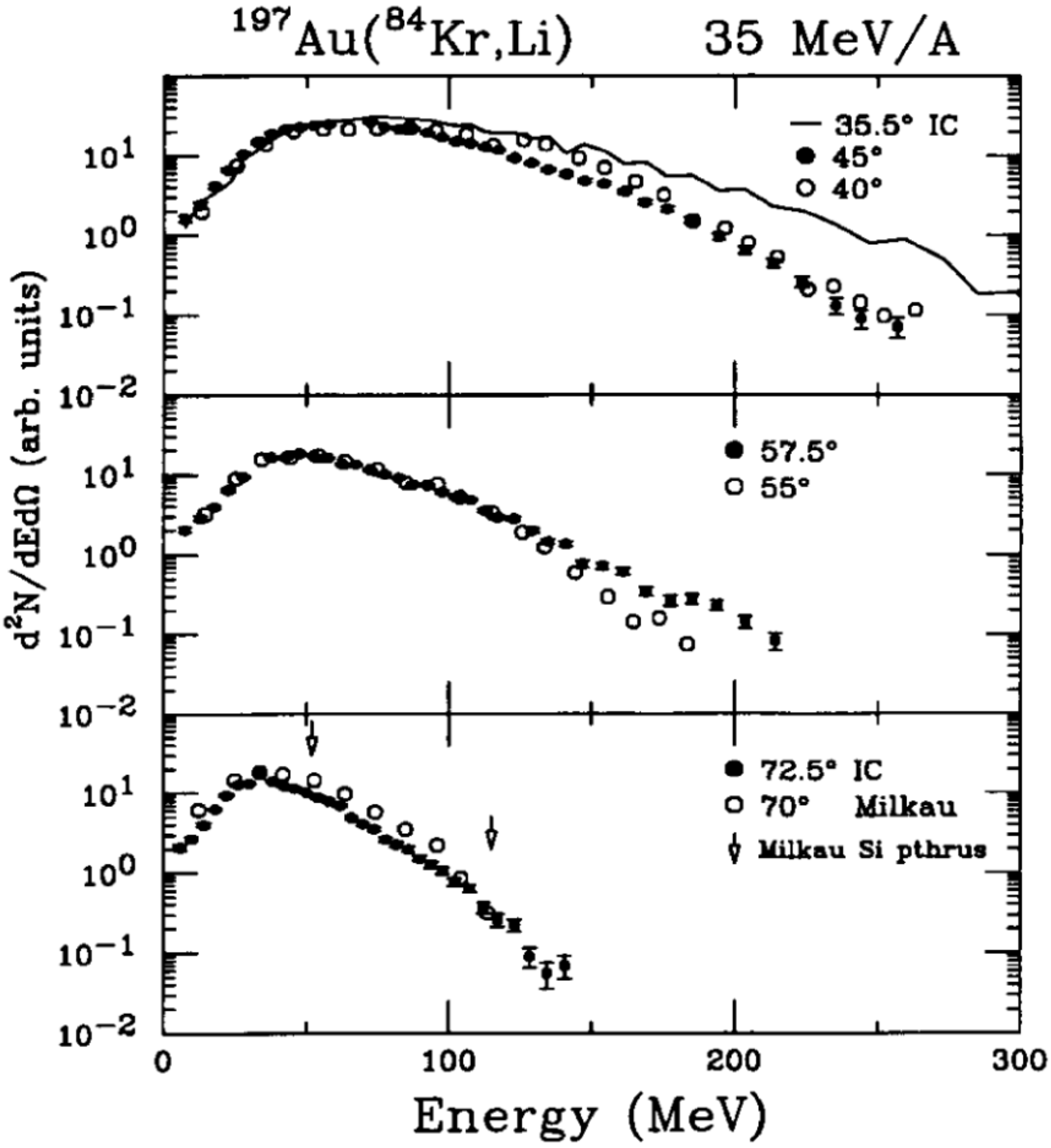

Figure 4.18. Comparison between inclusive kinetic energy spectra for lithium fragments measured in the ion-chamber telescopes (solid points and solid line) and spectra measured by Milkau *et al.* (open points, Ref. [7]) in the reaction ^{84}Kr + ^{197}Au at E/A = 35 MeV. See text for a description of the arrows.

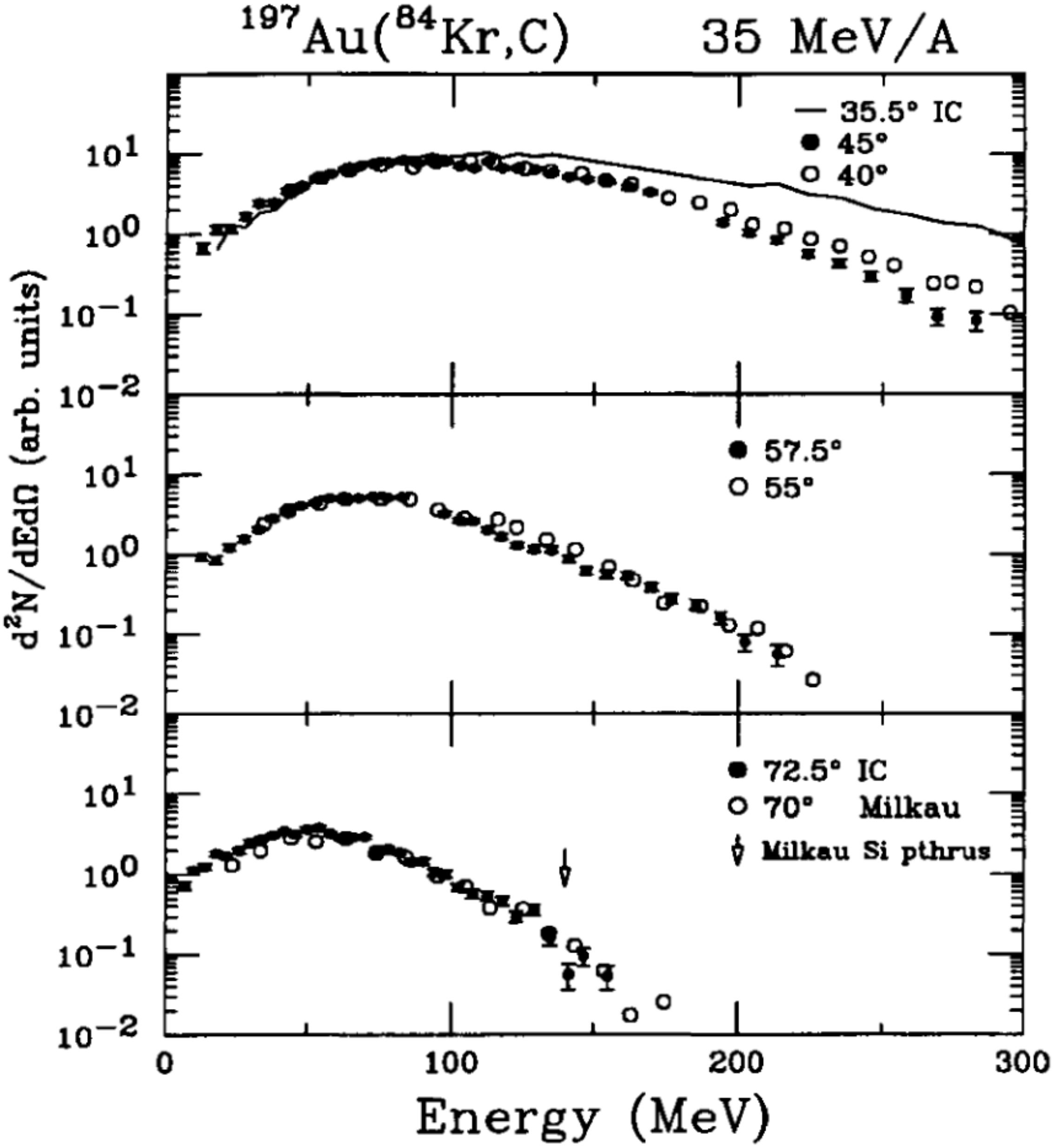

Figure 4.19. The same as in Figure 4.18 except for carbon fragments.

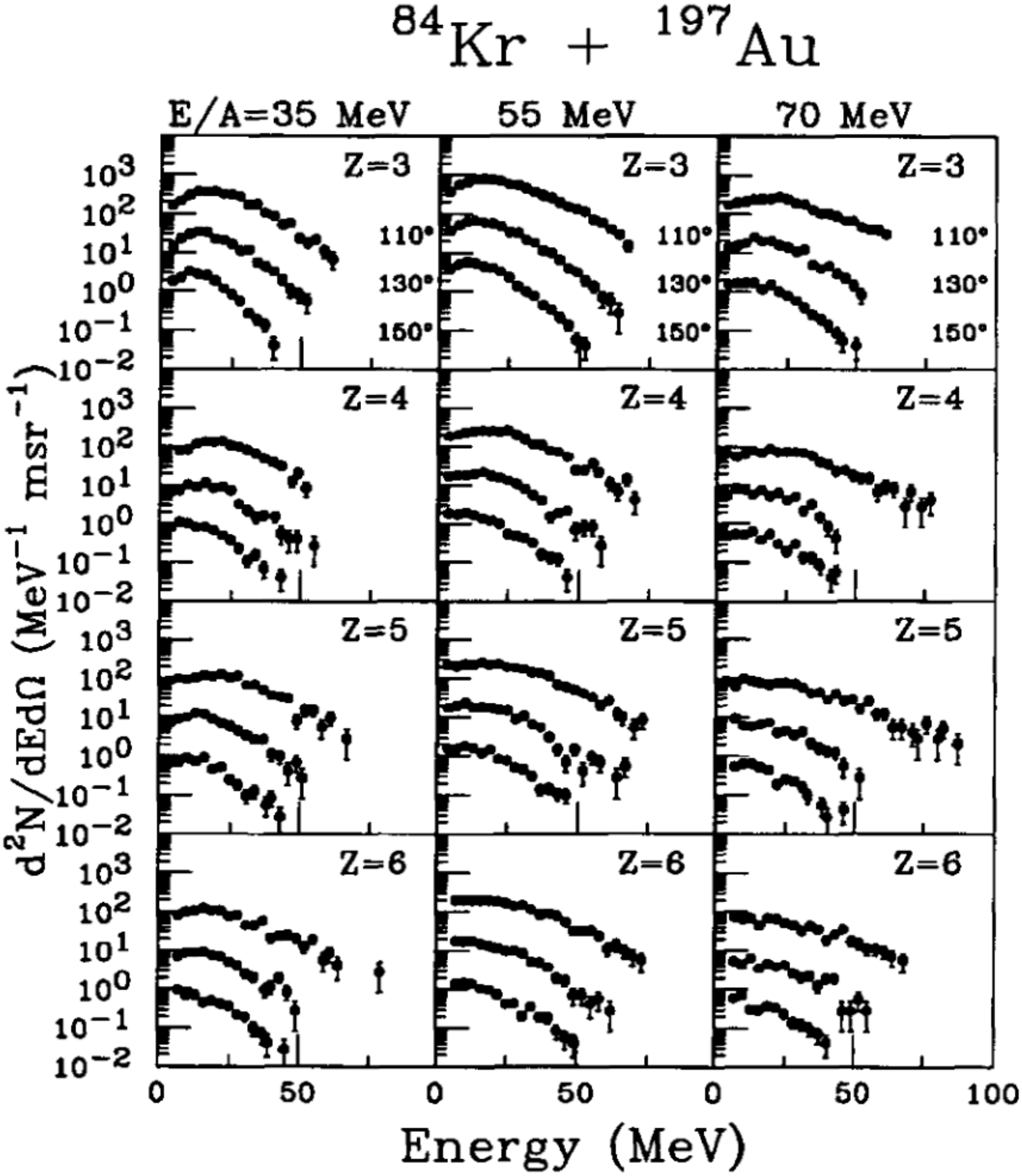

Figure 4.20. Backward-angle kinetic energy spectra of fragments (Z = 3 to 6) measured in the ion-chamber telescopes for central and midcentral collisions ($b/b_{max} \leq 0.4$) in the reaction ^{84}Kr + ^{197}Au at E/A = 35, 55, and 70 MeV.

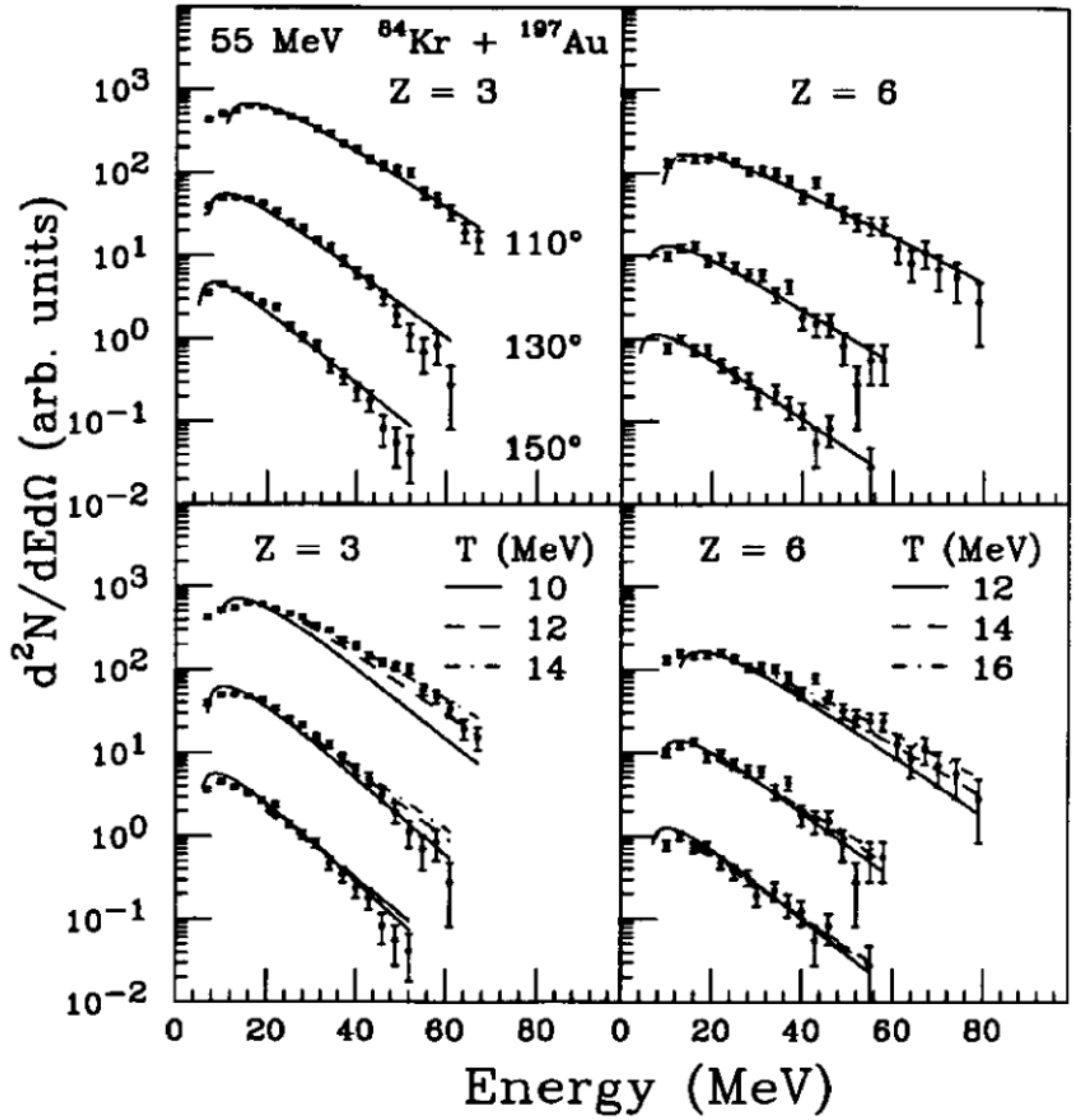

Figure 4.21. Single-source fits of backward-angle kinetic energy spectra of lithium (left panels) and carbon (right panels) fragments measured in the ion-chamber telescopes for central and midcentral collisions ($b/b_{max} \leq 0.4$) in the reaction ^{84}Kr + ^{197}Au at E/A = 55 MeV. The lines in the top panels correspond to source fits with all parameters varying freely. In the bottom panels, the lines correspond to source fits with the temperature parameter fixed to the indicated values.

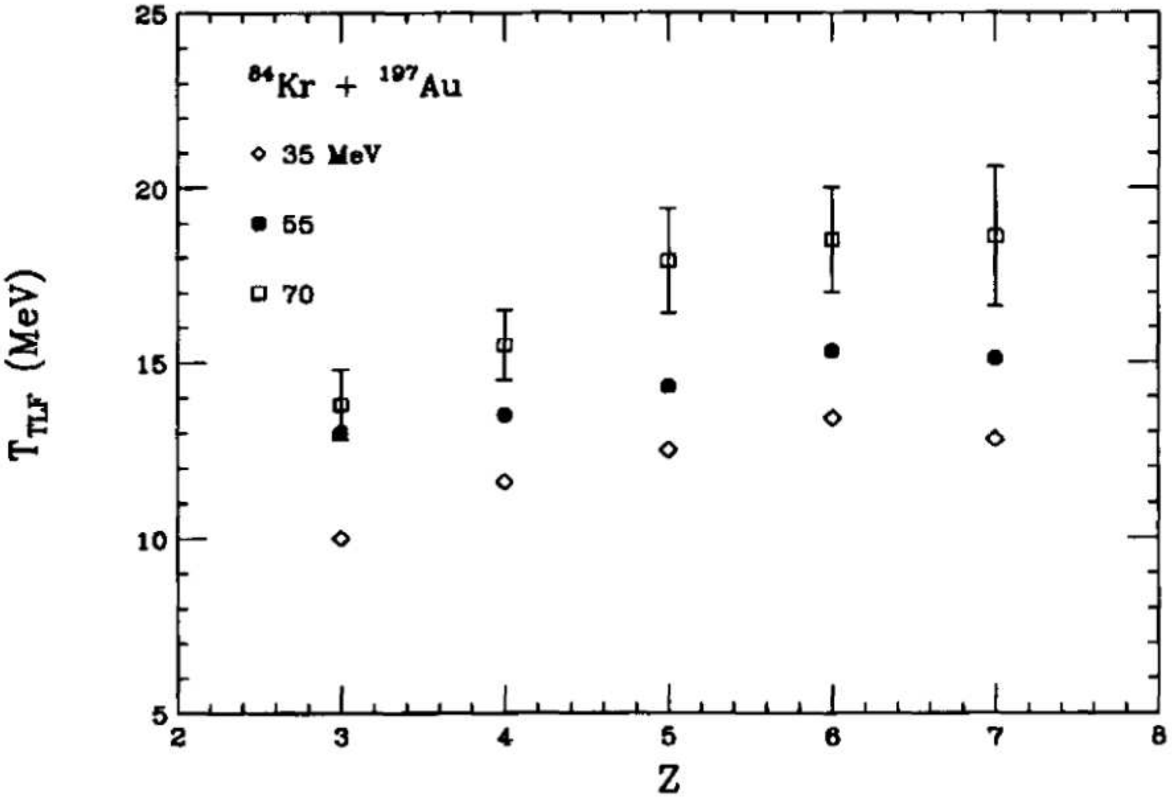

Figure 4.22. Dependence of the temperature parameter on Z from single-source fits to the backward-angle kinetic energy spectra. The fragments were measured in the ion-chamber telescopes for central and midcentral collisions ($b/b_{max} \leq 0.4$) in the reaction ^{84}Kr + ^{197}Au at E/A = 35 (open diamonds), 55 (closed circles), and 70 MeV (open squares).

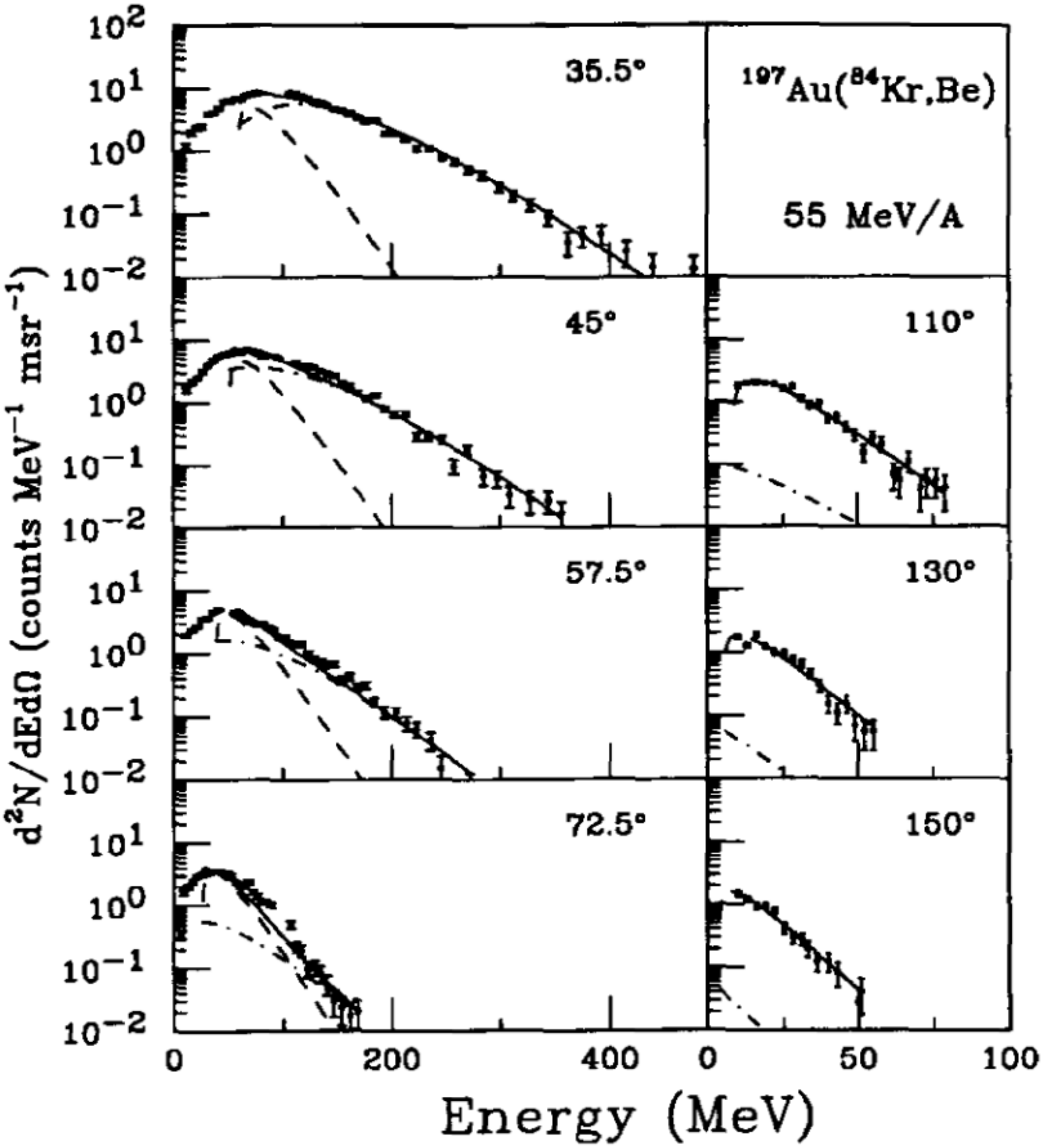

Figure 4.23. Two-source fits of kinetic energy spectra of beryllium fragments measured in the ion-chamber telescopes for central and midcentral collisions ($b/b_{max} \leq 0.4$) in the reaction ^{84}Kr + ^{197}Au at E/A = 55 MeV. The dashed line represents emission from target-like fragment (TLF); the dotdashed line represent emission from the intermediate rapidity source (IRS). The solid line is the sum of the TLF and IRS components.

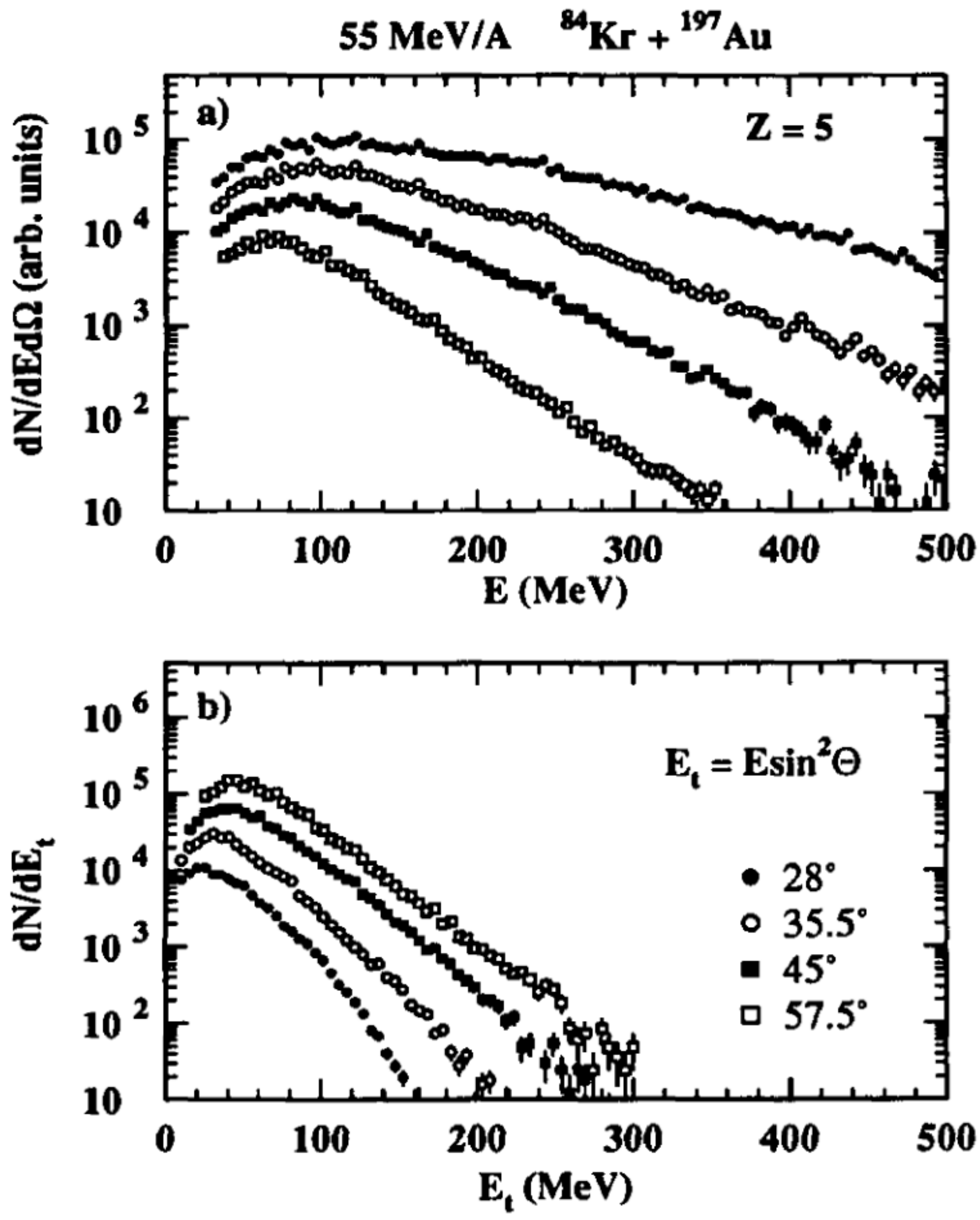

Figure 4.24. (a) Kinetic energy spectra of boron fragments emitted in central collisions of the reaction ^{84}Kr + ^{197}Au at E/A = 55 MeV. (b) Transverse kinetic energy spectra constructed from the spectra shown in (a).

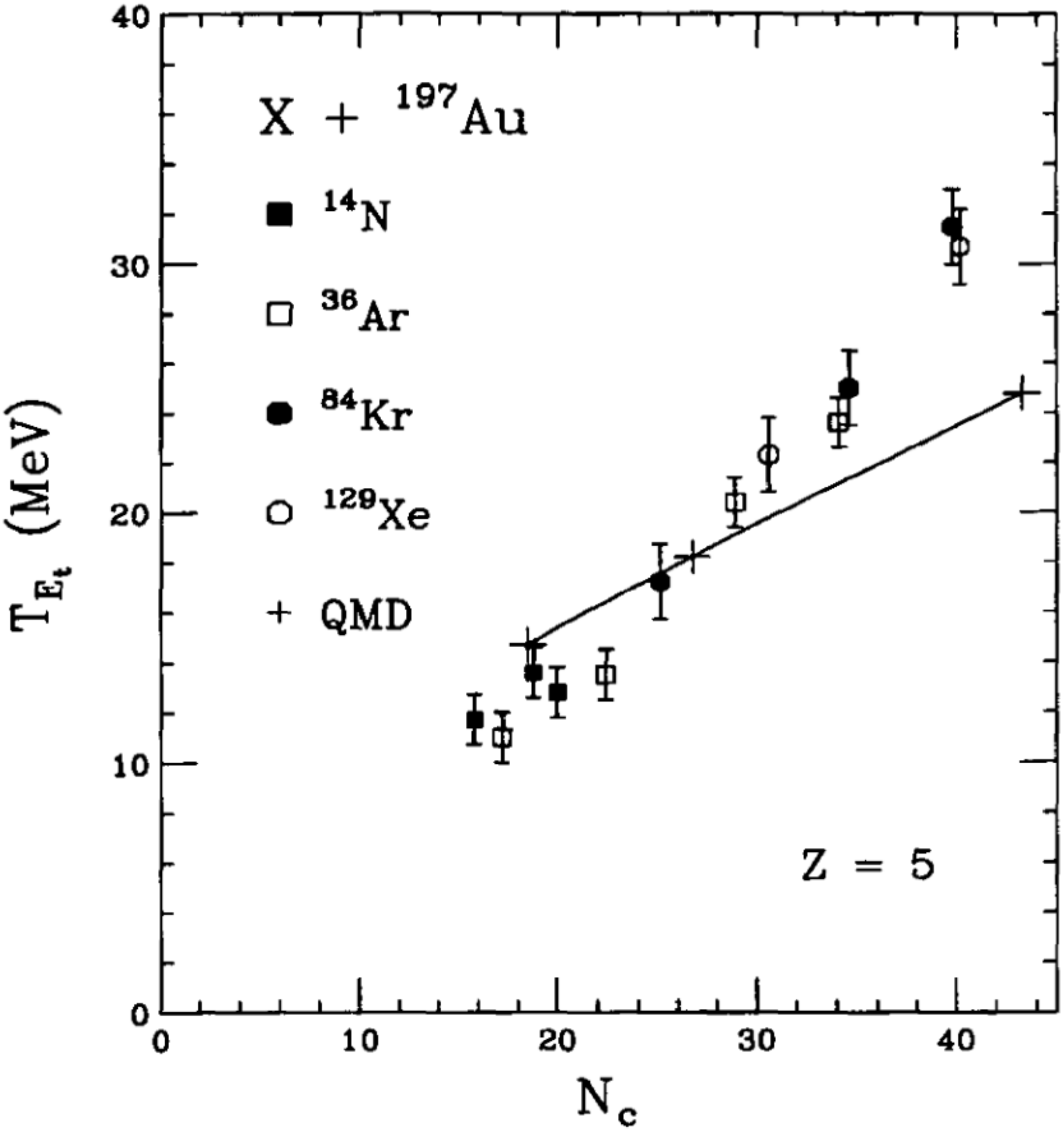

Figure 4.25. Extracted slopes from the transverse kinetic energy distributions for boron fragments emitted in central collisions. The beam energies represented for each system are described in the text.

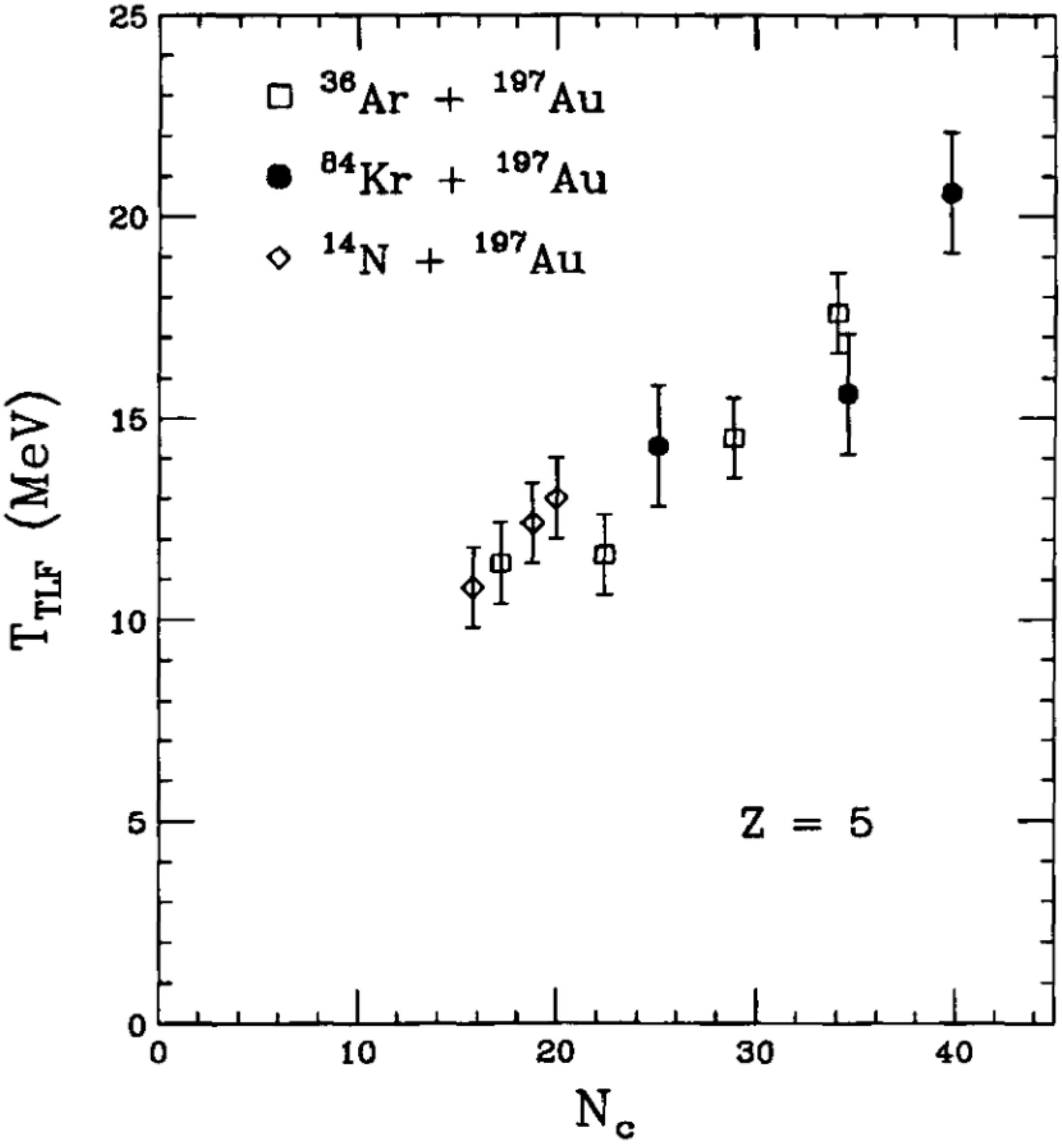

Figure 4.26. Slope parameters of the target-like source from moving-source fits of boron kinetic energy spectra. The beam energies represented for each system and the QMD calculations are described in the text.

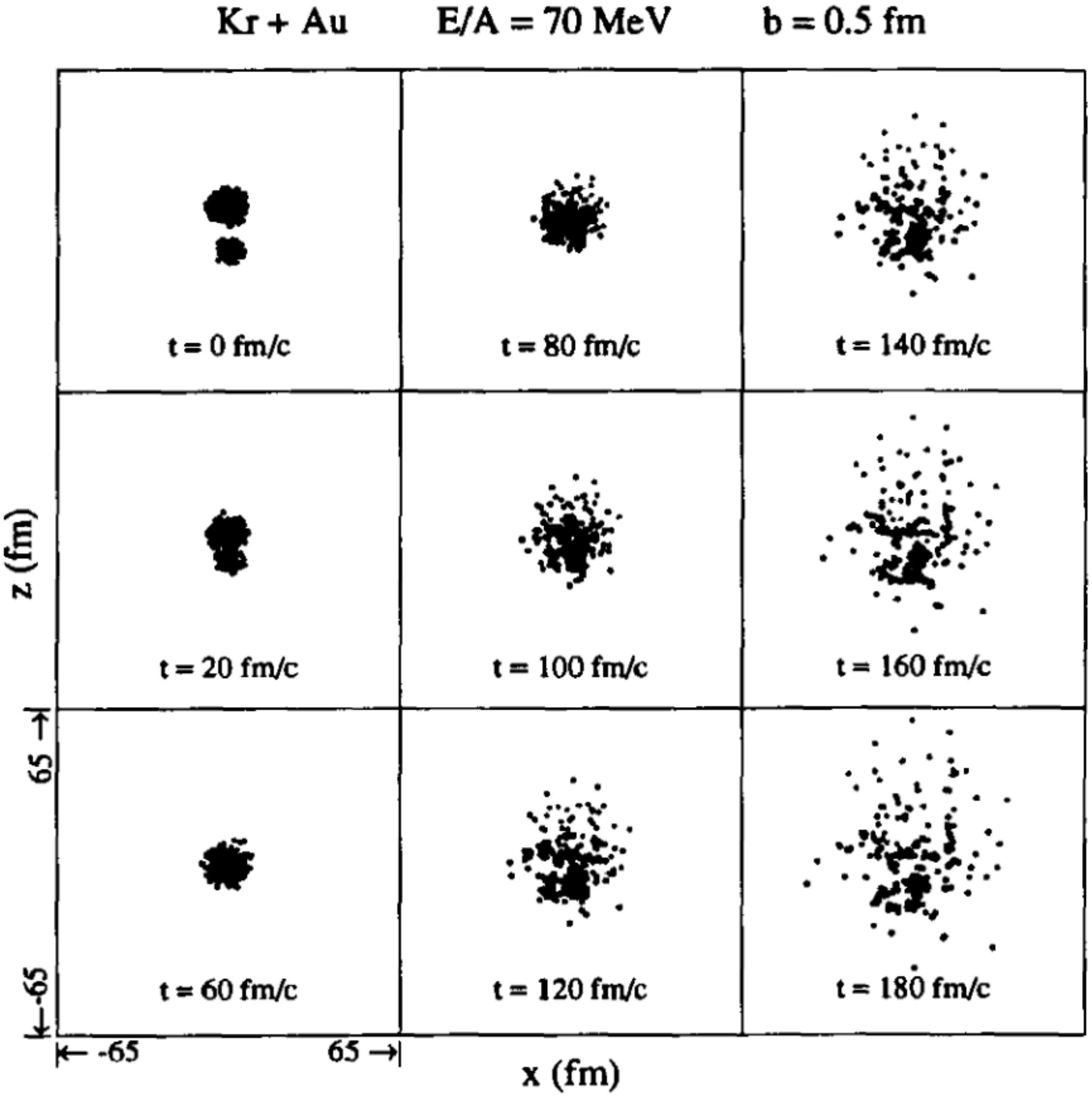

Figure 4.27. Simulation of a central collision (impact parameter = 0.5 fm) in the reaction ^{84}Kr + ^{197}Au at E/A = 70 MeV using the Quantum Molecular Dynamics (QMD) model for the different timesteps indicated in the figure. The ^{84}Kr projectile nucleons are represented as solid circles; the ^{197}Au target nucleons are represented as open circles.

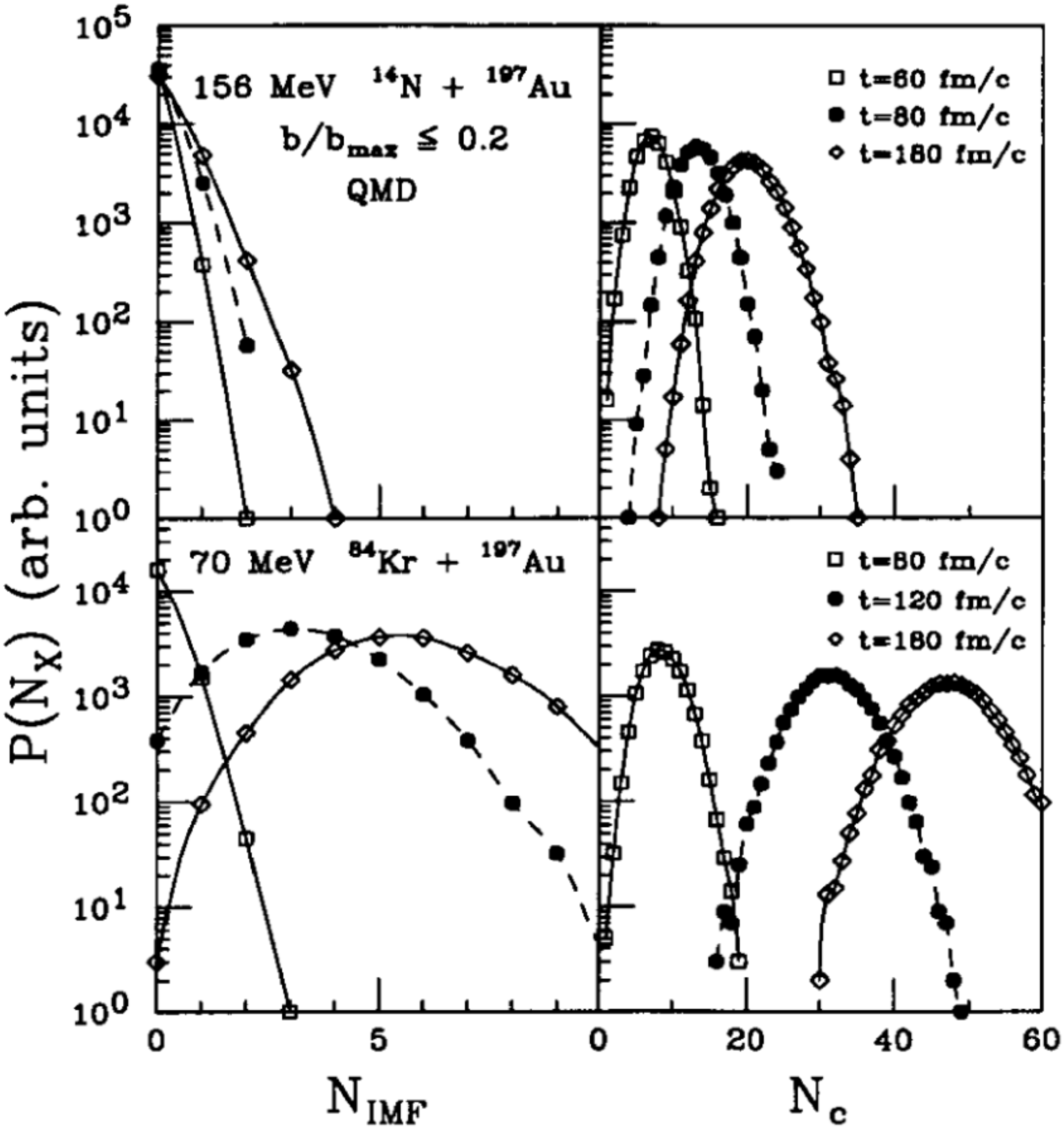

Figure 4.28. Intermediate-mass-fragment and charged-particle multiplicities from QMD simulations of central collisions in the reactions ^{14}N + ^{197}Au at E/A = 156 MeV (top panels) and ^{84}Kr + ^{197}Au at E/A = 70 MeV (bottom panels).

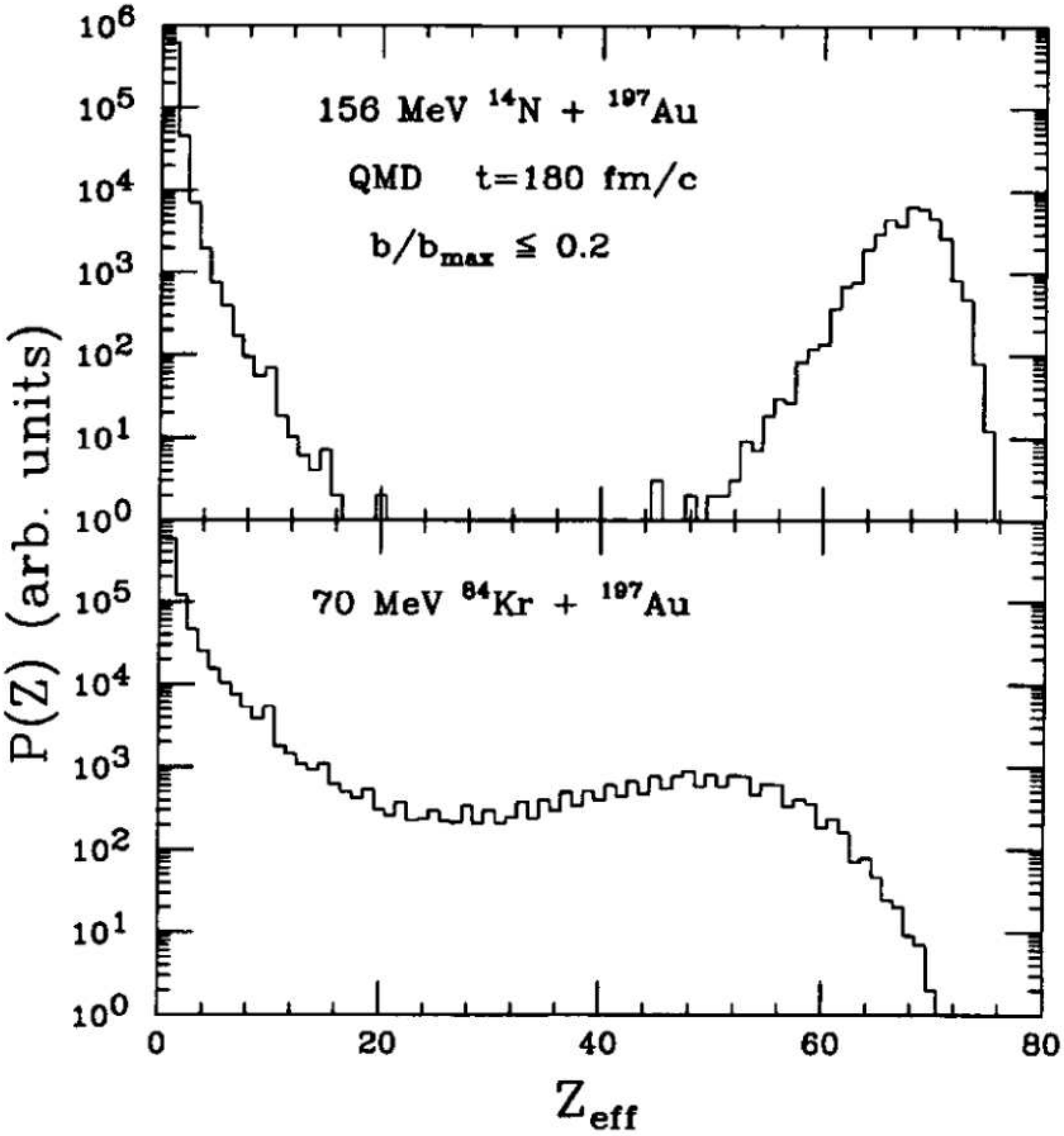

Figure 4.29. Effective charge distributions from QMD simulations of central collisions in the reactions ^{14}N + ^{197}Au at E/A = 156 MeV (top panel) and ^{84}Kr + ^{197}Au at E/A = 70 MeV (bottom panel).

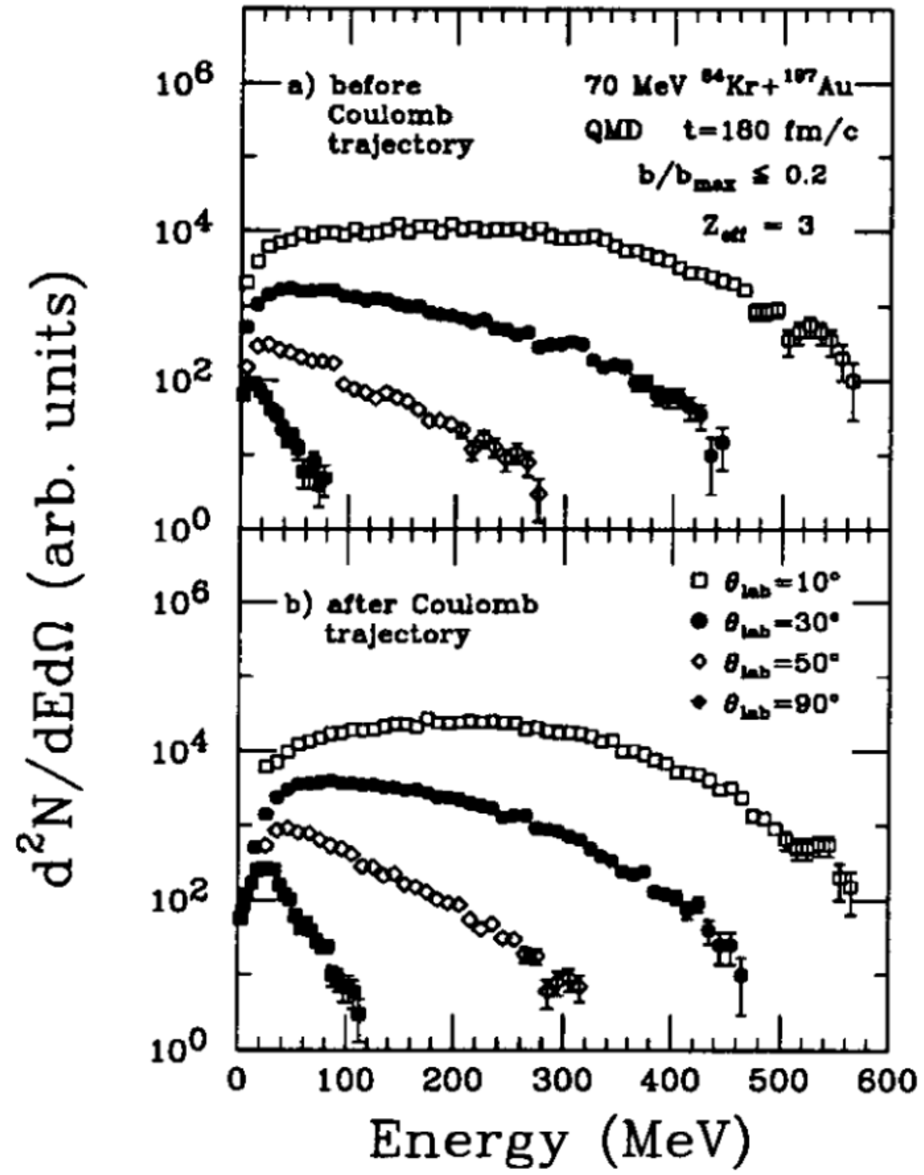

Figure 4.30. Kinetic energy spectra of $Z_{eff}=3$ fragments from QMD simulations of central collisions in the reaction ^{84}Kr + ^{197}Au at E/A = 70 MeV. The spectra are shown before (panel (a)) and after (panel (b)) the n-body Coulomb trajectory calculation (see text).

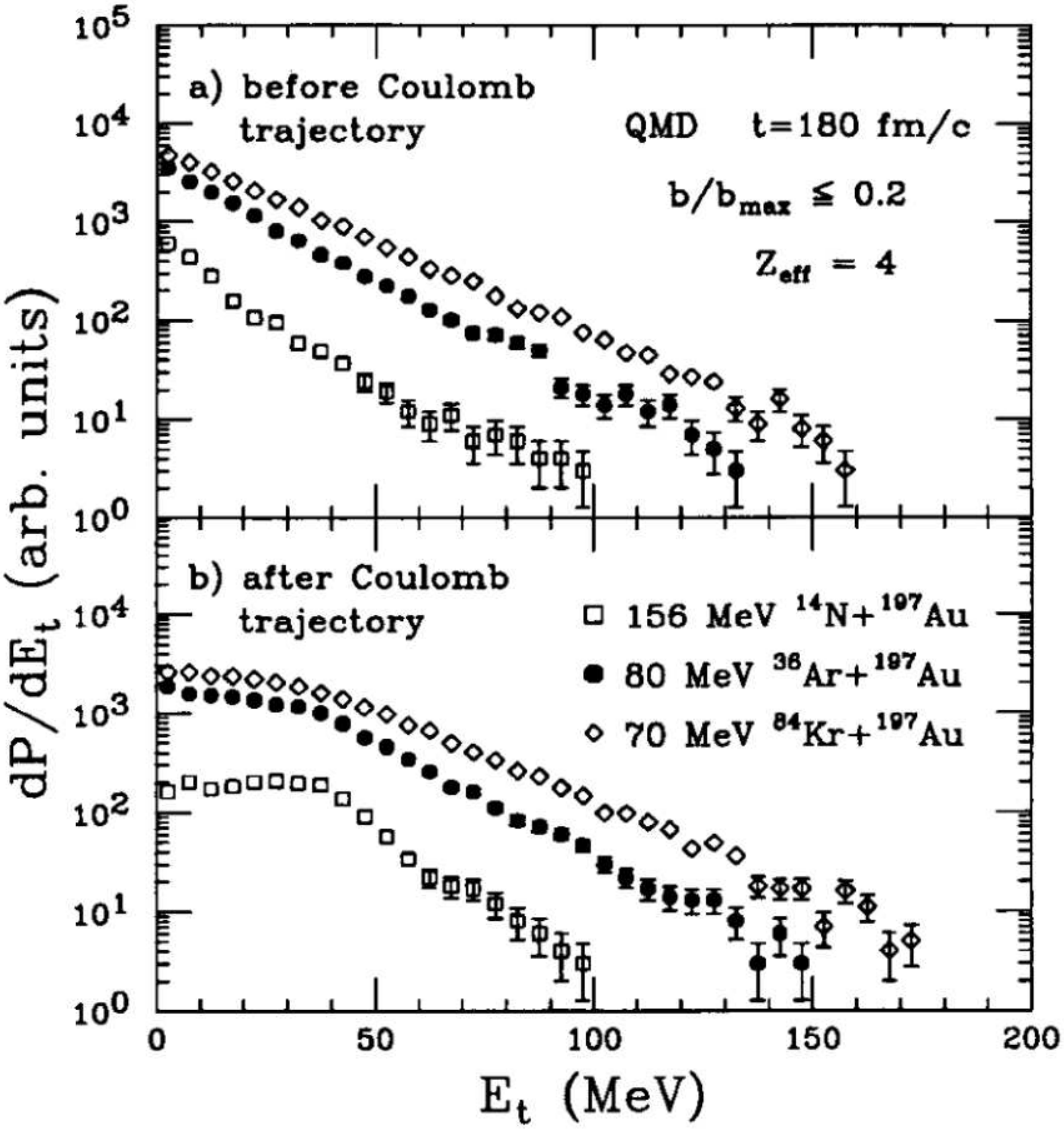

Figure 4.31. Transverse kinetic energy spectra of Z_{eff}=4 fragments from QMD simulations of central collisions in the reactions $^{14}N + ^{197}Au$ at E/A = 156 MeV (open squares), $^{36}Ar + ^{197}Au$ at E/A = 80 MeV (closed circles), and $^{84}Kr + ^{197}Au$ at E/A = 70 MeV (open diamonds). The spectra are shown before (panel (a)) and after (panel (b)) the n-body Coulomb trajectory calculation (see text).

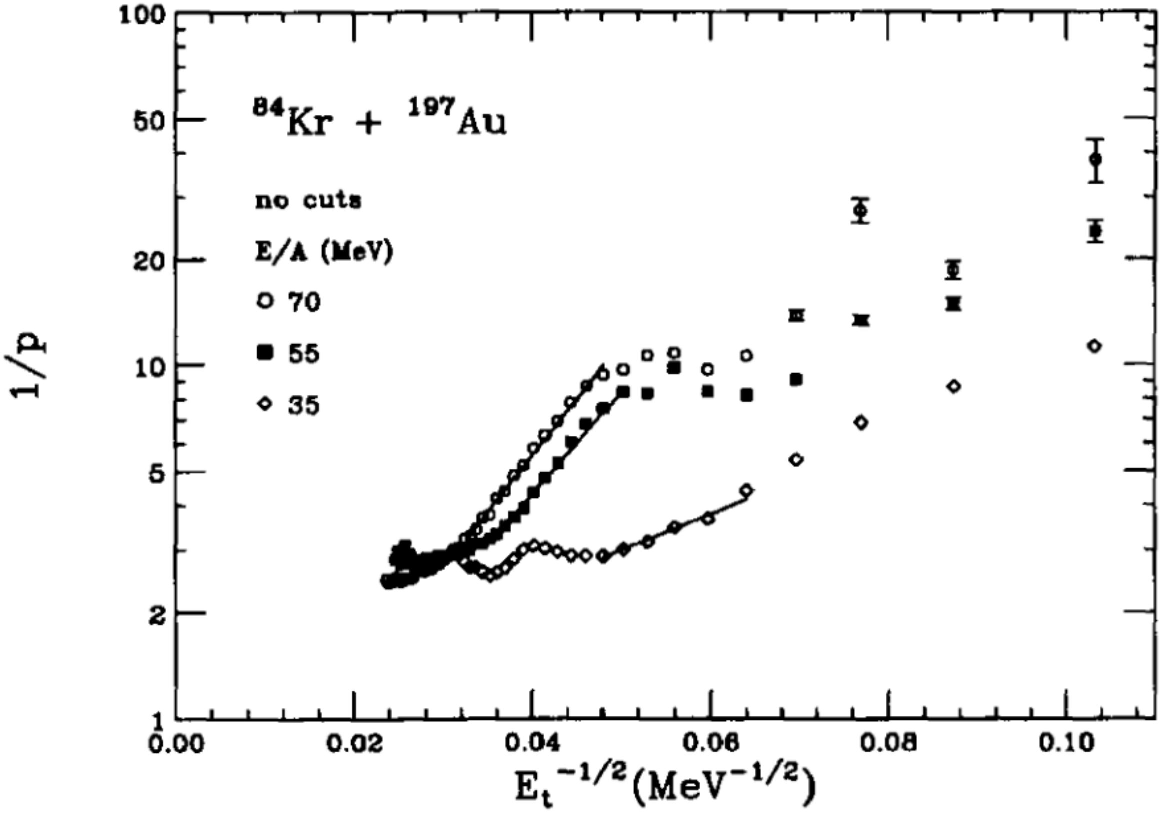

Figure 4.32. The reciprocal of the binary decay probability 1/p (calculated from the mean and variance of the IMF distributions) as a function of $E_t^{-1/2}$ for the reaction ^{84}Kr + ^{197}Au at E/A = 35 (open diamonds), 55 (closed squares) and 70 MeV (open circles).

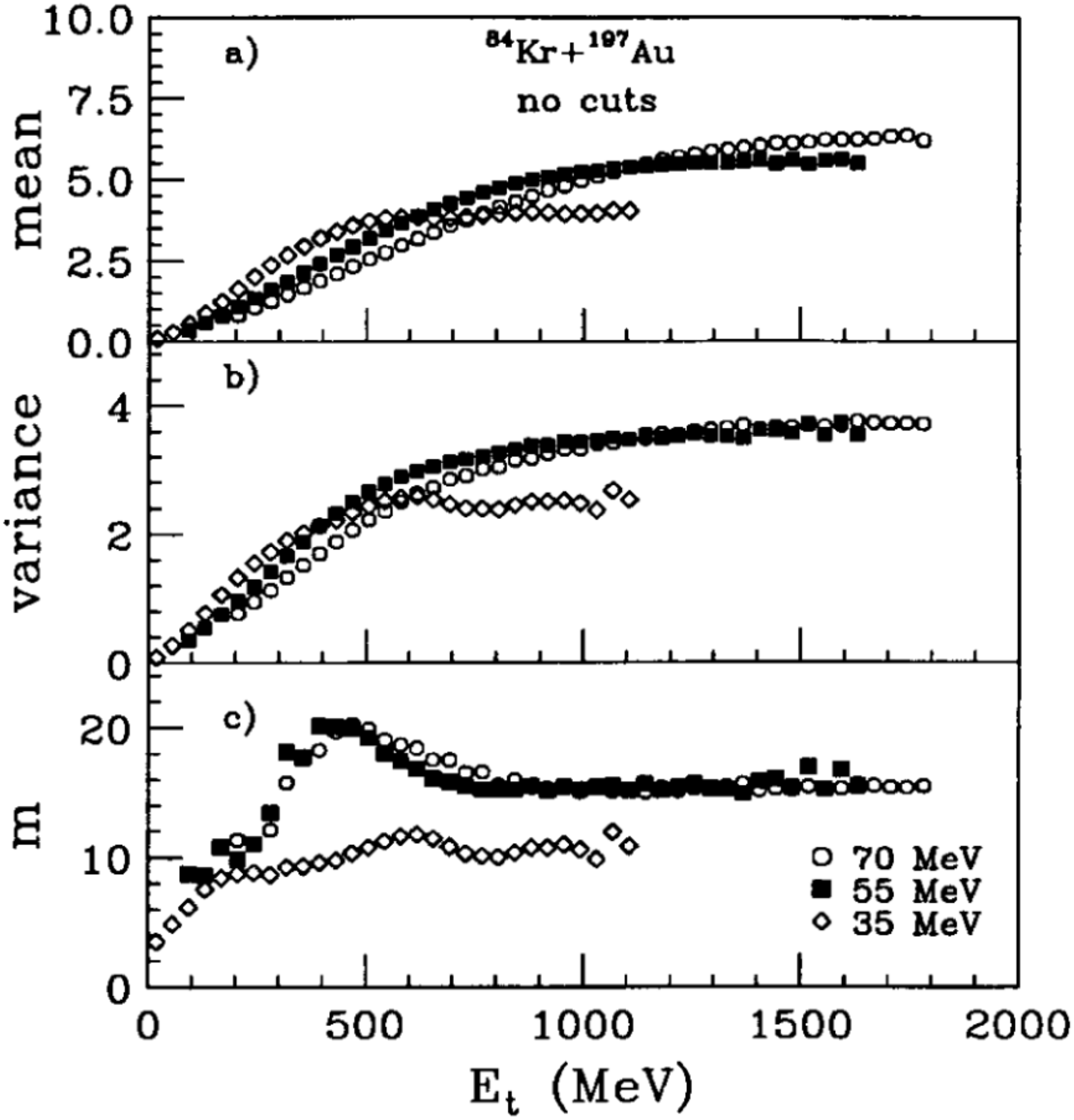

Figure 4.33. Dependence of the mean and variance of the IMF distribution, and the number of "tries" on the total transverse energy for the reaction ^{84}Kr + ^{197}Au at E/A = 35 (open diamonds), 55 (closed squares) and 70 MeV (open circles).

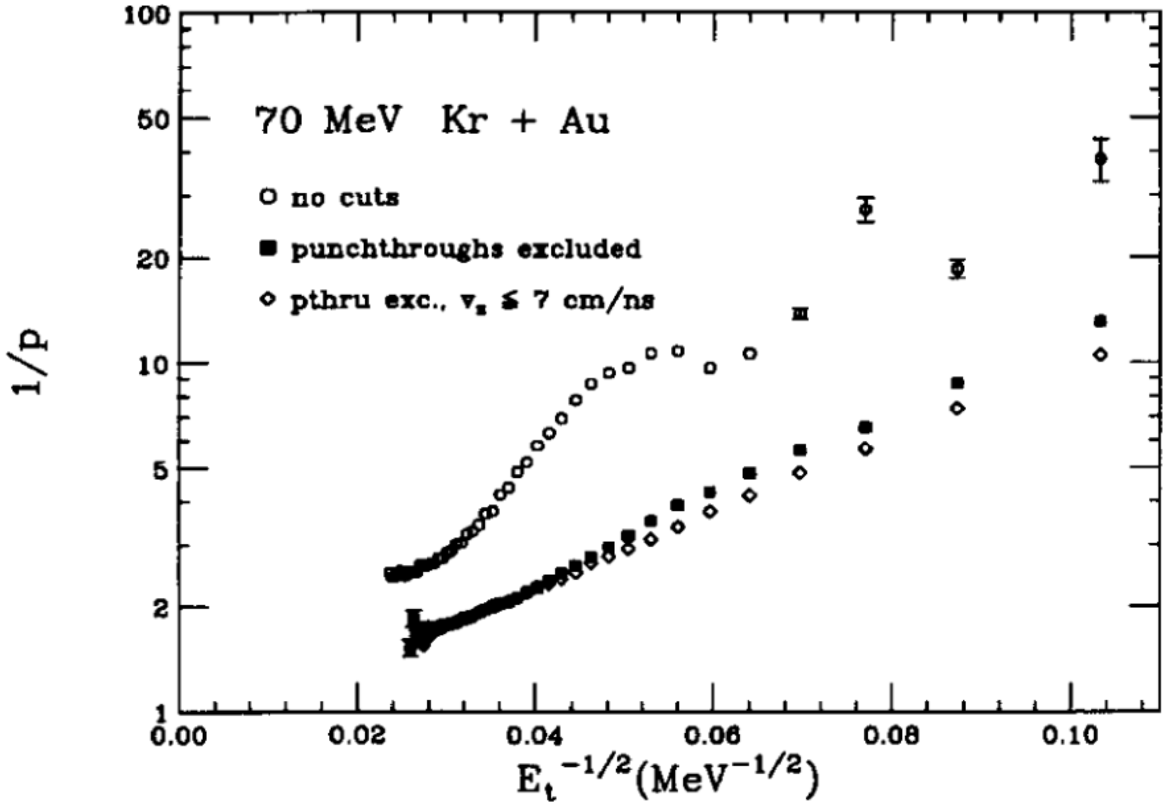

Figure 4.34. The reciprocal of the binary decay probability 1/p as a function of $E_t^{-1/2}$ for the reaction ^{84}Kr + ^{197}Au at E/A = 70 MeV. The different restrictions are described in the text.

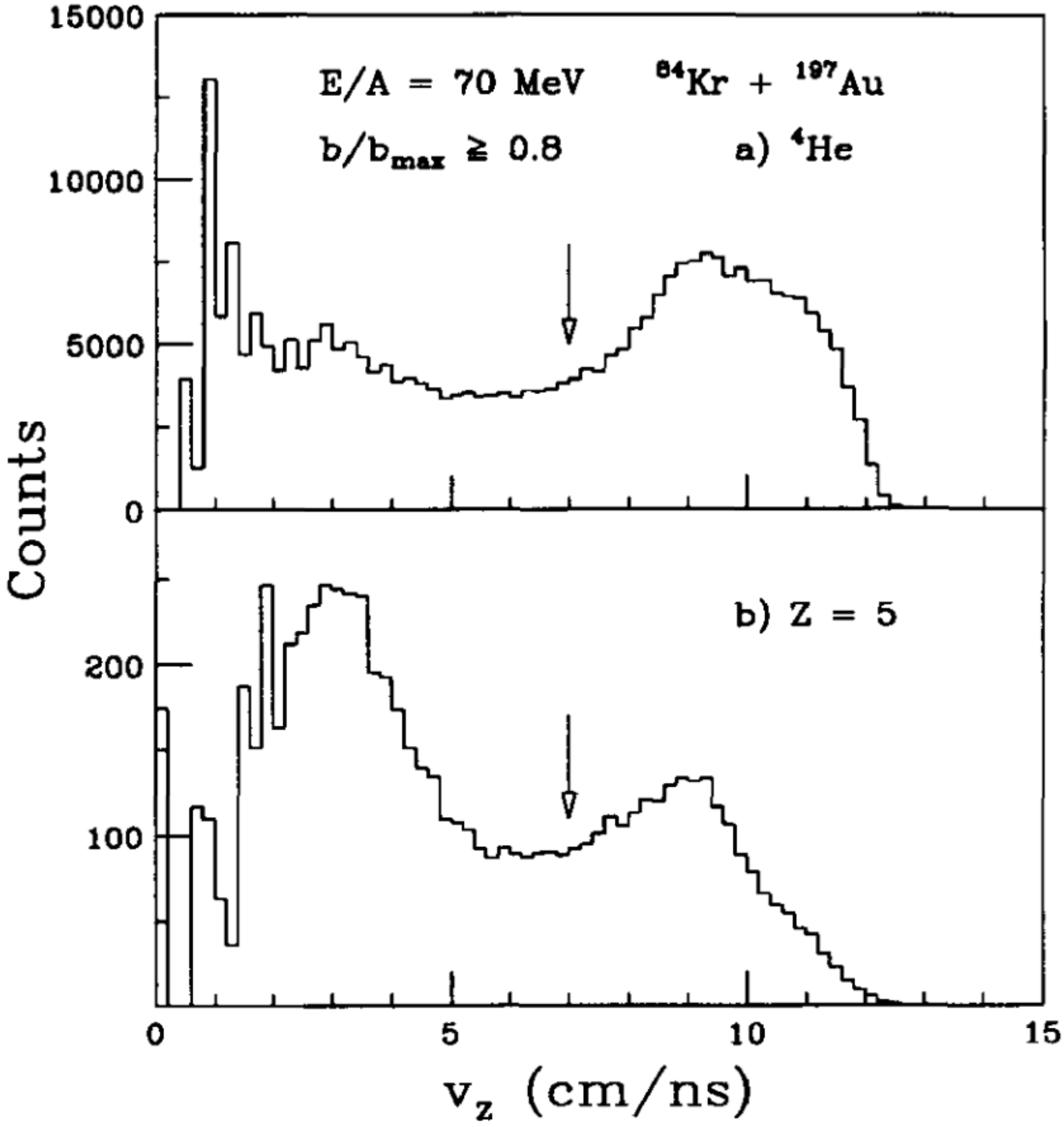

Figure 4.35. Longitudinal velocity distributions for alpha particles (top panel) and boron fragments (bottom panel) emitted in peripheral collisions ($b/b_{max} \geq 0.8$) of the reaction ^{84}Kr + ^{197}Au at E/A = 70 MeV. The arrows are described in the text.

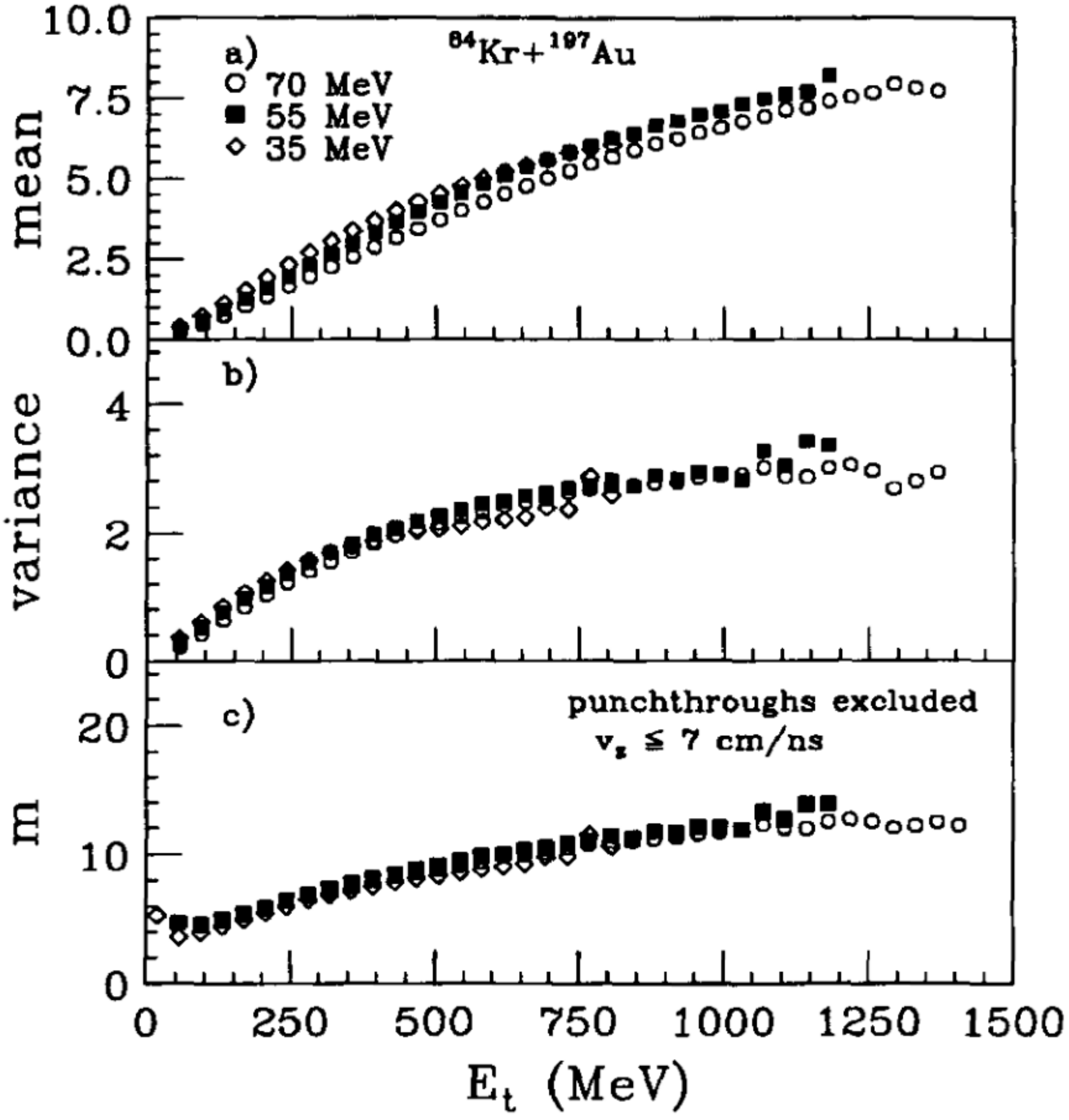

Figure 4.36. The same as in Figure 4.28 after eliminating punchthrough and high v_z particles (see text).

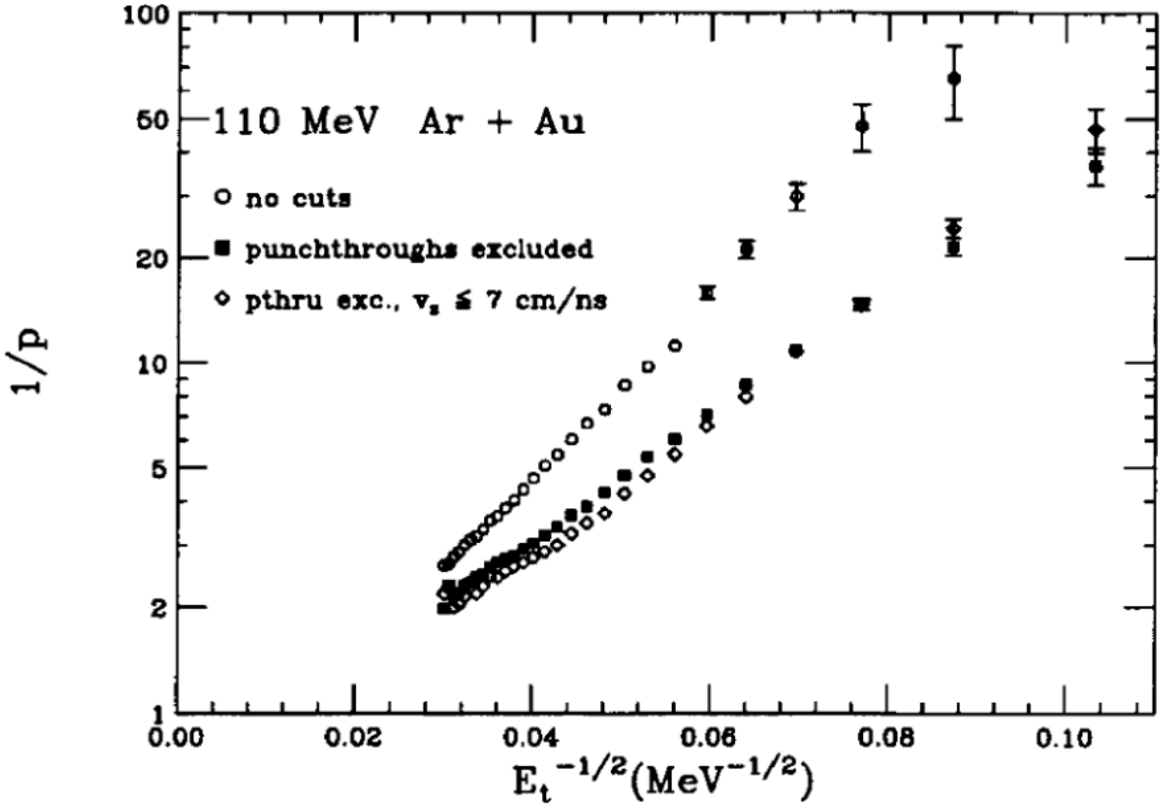

Figure 4.37. The reciprocal of the binary decay probability 1/p as a function of $E_t^{-1/2}$ for the reaction ^{36}Ar + ^{197}Au at E/A = 110 MeV. The different restrictions are described in the text.

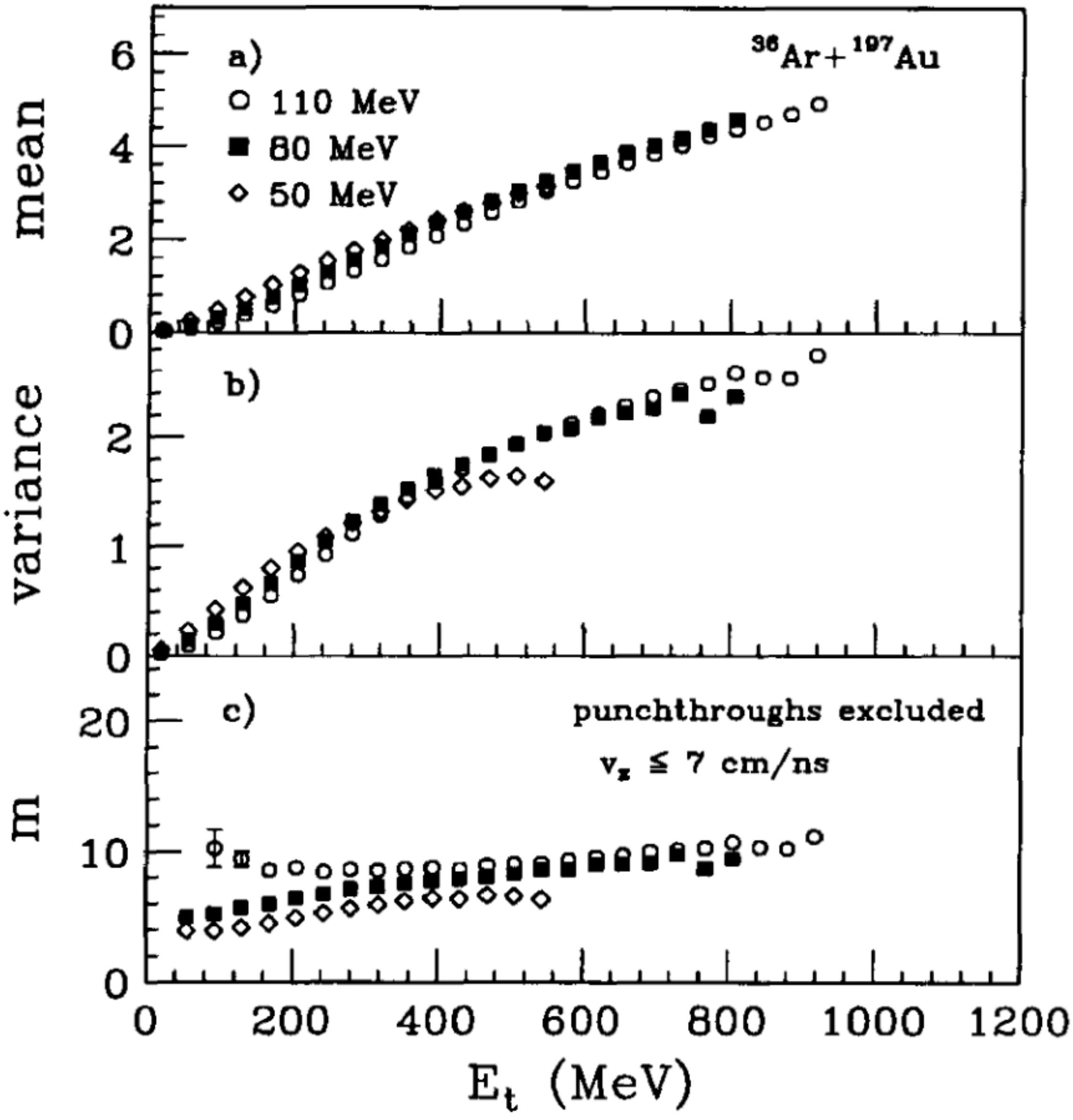

Figure 4.38. Dependence of the mean and variance of the IMF distribution, and the number of "tries" on the total transverse energy for the reaction ^{36}Ar + ^{197}Au at E/A = 50 (open diamonds), 80 (closed squares) and 110 MeV (open circles). Punchthrough and high v_z particles have been eliminated (see text).

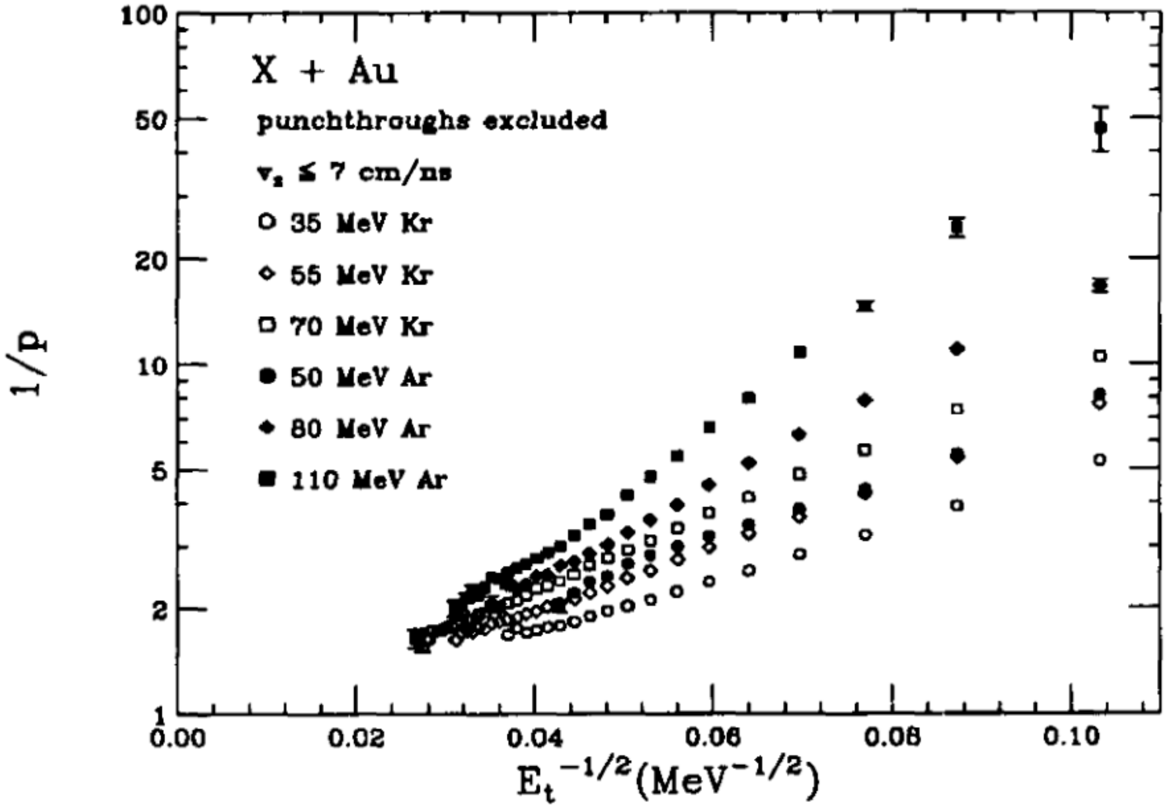

Figure 4.39. The reciprocal of the binary decay probability 1/p as a function of $E_t^{-1/2}$ for the reactions ^{84}Kr + ^{197}Au at E/A = 35, 55, and 70 MeV and reactions ^{36}Ar + ^{197}Au at E/A = 50, 80, and 110 MeV. Punchthrough and high v_z particles have been eliminated (see text).

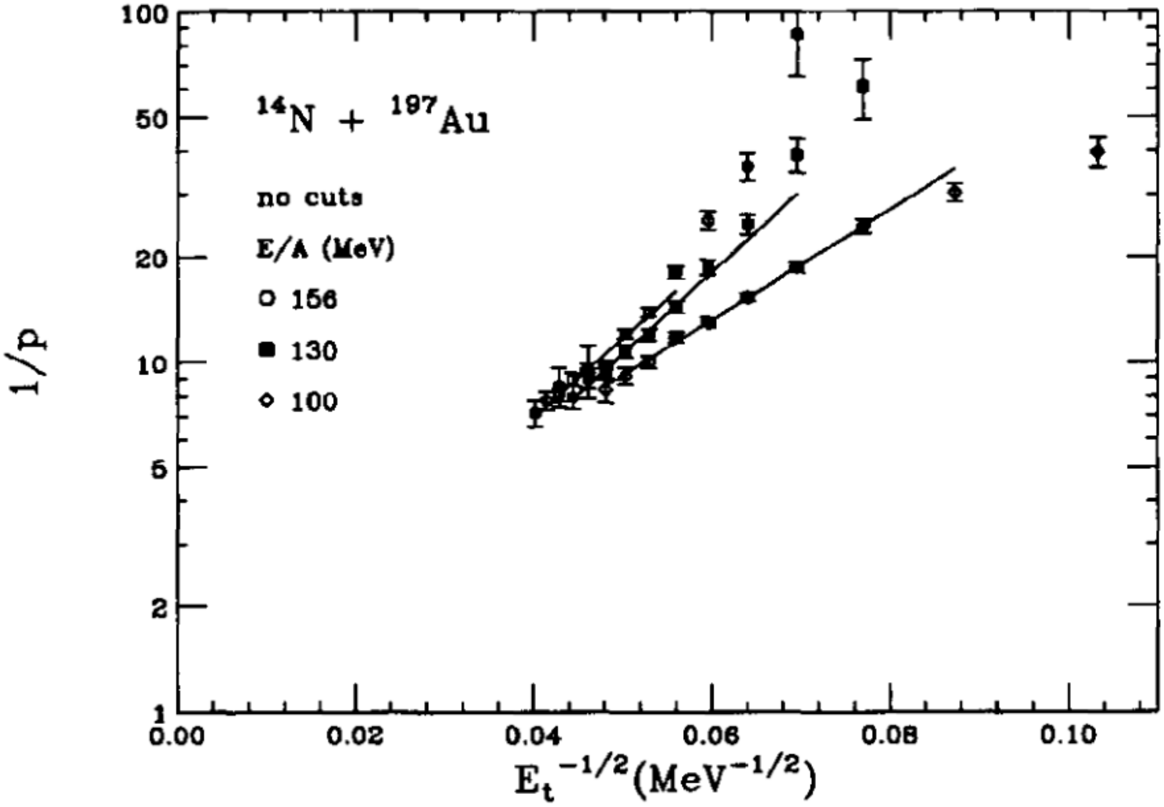

Figure 4.40. The reciprocal of the binary decay probability 1/p (calculated from the mean and variance of the IMF distributions) as a function of $E_t^{-1/2}$ for the reaction ^{14}N + ^{197}Au at E/A = 100 (open diamonds), 130 (closed squares) and 156 MeV (open circles).

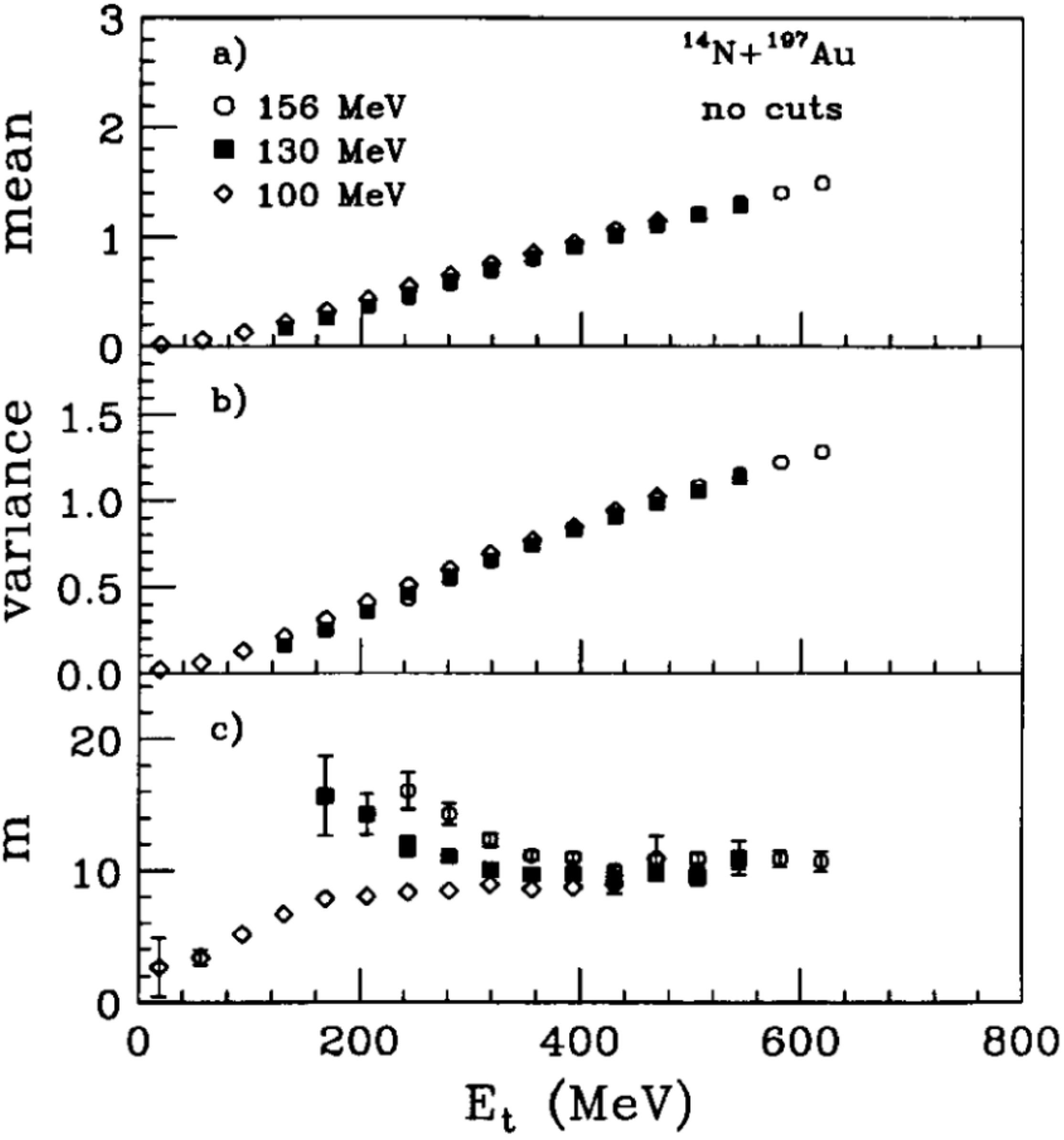

Figure 4.41. Dependence of the mean and variance of the IMF distribution, and the number of "tries" on the total transverse energy for the reaction $^{14}N + ^{197}Au$ at E/A = 100 (open diamonds), 130 (closed squares) and 156 MeV (open circles).

CHAPTER 5

ASSESSING THE EVOLUTIONARY NATURE OF MULTIFRAGMENT DECAY

A crucial question in the study of multifragmenting systems is whether the intermediate-mass nuclear fragments (*IMFs* :$3 \leq Z \leq 20$) are produced at a single time from a well defined (freeze-out) condition, or whether they are produced over a period of time as the system evolves and changes [1–6]. Inclusive observables provide little information about changes in source characteristics as the system de-excites. The exclusive measurements of the system ^{84}Kr + ^{197}Au can be used to gain insight into the time scale over which the fragments are emitted. In this analysis, our attention is specifically directed at the question posed above, i.e., whether the fragments arise from a single condition, or during the evolution of the system.

A. Velocity Correlation Functions

Our central question can be addressed by relating more exclusive observables to specific portions of the one-body energy spectrum. At a given angle these spectra are smooth, relatively featureless distributions which can be described by simple Boltzmann-like functions involving a single temperature, Coulomb barrier, and source velocity, and in some cases collective expansion energy. Typical spectra are shown in Figure 5.1. In particular, we have examined the fragment-fragment velocity correlations for different portions of the one-body velocity distribution. If the multifragmentation process were to involve a sharp freeze-out, then one would expect little dependence of these fragment correlations on different portions of the energy spectrum. On the other hand, if the yield were to arise during the evolution of the system, then different components of the spectra may arise from different conditions which could in turn provide different fragment-fragment correlation signals.

Fragment-fragment velocity correlations are a powerful tool for extracting information about the spatial-temporal dimensions of the emitting source [7–15]. This technique utilizes the mutual Coulomb repulsion of the fragments as a probe of the emitting system. The Coulomb repulsion results in a reduction of the probability for observing fragments at low relative velocity. Velocity correlation functions, $R(v_{red})$, were constructed, using procedures previously employed [10], by relating the coincidence yield Y_{12} to the product of the single particle yields Y_1 and Y_2:

$$\sum Y_{12}(v_1, v_2) = C[1 + R(v_{red})] \sum Y_1(v_1) Y_2(v_2), \qquad (1)$$

where v_1 and v_2 are the laboratory velocities of the fragments, the reduced velocity, $v_{red} = (v_1 - v_2)/(Z_1 + Z_2)^{1/2}$ [9], and C is a normalization constant determined by the requirement that $R(v_{red}) \rightarrow 0$ at large relative velocities where the Coulomb repulsion is small. The single particle yields were constructed by selecting fragments from different events which satisfy the same constraints as the coincidence yield. The use of v_{red} allows summation over different charge combinations [9].

In order to select preferentially events from a single equilibrated source, we select on central collisions. We have related the charged-particle multiplicity to an impact parameter scale following a geometrical prescription [16] and selected events which correspond to $b/b_{max} \leq 0.2$. In our definition, b_{max} refers to the maximum interaction radius for which two charged particles are emitted. For the central collisions selected, the azimuthal distributions are relatively flat indicating minimal distortions on the correlation function due to collective effects observed at higher incident energies [2].

As Figure 5.2(a-c) clearly indicates, the fragment-fragment correlation functions depend strongly on the kinetic energy of the fragment pairs. For each of the correlation functions shown, the fragments were selected on the basis of v_{min}, the minimum velocity of the less energetic fragment of each pair. All the correlation functions shown were summed over all pairs $4 \leq Z_1, Z_2 \leq 9$ emitted in the angular range $25^\circ \leq \theta_{lab} \leq 50^\circ$. The normalization constant for each correlation function was determined in the range $0.05\ c \leq v_{red} \leq 0.08\ c$. For orientation, the kinetic energies which correspond to these minimum velocities are depicted as the arrows on the energy spectra in Figure 5.1. For the E/A=35 MeV data the v_{min}=5 cm/ns correlation function was not shown because for this cut the correlation function at large v_{red} is not flat. This behavior could be due to dynamical effects (eg. resonance decays, collective motion, etc.). All of the correlation functions exhibit a "Coulomb hole", a strong suppression of pairs of low relative velocity. As the minimum velocity of the pair is increased, a significant increase in the width of the Coulomb hole is observed at all three incident energies. To quantify this effect sufficiently to pursue qualitative observations, we have extracted the width of the Coulomb hole in the correlation function at half its asymptotic value (HWHM) for each cut of fragment energy. In Figure 5.3(a), the values of the widths of the Coulomb holes are plotted against the velocity cut-off (minimum velocity) used to construct the correlation function. An increase in the HWHM with increasing v_{min} is clearly evident. For the v_{min} cuts shown, the correlation functions are affected by negligible dynamical effects. The representative error bars shown take into account the energy resolution. Selection of the same center-of-mass angle for each of the v_{min} cuts shown results in essentially the same trend observed in Figure 5.3(a).

We next consider the possible implications of this trend. The shape of the correlation function is associated with the space-time structure of the fragment emission process. In general, the wider the Coulomb hole the smaller the separation in space-time between the emission of contributing fragments pairs. Thus, the dependence of the strength of the Coulomb interaction suggests that different space-time situations are associated with the emission related to different parts of the spectra. Specifically, the higher energy fragments are emitted with smaller space-time separation between fragments. This result is a clear indication of an evolutionary process.

In earlier studies of proton-proton correlations [17], similar investigations found that different effective source sizes for proton emission were associated with different proton momenta. This trend was interpreted as due to contributions to the one-body energy distribution from protons originating both from an early dynamical stage, as well as, a late evaporative stage. This temporal behavior for proton emission is not surprising however, since proton emission does not require attainment of a low density phase.

B. Model Comparisons

To examine further the general trends observed in the correlation functions, we have performed 3-body Coulomb trajectory calculations in which we assume fragment emission from the surface of a source of fixed initial size. The source was assumed to be a nucleus with $Z = 40, A = 92$ and a radius of 7 fm [18]. The distribution function for the time between emissions was assumed to have the form $\exp(-t/\tau)$ which is characterized by a single time constant, τ. Correlations functions, characterized by v_{min}, were constructed from the 3-body Coulomb trajectory calculations. The observed inclusive correlation function, at 55 MeV/A, is well described by the decay of a R = 7 fm source with a characteristic emission time of $\tau = 100$ fm/c. Within the context of our 3-body model, the dependence of the width of the Coulomb hole on the minimum velocity for different values of τ is shown as solid lines in Figure 5.3(a).

While the reference 3-body calculations for a given size and decay rate show a dependence of the predicted widths on velocity cut-off, the trend is opposite the trend observed in the data; namely, one finds a decrease in width with increasing minimum velocity. This decrease may simply be associated with an increase in the initial spatial separation of the members of the pair due to the increasing velocity of the first emitted fragment. If one were to assume that variation in time separation is more significant than the variation in spatial separation, and if one makes some reasonable assumption of source size, then each observed hole width can be associated with a given emission time constant through comparison with the 3-body calculations. This procedure has been used to obtain the points displayed in Figure 5.3(b), which relate mean emission times to the minimum velocity cut-offs in the spectra. The two different sets of points arise from the use of two different values for the source radius in the reference trajectory calculations.

We have examined the predicted relationship between emission rates and spectral velocities for two specific models of multifragmentation, the first, representative of the *freeze-out* scenario (where all fragments are formed at a single time), and the second, based on an *evolutionary* scenario (where the system changes as the fragments are emitted).

For the first model we have examined the Berlin microcanonical statistical model (McFrag) [19]. This model has previously been used to investigate the inclusive correlation function [20], but it fails to reproduce the fragment kinetic energy spectra, providing a very narrow range of fragment velocities. The source was assumed to have $Z = 79, A = 197$ with an excitation energy of 2400 MeV and a freeze-out radius of $\approx$13 fm. These parameters roughly reproduce the experimentally measured IMF and charged-particle multiplicities at E/A = 55 MeV [13]. The dependence of the correlation function on the fragment velocity predicted by the McFrag model is shown in Figure 5.2(d). The velocity cut-offs, differing from those in Figure 5.2(a-c), were scaled (based on the fraction of the velocity distribution) to the limited range of the spectra provided by the model. Since all the fragments are emitted simultaneously, the only dependence of the correlation function on final spectral velocity comes from the sampling of different initial spatial configurations of the final decay fragments.

This feature appears to provide the correlation functions only a weak dependence on the fragment kinetic energy.

For the second model we examined the predictions of the EES model [6] which explicitly incorporates emission during the evolution of the system. While this model predicts smooth singles fragment energy spectra, these spectra are composed of contributions arising from different times in the decay of the source. In this model, the source temperature changes with time due to adiabatic changes in density and particle emission. The Coulomb acceleration also changes with time. The portion of the spectra associated with each instant in time is provided by instantaneous properties. A schematic calculation was done for an initial source of A=197 and Z=79, with an initial temperature of 12 MeV. This calculation predicts an average multiplicity of about 4 IMFs. Due to the changing conditions, the mean separation times vary with the velocity of the fragments. The calculation shows a decreasing mean emission (separation) time with increasing fragment energy. This result can be understood as follows: The most energetic part of the spectra is populated for the highest temperatures and Coulomb energies. These conditions exist only early in the evolution of the system. At later times, fragments of these kinetic energies are rarely emitted. This confined "window" of opportunity for high energy fragments affects the mean separation time associated with their emission.

The model suggests that the mean separation time increases with decreasing fragment energy until the vicinity of the yield peak where it levels off. For the very lowest velocity fragments the separation times grows sharply. These fragments are predominately emitted under conditions of low temperature and low source charge, where the predicted emission process is slowest. An attempt has been made to compare the qualitative predictions of the EES model with the trends shown in Figure 5.3(b). The model was used to predict the relationship between mean emission times and fragment velocities in the source frame for pairs of ^{9}Be fragments. The velocities of fragments predicted in the model were then transformed from the center-of-mass to the laboratory using the experimentally determined center-of-mass velocity. These transformed results have been compared with the experimental data in Figure 5.3(b). The schematic model calculations do not reproduce the exact dependence of τ on v_{min}, indicating that the precise relationship between changes in the source properties and fragment emission dynamics is not yet fully understood. The calculations do, however, predict a trend which is very similar to that observed experimentally, indicating that changes in the source characteristics and fragment formation occur on commensurate time scales.

REFERENCES

[1] M. L. Gilkes et al. Phys. Rev. Lett. **73**, 1590 (1994).

[2] B. Kaempfer et al., Phys. Rev. C **48**, R955 (1993).

[3] L. G. Moretto et al. Phys. Rev. Lett. **74**, 1530 (1995).

[4] D.H.E. Gross et al., Phys. Rev. Lett. **56**, 1544 (1986).

[5] J. Bondorf et al., Nucl. Phys. **A444**, 460 (1985).

[6] W.A. Friedman Phys. Rev. C **42**, 667 (1990).

[7] R. Trockel et al., Phys. Rev. Lett. **59**, 2844 (1987).

[8] Y. D. Kim et al., Phys. Rev. Lett. **67**, 14 (1991).

[9] Y. D. Kim et al., Phys. Rev. C **45**, 338 (1992).

[10] D. Fox et al., Phys. Rev. C **47**, R421 (1993).

[11] E. Bauge et al., Phys. Rev. Lett. **70**, 3705 (1993).

[12] T. C. Sangster et al.,Phys. Rev. C **47**, R2457 (1993).

[13] D. Fox et al., Phys. Rev. C **50**, 2424 (1994).

[14] T. Glasmacher et al., Phys. Rev. C **50**, 952 (1994).

[15] R. Bougault et al., Phys. Lett. **B232**, 291 (1989).

[16] C. Cavata, et al., Phys. Rev. C **42**, 1760 (1990).

[17] W. G. Gong et al., Phys. Rev. C **43**, 1804 (1991).

[18] The values of source charge and radius chosen for the trajectory calculation are smaller than those used for the EES and McFrag model calculations since the trajectory calculation is a surface emission model without light charged particle emission between successive IMF emissions.

[19] X.Z.Zhang et al., Nucl. Phys. **A461**, 641 (1987);**A461**, 668 (1987).

[20] O. Schapiro et al., Nucl. Phys. **A568**, 333 (1994).

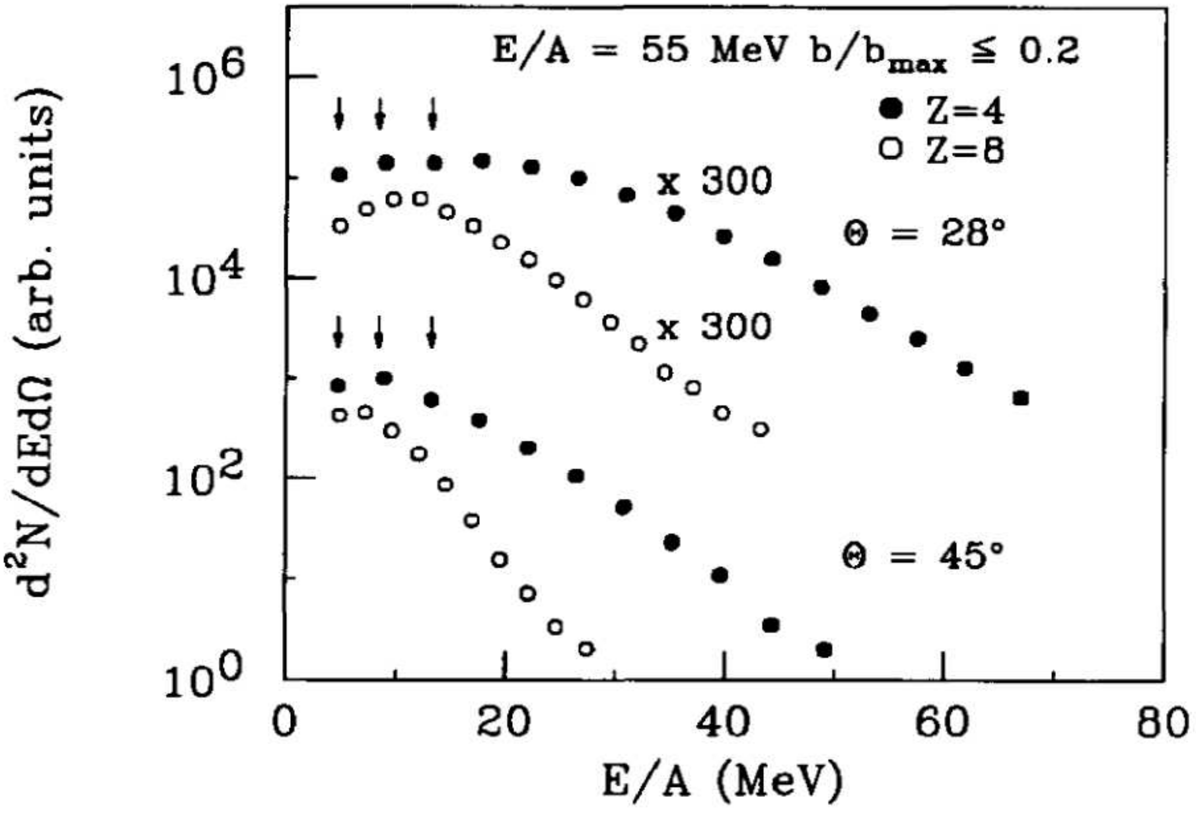

Figure 5.1. Inclusive kinetic energy spectra for Be and O fragments (closed and open symbols) emitted in central collisions. The arrows indicate velocity cuts of v_{min} = 3, 4, and 5 cm/ns.

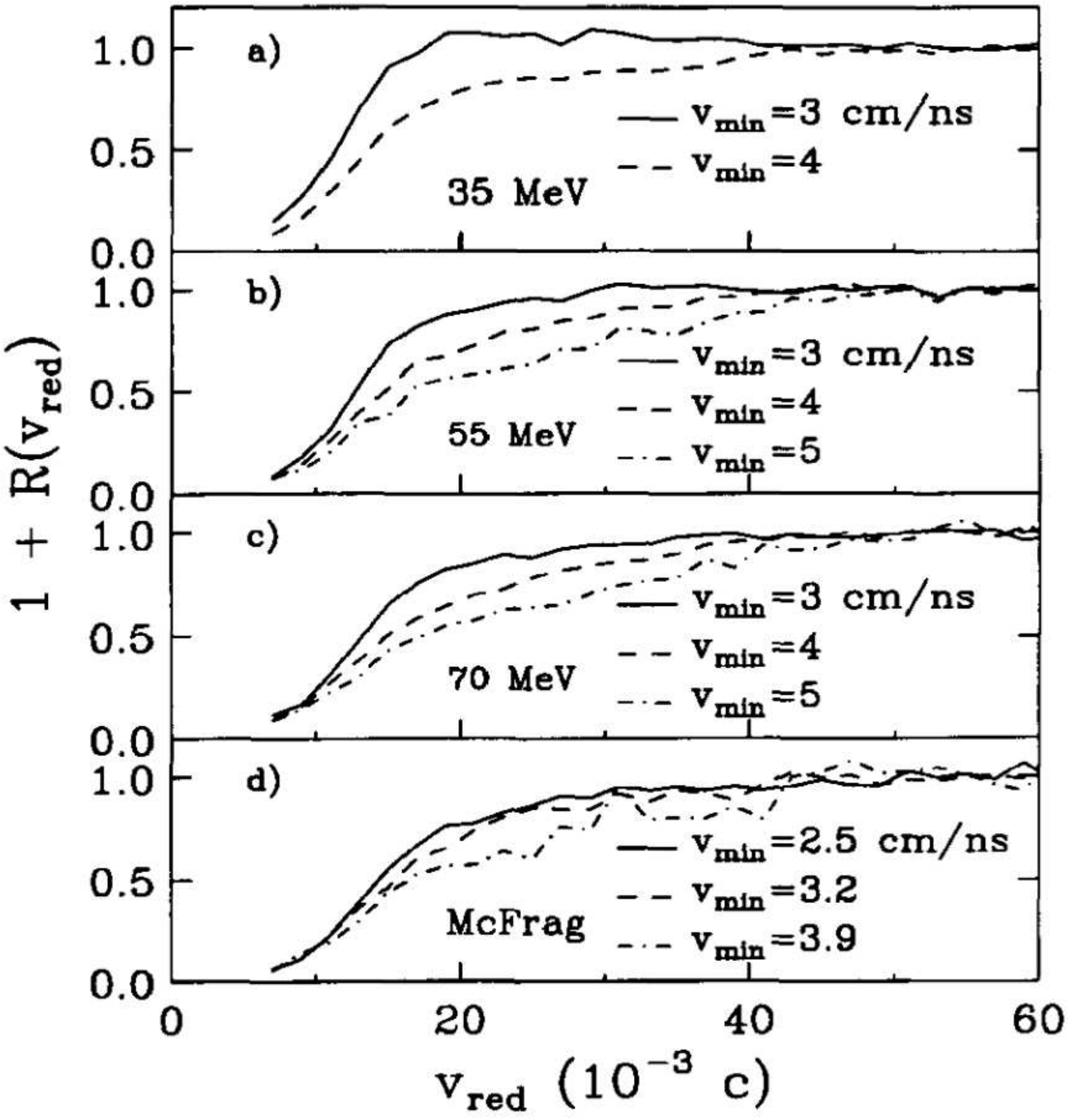

Figure 5.2. a-c) Experimental correlation functions at E/A = 35, 55, 70 MeV with different restrictions on v_{min}. d) Correlation functions constructed from the predictions of a microcanonical ensemble model for different restrictions on v_{min}.

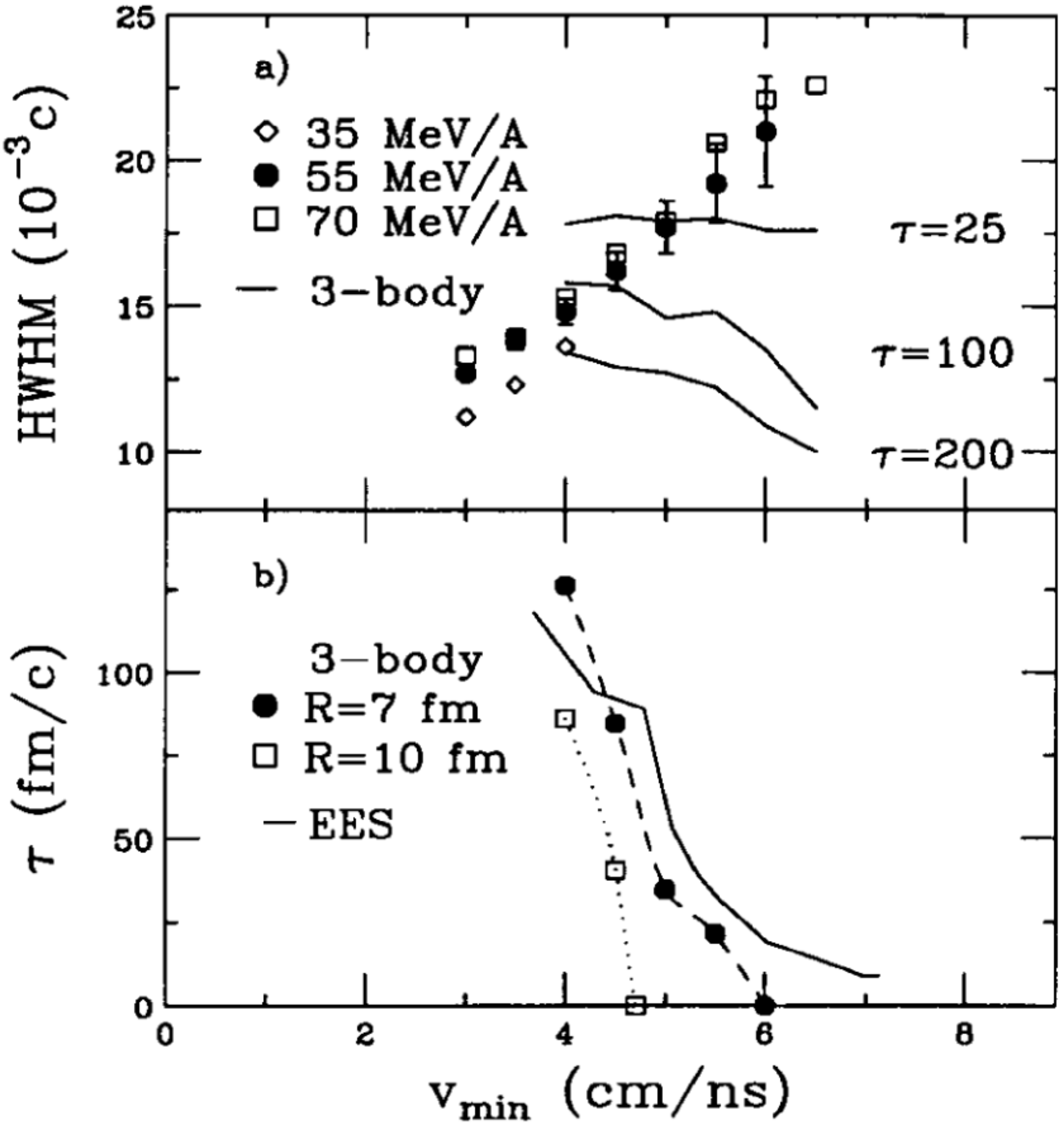

Figure 5.3. a) Dependence of the Coulomb interaction (HWHM) between fragments on the minimum fragment velocity. Diamonds, circles and squares represent the experimental data at E/A = 35, 55, and 70 MeV. Solid lines indicate the results of 3-body Coulomb trajectory calculations for τ = 25, 100, and 200 fm/c. b) Dependence of the extracted emission time on the minimum velocity of the fragment pair. The solid circles and open squares correspond to the experimental data at E/A = 55 MeV.

CHAPTER 6

CHANGING SOURCE CHARACTERISTICS DURING MULTIFRAGMENT DECAY

In Chapter 5, we investigated an association between the strength of the fragment-fragment Coulomb interaction and the kinetic energy of the fragment pair for IMFs emitted in central collisions of the reaction ^{84}Kr + ^{197}Au at E/A = 35, 55, and 70 MeV. Selection on fragment pairs of high velocity yielded a stronger fragment-fragment Coulomb interaction than for inclusive fragment pairs. This result is consistent with fragment emission from a source of decreased spatial-temporal extent and indicates that fragment emission occurs on a time scale commensurate with changes in the source characteristics. In the present chapter, the universality of this association (applicability to other systems) and the effect of different selection criteria are explored. The sensitivity of the spatial-temporal extent deduced by the correlation function technique to measurement uncertainties, assumed source characteristics, and rotational effects is assessed.

A. Impact Parameter Selection

In order to select preferentially the most highly excited systems where multifragment decay describes the average behavior of the system [1], we have focused on central collisions. We have constructed a reduced-impact parameter scale from the charged-particle multiplicity following a geometrical prescription [2]. The central collisions included in this analysis have impact parameters of $b/b_{max} \leq 0.2$, where b_{max} refers to the maximum interaction radius for which two charged particles are emitted. The corresponding charged-particle multiplicities for these central collisions are $N_c \geq$ 24, 33, and 38 and the average multiplicity of IMFs, $< N_{IMF} > \approx 4, 5, 6$ at E/A = 35, 55 and 70 MeV, respectively [1].

One characterizing observable of multifragmenting systems is the element distribution of emitted particles. In high energy ($80 \leq E_p \leq 350$ GeV) proton-induced reactions, Z distributions have been measured which obey a power law with $\tau = 2.6$ [3]. At considerably lower bombarding energies ($200 \leq E_{lab} \leq 3600$ MeV) for the ^{3}He + ^{nat}Ag system, power-law fits to the Z distributions reach a constant value of $\tau = 2.1$ at energies above 1800 MeV [4]. For heavy-ion reactions, where initial compression of the nuclear system might induce a liquid-gas phase transition, τ values of ≈ 2.2 have been measured for the ^{40}Ar + ^{197}Au system at E/A = 220 MeV [5]. All of the above measurements, however, represent inclusive measurements where the fragment emission is averaged over a wide range of impact parameters. In the present experiment, we have investigated the impact-parameter-selected character of Z distributions of fragments emitted in multifragmenting nuclear systems.

The change in the Z distributions of emitted particles with increasing charged-particle multiplicity can be seen in Figure 6.1. These distributions have been measured in the angular range $25° \leq \theta_{lab} \leq 50°$ using the low threshold ionization-chamber telescopes. We have fit the Z distributions for $3 \leq Z \leq 14$ with the functional form $P(Z) \propto Z^{-\tau}$. The dependence of the fit parameter, τ, on N_c at each of the different bombarding energies is plotted in Figure 6.1. The inset in this figure depicts the Z distributions measured for particles emitted in collisions of different impact parameters in the reaction ^{84}Kr + ^{197}Au at E/A = 55 MeV, along with the power-law fits (solid lines). The distributions become less steep as we select on more central collisions.

The observed decrease in τ with increasing multiplicity can be understood in terms of the correlation between multiplicity and deposited energy. Fragment emission is expected to increase as the temperature of the emitted system is raised and the Coulomb barrier effects are reduced [6]. The minimum τ achieved in central collisions increases from 1.2 at E/A = 35 MeV to 1.7 at E/A = 70 MeV. This increase in τ_{min} is qualitatively consistent either with a more excited system at E/A = 70 MeV fragmenting into smaller (on average) pieces or the increasing importance of sequential decay of excited primary fragments.

The details of the shape of the fragment kinetic energy spectra can provide useful information regarding the *excitation* and *density* of the emitting system [7]. The kinetic energy spectra for beryllium and carbon fragments emitted in central collisions in the reaction ^{84}Kr + ^{197}Au at E/A = 55 MeV are presented in Figure 6.2. The spectra have been measured in the angular range $40° \leq \theta_{lab} \leq 50°$ using the Miniball detector array. The spectral shapes shown agree with the energy spectra measured with the ion-chamber telescopes. At a given angle, these spectra can be represented as general Maxwell-Boltzmann distributions consisting of a single temperature, Coulomb barrier, and source velocity. However, the energy-angle distributions are not understandable in terms of the isotropic emission from a single equilibrium source because the angular distributions are anisotropic in any single rest frame.

The presence of multiple sources can clearly be seen in the velocity plots presented in Figure 6.3. Beryllium fragments emitted in peripheral (b/b_{max} = 0.6-0.8) and central ($b/b_{max} \leq 0.2$) collisions for E/A = 70 MeV are displayed in panels (a) and (b), respectively. The detector thresholds are indicated by the dashed lines. Peripheral interactions manifest a fragment velocity distribution with more than one component. The higher longitudinal velocity component is a broad distribution populating v_{par} between 4 and 11 cm/ns. This component might arise from projectile breakup reactions or emission from the excited projectile-like fragment following a dissipative binary collision. The second source of fragments in peripheral collisions is a target-like source with a velocity $v_{par} \approx 1$ cm/ns. For central collisions (panel (b)), the presence of two components is less obvious. It is clear that isotropic emission from a single equilibrated source of fixed velocity is inconsistent with the observed emission pattern. In order to minimize the effects of multiple sources, we have restricted the following analysis to the angular range $25° \leq \theta_{lab} \leq 50°$ (depicted as solid lines in panel (b)).

B. Inclusive Correlation Functions

To examine the spatial-temporal size of the emitting source we have utilized two-fragment velocity correlations [6,8–15]. In previous work we have examined the decrease in the spatial-temporal extent of the source as the incident energy is increased [9,10]. This decrease in spatial-temporal extent is understandable if, by increasing the incident energy systems of increased excitation are produced. Other studies indicate that, for a given system, the spatial-temporal extent decreases with increasing incident energy and then saturates at a minimum value [13]. Such a saturation might indicate either a saturation in energy deposition or the minimum spatial extent of the fragmenting source, consistent with an instantaneous breakup scenario. Distinguishing between these two possibilities is key to improving our understanding of multifragmenting nuclear systems.

The velocity correlation function, $R(v_{red})$, is constructed by relating the coincidence yield Y to the background yield $Y^\dagger$:

$$\Sigma Y(\mathbf{v}_1, \mathbf{v}_2) = C^\dagger[1 + R(v_{red})]\Sigma Y^\dagger(\mathbf{v}_1, \mathbf{v}_2), \quad (1)$$

where $\mathbf{v}_1$ and $\mathbf{v}_2$ are the laboratory velocities of the fragments, v_{red} is the reduced velocity given by $v_{red} = (v_1 - v_2)/(Z_1+Z_2)^{1/2}$ cm/ns [6], and $C^\dagger$ is the normalization constant determined by the requirement that $R(v_{red}) \rightarrow 0$ at large reduced relative velocities where the Coulomb repulsion is small. The background yield was constructed by selecting fragments from different events [16].

In order to understand the source of the IMF pairs, we have examined the dependence of the reduced velocity of the fragment pair, v_{red}, on the longitudinal component of the center-of-mass velocity of the fragment pair divided by the beam velocity, $(v_{12})_z/v_{beam}$. The results for $4 \leq Z_1, Z_2 \leq 9$ in the angular range $5.4° \leq \theta_{lab} \leq 80°$ are displayed in Figure 6.4. The fragment mass is assumed to be the mass of the beta-stable isotope for that element. For peripheral interactions (panel (a)), three groups of IMF pairs can be distinguished. The first group, centered at $(v_{12})_z/v_{beam} \approx 0.75$ and $v_{red} \approx 0.035$ c, consists of pairs emitted from the projectile-like source. In the second group, centered at $(v_{12})_z/v_{beam} \approx 0.25$ and $v_{red} \approx 0.035$ c, the pairs originate from the target-like source. The third group, centered at $(v_{12})_z/v_{beam} \approx 0.5$ and $v_{red} \approx 0.065$ c, is composed of events where one IMF is emitted from the projectile-like source and the second is emitted from the target-like source. Fragments emitted in central collisions (panel (b)) originate predominantly from a single group, centered at $(v_{12})_z/v_{beam} \approx 0.3$ and $v_{red} \approx 0.050$ c. The effect of limiting the angular range to $25° \leq \theta_{lab} \leq 50°$ can be seen in panel (c). Selecting on pairs emitted in central collisions appears to preferentially isolate a single source. Similar results have previously been observed for the system ^{36}Ar + ^{197}Au [10].

Velocity correlation functions for central collisions in the reaction ^{84}Kr + ^{197}Au at E/A = 35, 55 and 70 MeV are presented in Figure 6.5. The fragments used in constructing the correlation functions include Z=4 to 9 emitted in the angular range $25° \leq \theta_{lab} \leq 50°$. The normalization constant was determined in the region 0.05c to 0.08c where the correlation function is relatively flat. At low relative velocity, the mutual Coulomb repulsion between the fragments results in strong suppression in the probability of observing fragments of similar velocity. A more significant change in the shape of the correlation function is observed between E/A = 35 and 55 than between E/A = 55 and 70.

To quantitatively extract the spatial-temporal extent of the emitting system, we have performed simulations using a classical 3-body Coulomb trajectory calculation

[10]. This 3-body trajectory model assumes the two fragments are emitted sequentially from the surface of a nucleus of initial atomic number Z_s, mass number A_s, and radius R_s, with the initial separation between source and IMF given by $R_s + R_{IMF}$. The experimentally measured energy, angular, and Z-distributions were used as inputs to the calculation. At E/A = 35 and 70 MeV, the source charge was assumed to be 57 and 32, respectively. This assumption was based upon the total measured charge (corrected for detector acceptance) and assuming the fragments are emitted last in the de-excitation cascade. Thus, this assumption represents an estimated lower limit for the source charge. The source velocities were determined from moving-source fits to be 2.4 and 3 cm/ns at E/A = 35 and 70 MeV, respectively. The time between emissions was assumed to follow an exponential $\exp(-t/\tau)$ characterized by the mean emission time, τ.

The experimental energy spectra from the reaction ^{84}Kr + ^{197}Au at E/A = 55 MeV are compared to the energy spectra calculated by the 3-body Coulomb trajectory model in Figure 6.2. Reasonable agreement is found for the following assumptions: Z_s=40, A_s=96, R_s=7 fm, and τ = 100 fm/c. The source charge was chosen using the prescription as at the other two incident energies. The calculated energy spectra are fairly insensitive to the mean emission time. Calculations using a larger source (e.g. Z_s = 79) fail to reproduce the low-energy portion of the spectrum which suggests that a small source size is more appropriate for the simulations [10]. Because the trajectory model does not treat sub-barrier emission, the correlation functions were constructed for fragments with a velocity above the trajectory model Coulomb barrier ($v \geq 4$ cm/ns).

In Figure 6.6, we display the fragment-fragment velocity correlation functions at E/A = 35 and 70 MeV together with the reference 3-body trajectory calculations. For each value of source radius, the mean emission time is the best fit of the 3-body calculation to the data, as determined by minimizing the χ^2 per degree of freedom, χ^2/ν [10]. If we assume a constant source radius, the mean emission time decreases with increasing bombarding energy. A more complete description of the spatial-temporal size of the emitting system is shown in Figure 6.7. In these calculations, the variables R and τ have been treated as free parameters within physical limits. The lower limit on the radius of 5 fm is approximately equal to the sum of the radii for 2 IMFs. The upper limit of 12 fm corresponds to a source density of $\rho/\rho_0 = 0.1$. The solid and open circles represent best fits to the data at E/A = 35 (Z_s=57, A_s=139) and 70 MeV (Z_s=32, A_s=74), respectively. For the range of assumed source radius, $\tau \leq 140$ fm/c for the data at E/A = 35 MeV and $\tau \leq 115$ for the data at E/A = 70 MeV. These values represent the maximum mean emission times deduced at each bombarding energy.

Also shown in Figure 6.7 for reference is the deduced spatial-temporal extent for the system ^{36}Ar + ^{197}Au [10] at E/A = 50 and 110 MeV. The 50 MeV and 110 MeV data are represented by the solid and dashed lines, respectively. In the Ar-induced reactions, a source charge of $Z_s = 40$ was assumed for the simulations to represent the limiting case where the light charged particles are emitted early in the de-excitation process, followed by the fragments. The spatial-temporal extent for the ^{36}Ar + ^{197}Au data at E/A = 110 is very similar to that of the ^{84}Kr + ^{197}Au data at E/A = 35 MeV, while the Ar data at E/A = 50 MeV has a larger spatial-temporal extent. A qualitative relationship is observed between increasing available energy and emitting source size. The available center-of-mass energies (assuming full linear momentum transfer) are 1522 and 3348 MeV for the ^{36}Ar + ^{197}Au system at E/A = 50 and 110 MeV and 2061 and 4122 MeV for the ^{84}Kr + ^{197}Au system at E/A = 35 and 70 MeV. The Kr data at E/A = 70 MeV has the largest available center-of-mass energy of the systems shown and the smallest spatial-temporal extent. This qualitative relationship between the maximum available energy and the source spatial-temporal extent suggests the underlying relationship between emission time and excitation. This connection between mean emission time and excitation is pursued further in the following section.

C. Exclusive Correlation Functions

A recent investigation [17] has demonstrated the association between the strength of the fragment-fragment interaction and the minimum velocity of the fragment pair, defined as the velocity of the less energetic fragment. The width of the correlation function increases with increasing minimum velocity of the pair, signaling a decrease in the spatial-temporal extent of the emitting source. In this section, we examine the universality of this experimental trend and the effect of different selection criteria in velocity and angular range.

In Figure 6.8(a) we present correlation functions constructed for fragment pairs $4 \leq Z_1, Z_2 \leq 9$ emitted in the angular range $25° \leq \theta_{lab} \leq 50°$ in the reaction ^{84}Kr + ^{197}Au at E/A = 55 MeV. The correlation functions are shown with different cuts in minimum velocity, v_{min}. A significant increase in the width of the Coulomb hole with increasing minimum velocity is observed. In Figure 6.8(b), correlation functions selected on v_{min} are presented for the system ^{36}Ar + ^{197}Au at E/A = 80 MeV [10]. In this case, the correlation functions were constructed for fragments emitted in the angular range $16° \leq \theta_{lab} \leq 40°$. The increase in the width of the Coulomb hole with increasing minimum velocity is also observed for this system. We have also analyzed the ^{14}N + ^{197}Au at E/A = 156 MeV and constructed correlation functions in the angular range $16° \leq \theta_{lab} \leq 80°$. For this reaction, fragments pairs $4 \leq Z_1, Z_2 \leq 7$ were used to construct the correlation function since the cross-section for $Z \geq 8$ is significantly reduced. As can be see in Figure 6.8(c), increasing v_{min} also results in an increasing width of the Coulomb hole for this reaction. Since the characteristics of the fragment velocity spectra depend on the source size, velocity and excitation of the system, different systems exhibit different velocity spectra. Consequently, to compare the different systems, we have chosen minimum velocity cuts based on certain fractions of the velocity distribution at each bombarding energy. For the

Kr and Ar systems, the cuts correspond to the upper 90%, 70%, and 50% of the integrated velocity spectrum in the angular range over which the correlation function is constructed. For the N system, the cuts correspond to the upper 98% and 84% of the integrated velocity spectrum.

Selecting on the average velocity of the two fragments, $v_{avg} = (|v_1| + |v_2|)/2$, instead of v_{min} qualitatively produces the same result, as can be seen in Figure 6.9. The two fragments in a given v_{avg} bin are chosen to have the same velocity within 1 cm/ns. Because selecting on v_{min} doesn't constrain the velocity of the more energetic fragment, cuts in v_{min} correspond on average to more energetic pairs and thus produce a slightly wider Coulomb hole than similar cuts in v_{avg}. One drawback of using v_{avg} is the limitation of a well-defined normalization region. Fragments of a certain v_{avg} have a maximum allowed relative velocity. Since the normalization region arises from particles with large v_{red}, selecting events with a small v_{avg} limits the normalization region.

Recent evidence [18] indicates that fragments of different atomic numbers might sample different time windows of the source de-excitation. Such an effect would distort the association between fragment velocity and emission time that we are currently investigating. To preclude this possibility, we have constructed correlation functions for pairs of boron fragments. The results are presented in Figure 6.10. Correlation functions selected on the minimum velocity of the pair are shown in panel (a). An increase in the width of the Coulomb hole with increasing minimum velocity of the pair is clearly observed for the fragments where $Z_1 = Z_2 = 5$. In panels (b) and (c), we compare these results to simulations using the trajectory model described above. For the assumed source radius, $R_s = 7$ fm, the mean emission time decreases from $\tau = 100 \rightarrow 0$ fm/c as the minimum velocity of the pair is increased from 5 to 7 cm/ns. These results indicate that the increase in the strength of the Coulomb interaction with increasing velocity of the pair is not due solely to different Z_1,Z_2 combinations sampling different portions of the de-excitation cascade.

To examine the increase in the width of the correlation function quantitatively, we have extracted the half-width-at-half maximum (HWHM), the width of the correlation function at half the asymptotic value. The dependence of the extracted HWHM values on the minimum velocity of the fragment pair for the two systems in the laboratory is shown in Figure 6.11(a). The data group themselves along two lines, one corresponding to the two more mass-asymmetric systems (N,Ar) and the other corresponding to the more mass-symmetric system (Kr). For a given minimum velocity in the Kr-induced reactions, the HWHM increases with increasing bombarding energy.

The two different lines observed for the N,Ar and Kr systems in Figure 6.11(a) might arise from the different kinematics of the three excitation functions. To minimize this trivial difference we have moved from the laboratory frame to the center-of-mass frame. An average source velocity was determined by fitting the experimental angular distribution. This source velocity corresponded to: 1.0 cm/ns for all of the N-induced reactions; 2.6, 2.7, and 2.7 cm/ns for the Ar system at E/A = 50, 80, and 110 MeV; 3.4, 3.9, and 4.0 cm/ns for the Kr system at E/A = 35, 55, and 70 MeV. The velocity cuts in the center-of-mass frame were chosen to correspond to the same fractions of the velocity distribution used in the laboratory frame. Removing the contribution of the source velocity reduces the distinct nature of the three projectile-target combinations (Figure 6.11(b)).

Correlation functions gated on v_{min} are depicted in Figure 6.12, both for the laboratory frame (panel (a)) and for the center-of-mass (panel (b)). The increase in HWHM in the angular range from 25° to 50° in the laboratory is similar to that observed in the range from 45° to 90° in the center-of-mass. This observation can be interpreted as the two ranges sampling comparable regions in phase space. The correlation functions selected on minimum velocity for different angular ranges in the center-of-mass are presented in Figure 6.13. The increase in HWHM with increasing minimum velocity of the pair is greater at more backward angles in the center-of-mass. This result can perhaps be understood in the following context: the fragment cross-section measured at forward angles contains a larger non-equilibrium contribution than the fragment cross-section at backward angles. This non-equilibrium component arises from fragment emission from sources associated with different amounts of linear momentum transfer and correspondingly different source velocities. Consequently, selection of fragment pairs of higher average velocity can select pairs from higher velocity sources, not necessarily sources of higher excitation.

In order to further isolate the contribution from different sources, we have performed an analysis in which we have restricted the longitudinal velocity of the IMF pair. Shown in Figure 6.14 is the distribution of the longitudinal velocity, $(\mathrm{v}_{12})_z/\mathrm{v}_{beam}$ $= (|v_1|_z + |v_2|_z)/v_{beam}$, for fragment pairs $4 \leq Z_1, Z_2 \leq 9$ emitted in the angular range $25^\circ \leq \theta_{lab} \leq 50^\circ$ for central collisions of the reaction ^{84}Kr + ^{197}Au at E/A = 70 MeV. The distribution is essentially a skewed Gaussian peaked at $(\mathrm{v}_{12})_z/\mathrm{v}_{beam} = 0.33$ with an exponential tail extending to $(\mathrm{v}_{12})_z/\mathrm{v}_{beam} \approx 0.73$. Large values of $(\mathrm{v}_{12})_z/\mathrm{v}_{beam}$ correspond to fragment pairs of large longitudinal velocities, presumably from sources of high velocity. The arrows shown in the figure indicate values of $(\mathrm{v}_{12})_z/\mathrm{v}_{beam} = 0.3$, 0.4, and 0.5.

We have constructed correlation functions in the same manner previously described with the additional restriction on $(\mathrm{v}_{12})_z/\mathrm{v}_{beam}$. Correlation functions shown in Figure 6.15, panels (a), (b), and (c) correspond to restrictions of $(\mathrm{v}_{12})_z/\mathrm{v}_{beam} \leq$ 0.5, 0.4 and 0.3, respectively. As can be seen in the figure, in all cases increasing the v_{min} criterion results in an increasing width of the Coulomb hole indicating a stronger fragment-fragment interaction. Decreasing the threshold of $(\mathrm{v}_{12})_z/\mathrm{v}_{beam}$ from 0.5 to 0.3 limits the maximum v_{min} for which the correlation function can be constructed. The reduced change in the correlation functions shown in Figure 6.15(c) as compared to Figure 6.15(a) is due this reduction in the v_{min} range.

The dependence of the extracted HWHM on v_{min} is shown in Figure 6.16. The same dependence of HWHM on v_{min} is observed both for the $(\mathrm{v}_{12})_z/\mathrm{v}_{beam}$ integrated results, as well as, the results from cases involving various restrictions in $(\mathrm{v}_{12})_z/\mathrm{v}_{beam}$.

It is evident in Figure 6.16 that the three cases involving restrictions in $(\mathrm{v}_{12})_z/\mathrm{v}_{beam}$ have (within the uncertainties shown) the same semi-quantitative dependence of HWHM on v_{min} as the $(\mathrm{v}_{12})_z/\mathrm{v}_{beam}$ integrated results. This insensitivity of the dependence of HWHM on v_{min} to cuts in $(\mathrm{v}_{12})_z/\mathrm{v}_{beam}$ suggests that the dependence of HWHM on v_{min} is not significantly attributable to fragments originating from sources with different longitudinal source velocities.

Recent analyses [15] have utilized directional cuts in the correlation function to attempt to resolve ambiguities between source size and lifetime. We have examined the effect of our velocity selection on such directionally constrained correlation functions. Transverse correlation functions with different cuts in minimum velocity for the system ^{84}Kr + ^{197}Au at E/A = 70 MeV are shown in Figure 6.17. The transverse cut is defined as $\psi = 80° - 90°$, where ψ is the angle between the reduced velocity, v_{red}, and the total velocity vector, $\mathbf{V} = \mathbf{v}_1 + \mathbf{v}_2$ [15]. The increase in the value of HWHM with increasing minimum velocity of the fragment pair is semi-quantitatively the same as previously displayed in Figure 6.11. The longitudinal correlation functions ($\psi \leq 40°$, not shown) might exhibit a smaller increase in width with increasing v_{min}. However, due to the lack of a well defined normalization region, the extraction of the width of the correlation function is more difficult than for the transverse cut. Consequently, for the longitudinal cut, the quantitative dependence of the value of HWHM on v_{min} is difficult to assess.

D. Finite Detector Resolution Effects

We now focus on the sensitivity of the observed trends to the detector granularity, energy resolution, and particle identification limitations of the detector setup. Determination of the magnitude of these effects allows us to assess the relative errors associated with the trends we have observed in the data.

The effect of finite angular resolution is illustrated in Figure 6.18. The open points depict the theoretical correlation function for ^{11}B fragments with a source of radius 7 fm and a mean emission time of 100 fm/c unfiltered by the detector granularity. The solid line is the result of filtering these results with the detector granularity. Because it is difficult to describe low-energy emissions in the context of the classical trajectory calculation, the fragments have a minimum velocity cutoff of 4.5 cm/ns. As can be seen in the figure, the detector granularity produces only a minor distortion of the correlation function. The filtered correlation function is rotated about a point close to the HWHM, producing a wider Coulomb hole. This suggests that the 'true' correlation function has a slightly narrower Coloumb hole than is measured by our apparatus;however, the quantity HWHM seems to be relatively insensitive to the rotation.

In Figure 6.19(a) we examine the effect of the finite energy resolution of the experimental apparatus on the correlation function. The points are the correlation function constructed from the data measured with an estimated energy resolution of about 15% [1]. The solid and dashed lines are the result of smearing on a Gaussian distribution with a FWHM of 10% and 20%, respectively. The 10% smearing does not produce a noticeable change in the correlation function, while the 20% case results in a small rotation, similar to that observed in the case of the detector granularity. Investigations of the energy spectra before and after the smearing have shown that the 20% FWHM smearing causes only a 1% change in the width, or second moment, of the Be energy spectrum measured in the range $25° \leq \theta_{lab} \leq 31°$.

Isotope misidentification of fragments is another source of uncertainty in this analysis. The theoretical correlation functions shown in Figure 6.19(b) were constructed using the same conditions as in Figure 6.18. We first assumed that all of the boron was A=10 (solid points). Following this calculation we assumed all of the boron was A=12 (open circles). Increasing the mass of the boron fragment decreases the width of the Coulomb hole. For a given fragment energy, increasing the assigned mass decreases